Ultrafast pump-probe fluence and wavelength dependent relaxation dynamics in graphene

By

Rustam Gatamov

Dissertation

Submitted to the Faculty of the

Graduate School of Vanderbilt University

in partial fulfillment of the requirements

for the degree of

DOCTOR OF PHILOSOPHY

in

Physics

December 12, 2020

Nashville, Tennessee

Approved:

Norman H. Tolk, Ph.D.

Jimmy L. Davidson, Ph.D.

Sokrates T. Pantelides, Ph.D.

Sait A. Umar, Ph.D.

Kalman Varga, Ph.D.

ACKNOWLEDGMENTS

I would like to thank my advisor Norman Tolk for his support, mentoring and enabling the group's research. I would also like to express my deepest gratitude to Andrey Baydin and Halina Krzyzanowska, who made significant contributions to my research progress. I thank my PhD committee members Kalman Varga, Sait Umar, Sokrates Pantelides, Jimmy Davidson for their input. I would also like to thank VINSE staff Anthony Hmelo and Dmitry Koktysh for their technical support. Special thanks to the administrative team of the Department of Physics and Astronomy Don Pickert, Sheila Warf, Libby Johnson, Peggy McGowan and Barbara Amann, who were always there to help with any issues.

TABLE OF CONTENTS

LIST OF FIGURES

Chapter 1

Introduction

1.1 Motivation

Graphene is a single layer material of carbon atoms with linear dispersion relation at the K points of the Brilluion zone (Figure 1.8), which leads to high carrier mobility and unique opto-electronic properties making it useful for a wide range of applications [22, 23, 24, 25, 26, 27]. The use of the advantageous properties of graphene in application to opto-electronic devices inevitably entails the generation of hot carriers with energies significantly exceeding the Fermi energy [25, 22, 23]. Therefore, carrier relaxation dynamics plays a central role in many proposed graphene based devices [28, 29, 30, 31]. Especially with the scale of devices continuing to shrink, power capabilities being pushed to the limit and efficient heat removal becoming an issue it is hard to overestimate the importance of a more comprehensive understanding of carrier relaxation dynamics in graphene.

There is an enormous ongoing effort by many groups to study graphene related relaxation dynamics using various techniques such as photocurrent measurements, ultrafast pump-probe spectroscopy, time resolved Raman spectroscopy, etc. [32, 33, 34]. Ultrafast pump-probe spectroscopy is a powerful technique that allows to monitor the relaxation dynamics of photoexcited electrons with femtosecond temporal resolution, which supercedes the capabilities of modern electronics. Ultrafast pump-probe spectroscopy has been particularly fruitful in providing valuable insights into electron-electron, electron-phonon and phonon-phonon interactions [34, 35, 36, 37, 38, 39, 40, 41]. Typically, after electrons and holes are excited into a non-thermal distribution by an ultrafast laser pulse, they thermalize into a Fermi-Dirac distribution through Coulomb interactions in tens of femtoseconds [42, 43, 1, 44, 45]. The thermal distribution of photoexcited electrons further cools to lower temperatures on a picosecond time scale. Brida *et al.* [1] experimentally investigated

the subpicosecond nonequilibrium electron dynamics in graphene and identified ultrafast collinear scattering, which enables Auger processes including carrier multiplication, as the significant fundamental physical mechanism governing the ultrafast dynamics of graphene. Figure 1.1 depicts thermalization of a narrow hot distribution of photoexcited electrons and further cooling of the thermalized distribution in a subpicosecond time window. As illustrated in Figure 1.1, the initial narrow hot electron distribution (red) turns into a broad nonthermal distribution (black) by 10 femtoseconds, which subsequently thermalizes into a high temperature Fermi-Dirac distribution (green) by 50 femtoseconds followed by further cooling of the Fermi-Dirac distribution. The cooling of the hot thermal population of carriers occurs through the emission of optical phonons. The processes of thermalization and further cooling are illustrated in Figure 1.2 [2]. At the point when the temperatures of the electron and phonon systems equilibrate, the hot phonon bottleneck occurs, which significantly lessens the cooling rate [39, 46, 47]. Subsequent cooling primarily results from the hot optical phonons undergoing anharmonic decay into acoustic phonons. However, in the case of supported graphene, direct coupling of the charge carriers to surface phonons in the polar substrates is a possible cooling channel [48, 49, 50, 51]. As predicted by theory and measured by experiments, the time constant of the hot optical phonon decay in graphene is of the order of a few picoseconds [46, 39, 52, 33, 41, 40, 38]. The hot phonon bottleneck bears far reaching implications for device performance, in particular the timescale of the photoresponse in opto-electronic devices [25, 53, 54, 55]. Hence, full understanding of the cooling pathways for excited carriers and hot phonons are necessary for device applications.

A positive transient differential transmission response of graphene in an ultrafast pump-probe experiment was observed by different groups [2, 39, 56, 57]. The positive transient differential transmission is attributed to bleaching of the interband transitions due to Pauli blocking as the time dependent hot electron distribution in the conduction band decreases absorption. As the distribution of the excited electrons cools down, absorption increases

and differential transmission decreases. Monitoring temporal evolution of the transient differential transmission allows to measure the time dependent electron density and electron distribution.

Malard *et al.* [41] observed both positive and negative fluence dependent transient differential transmission in graphene. The negative transient differential transmission occurs due to induced free carrier absorption in view of dominating intraband electron transitions at lower temperatures achieved at lower pump fluences. Microscopic description of intraband absorption in graphene was given by Kadi *et al.* [3]. The fluence dependent studies showing transient negative differential transmission imply that optical response of graphene can be accurately described only when contributions from both intra- and interband electron transitions to the optical conductivity are taken into account. Indeed, as demonstrated by Kadi *et al.* in Figure 1.3 [3], switching on and off the intraband transitions has a dramatic effect in the range of pump fluences, at which intra- and interband transitions have comparable contributions to the optical conductivity of graphene.

To summarize, previous measurements of photo-induced ultrafast dynamics in graphene by pump-probe spectroscopy have yielded a diversity of differential transmission and reflection dynamics [58, 59]. It has been shown that differential transmission dynamics (DTD) depends on carrier scattering time, doping, Fermi level and probe energy [58, 59, 60, 35, 61]. Several different regimes for DTD have been observed: i) fully positive DTD [35, 60, 61, 62, 63, 64, 65, 39, 57], ii) fully negative DTD [36, 66, 67, 68], and iii) a complex DTD consisting of a positive peak near zero time delay followed by a negative slow recovery tail [59, 61, 60, 34, 35, 58, 69]. The transient differential transmission through graphene is positive in high fluence ultrafast pump-probe experiments due to the bleaching of dominating interband electron transitions at high temperatures owing to Pauli blocking. The transient differential transmission drops below zero and becomes negative after the initial positive spike in low fluence ultrafast pump-probe experiments due to the negative contribution to the optical transmission of the phonon assisted intraband electron transitions

that are dominant at low temperatures. A natural question that follows is concerned with the ultrafast pump-probe response of graphene at those pump fluences, when the crossover from the negative to positive transient differential transmission occurs, which, to the best of our knowledge, has not been investigated. Consequently, we set out to investigate the transition from the intra- to interband dominated ultrafast pump-probe response of graphene, which occurs at the pump fluences ensuring comparable contributions from both processes.

Thus, we conducted a comprehensive study on fluence and wavelength dependent ultrafast pump-probe relaxation dynamics of single layer graphene supported on a soda-lime glass substrate. We were able to observe both intra- and interband dominated response. Our unique contribution lies in studying the transition from the intra- to interband dominated relaxation dynamics. Interestingly, we found an order of magnitude faster relaxation of the ultrafast pump-probe signal.

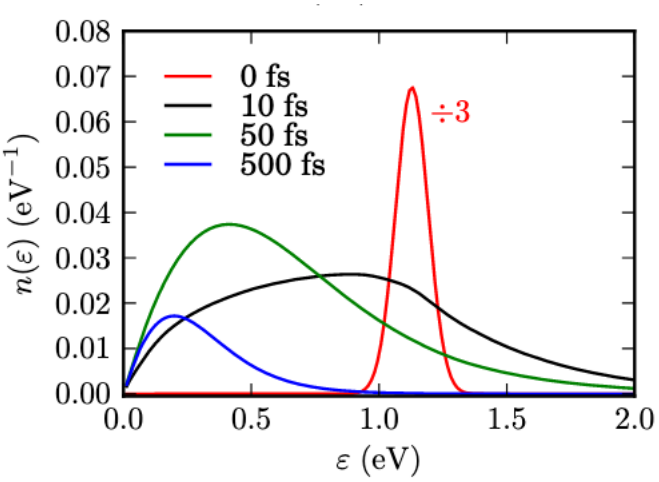

Figure 1.1: Temporal evolution of the electron population per unit cell[1].

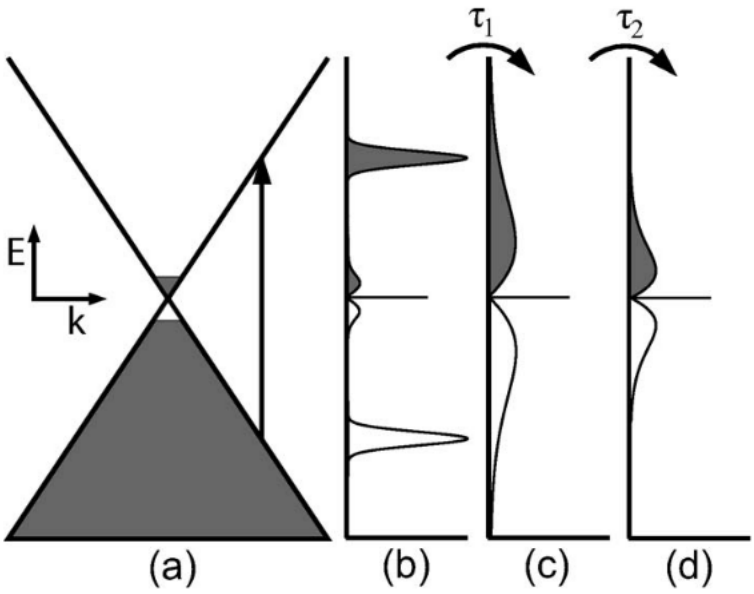

Figure 1.2: a) Band structure of graphene with intrinsic electron and hole population near the Dirac point. b) The nonequilibrium distribution of carriers after photoexcitation. c) The carrier thermalization process. d) The further cooling of the thermal carrier distribution [2].

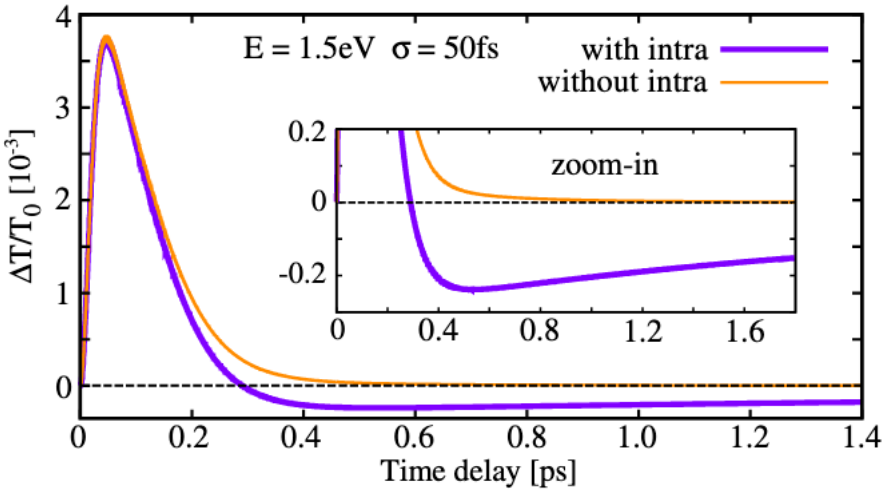

Figure 1.3: The effect of the phonon assisted intraband transitions on the transient differential transmission in graphene [3].

1.2 Statement of work

In this work, we study fluence dependent ultrafast carrier and phonon dynamics in CVD graphene on a soda-lime glass substrate using pump-probe spectroscopy in transmission geometry at the wavelengths of 775 nm, 800 nm, 825 nm and 850 nm. We cover a range of pump fluences that allows us to observe probe dynamics governed by both intra- and interband transitions. In our measurements, we examine the transition from complex DTD to fully positive DTD as a function of pump fluence. At low pumpfluences, after the initial positive spike arising from the bleaching of the in-terband transitions, the differential transmission crosses zero and its slow recovery tail is negative due to primarily intraband absorption processes. An example of such a response and a possible microscopic mechanism are illustrated in figures 1.4 and 1.5, respectively. A paper by F. Kadi *et al.* [70]

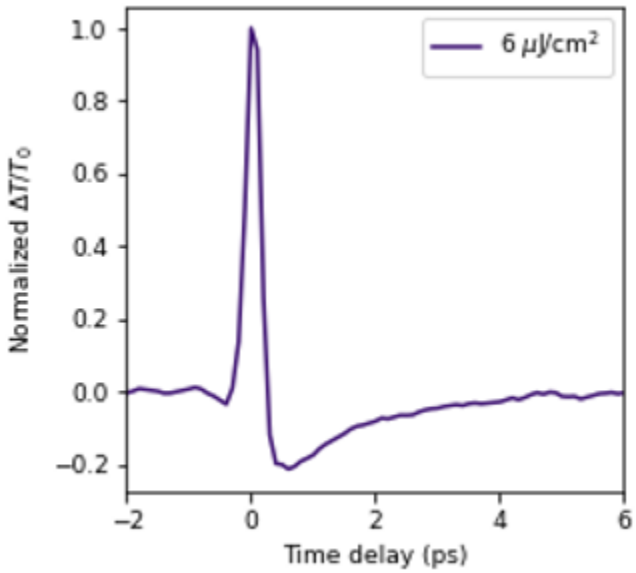

Figure 1.4: Differential transmission of graphene at low fluence showing the predominant role of intraband transitions.

explains the observation of transient negative differential transmission, i. e. a zero-crossing of the differential transmission at about 300 fs, using a microscopic treatment of intraband absorption in graphene. At high pump fluences, the slow recovery tail of the differential

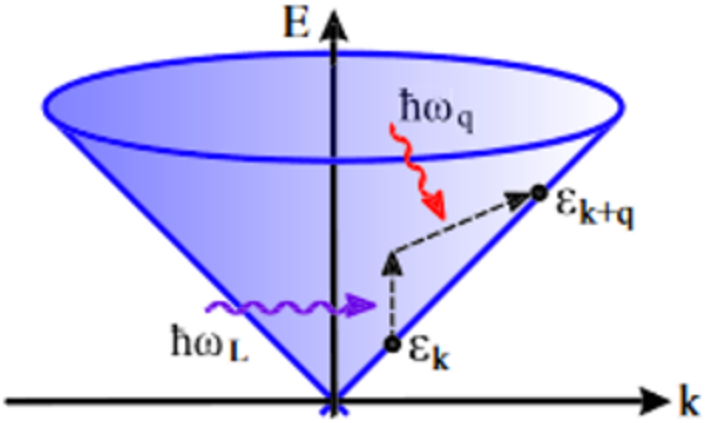

Figure 1.5: The phonon assisted intraband absorption within the linear band structure of graphene [3].

transmission is positive due to predominant interband transitions, which is illustrated in figure 1.6. The response at low and high fluences has already been observed and discussed

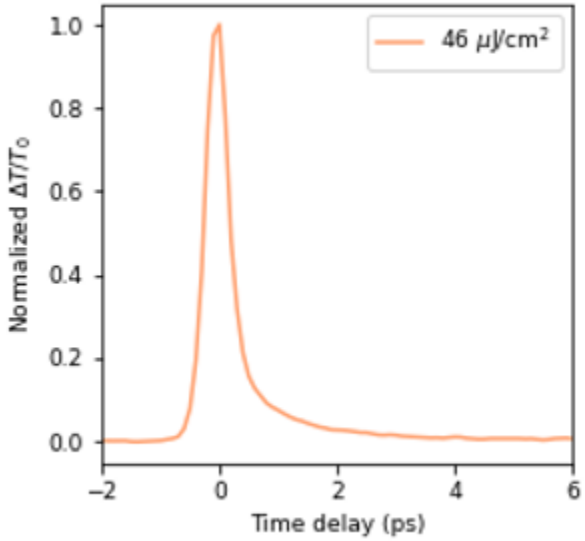

Figure 1.6: Differential transmission of graphene at high fluence showing the predominant role of interband transitions.

in previous works [41, 3, 71]. Thus, in this work we study the transition from intraband to interband dominated response of graphene. Thus, this work provides a novel experimental

observation of an order of magnitude faster relaxation of differential transmission at the intermediate pump fluences, where the intraband and interband contributions are equal in magnitude and opposite in sign. A natural question arises as to the physical reasons for a faster relaxation of the optical signal. We apply a model that relates transmission to the optical conductivity of graphene depending on the temperature of the Fermi-Dirac distribution of electrons. The temporal evolution of electron temperature is simulated by the rate equations describing the cooling of the electron system and the coupled optical phonons via emission of lower energy phonons. The phenomenological relaxation time constant of the optical phonons does not show any abrupt changes in the vicinity of the transition pump fluence, whence it follows that the faster decay of the differential transmission is not due to the change in the relaxation mechanism. The effect is attributed to the opposite and approximately equal contributions of intra- and interband transitions to the optical conductivity of graphene in the vicinity of the transition pump fluence. As the relaxation time of the electron temperature is found to increase monotonically over the range of pump fluences used in this study, comparison with the measured relaxation times of the differential transmission implies that pump fluence greatly modifies time-dependent optical properties, while the electron and phonon relaxation processes remain unaffected.

1.3 Thesis outline

The content of this dissertation runs as follows:

Chapter 1 started with a review of the existing literature on ultrafast carrier relaxation dynamics in graphene studied by pump-probe spectroscopy, naturally followed by motivation for the study the current dissertation is seeking to present as well as short description of the achieved results. The last section in this introductory chapter reviews basic properties of graphene such as band structure and optical transmission.

Chapter 2 describes experimental techniques employed for this study. In particular, the first section starts off with chemical vapor deposition (CVD) graphene growth and

transfer onto desired substrates. The second section discusses the fundamentals of Raman spectroscopy and the phonon properties in graphene followed by the Raman peaks of single layer graphene explained in terms of the underlying Raman processes. Applications of Raman spectroscopy to characterization of graphene such as determination of layer number, stacking order, defects and doping are also elaborated on. The last section in this chapter presents the fundamentals of the pump-probe spectroscopy crucial to this study.

Chapter 3 describes experimental work and data as obtained during the current study. The first section describes the preparation and characterization of our sample . The second section presents experimental pump-probe transmission data. The third section describes the bi-exponential analysis of transmission relaxation curves, which yields our new observation of an order of magnitude faster relaxation time of differential transmission in the vicinity of the transition pump fluence, when the crossover from negative to positive response occurs.

Chapter 4 describes an attempt to explain the new observation by applying a model that relates transmission to the optical conductivity of graphene with contributions from both intra- and interband transitions depending on the temperature of the Fermi-Dirac distribution of electrons. We attributed our new observation to the opposite and approximately equal contributions of intra- and interband transitions to the optical conductivity in the vicinity of the transition pump fluence based on the modelling results.

Chapter 5 provides an overview and conclusions for the conducted study as well as outlines a potential area, where the new observation may find its application.

1.4 Review of graphene properties

Graphene is a hexagonal lattice of carbon atoms with sp^2 hybridization and the interatomic distance of 1.42 Å [72]. Each carbon atom contributes four valence electrons, of which three participate in the formation of sp^2 hybridized orbitals, thus producing strong planar covalent σ bonds with each of its three neighbors responsible for the high stiffness

of the graphene lattice with Young's modulus measured up to 1 TPa [73, 74] and high thermal conductivity for suspended graphene of approximately 5300 $Wm^{-1}K^{-1}$ [75]. The remaining p_z electron forms the π bond oriented out of the plane of graphene. The π bonds further hybridize to form the π and π^* bands corresponding to the dispersion of bonding and antibonding molecular orbital. The π and π^* bands provide the only free electrons responsible for the conductivity and transport properties in graphene.

The unit cell of single layer graphene consists of two nonequivalent carbon atoms and is spanned by the two basis vectors $\mathbf{a}_1 = a_0(\frac{\sqrt{3}}{2}, \frac{1}{2})$ and $\mathbf{a}_2 = a_0(\frac{\sqrt{3}}{2}, -\frac{1}{2})$, where $a_0 = \sqrt{3}b$ with the interatomic distance of $b = 1.42$ Å (see Figure 1.7). The coordinates of the high symmetry points in the first Brillouin zone of the reciprocal space are $\Gamma = (0,0)$, $K = (\frac{2\pi}{\sqrt{3}a_0}, \frac{2\pi}{3a_0})$ and $M = (\frac{2\pi}{\sqrt{3}a_0}, 0)$.

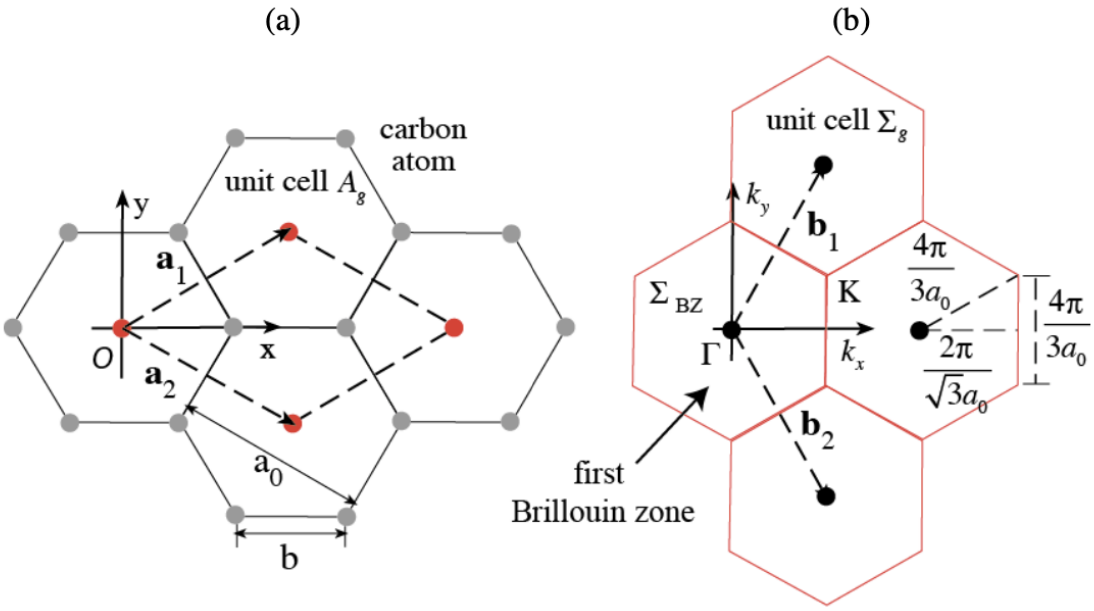

Figure 1.7: a) Bravais lattice. b) Reciprocal lattice [4].

Within the nearest neighbor tight binding approximation, the energy dispersion for the π electrons is expressed by the following relation [76]:

$$E(\mathbf{k}) = \pm\gamma\sqrt{1+4\cos(\frac{\sqrt{3}k_x a_0}{2})\cos(\frac{k_y a_0}{2})+4\cos^2(\frac{k_y a_0}{2})}, \tag{1.1}$$

where $\gamma = 2.7\ eV$ is the nearest neighbor hopping energy. As seen from Figure 1.8, the energy dispersion surfaces for the π and π^* bands touch each other at the K points of each Brillouin zone. Electrons have linear dispersion around the point where the conduction and valence bands meet. The energy dispersion has a saddle point singularity at the M point. The energy gap between the valence and the conduction bands at the Γ point is approximately 20 eV [22, 77]. The constant energy contour plot is isotropic and the energy dispersion is parabolic around the Γ point.

In the linear approximation near the Dirac point, the energy dispersion relation can be written as

$$E(\mathbf{k}) \approx \pm \hbar \upsilon_F q, \tag{1.2}$$

where $\upsilon_F \sim 10^6\ m/s$ and $\mathbf{q}$ is the wave-vector relative to the Dirac point. Electrons in graphene are described as massless Dirac fermions by the Dirac equations [22].

The density of states in graphene can be calculated as follows:

$$D(E) = \frac{2}{A} \sum_{\mathbf{k}} \delta(E(\mathbf{k}) - E) \tag{1.3}$$

$$D(E) = \frac{1}{2\pi^2} \iint_{1stBZ} \delta(E(\mathbf{q}) - E) d^2q \tag{1.4}$$

By using Dirac approximation near the K and K' points and intergrating over the first Brillouin zone:

$$D(E) = \frac{1}{\pi^2} \iint \delta(\hbar \upsilon_F q - E) d^2q = \frac{2}{\pi} \int_0^\infty \delta(\hbar \upsilon_F q - E) q dq = \frac{2}{\pi \hbar^2 \upsilon_F^2} \int_0^\infty \delta(x - E) x dx \tag{1.5}$$

Hence, the density of states becomes equal to:

$$D(E) = \frac{2E}{\pi \hbar^2 \upsilon_F^2} \tag{1.6}$$

The linear density of states around the zone edges along with the zero band gap of graphene

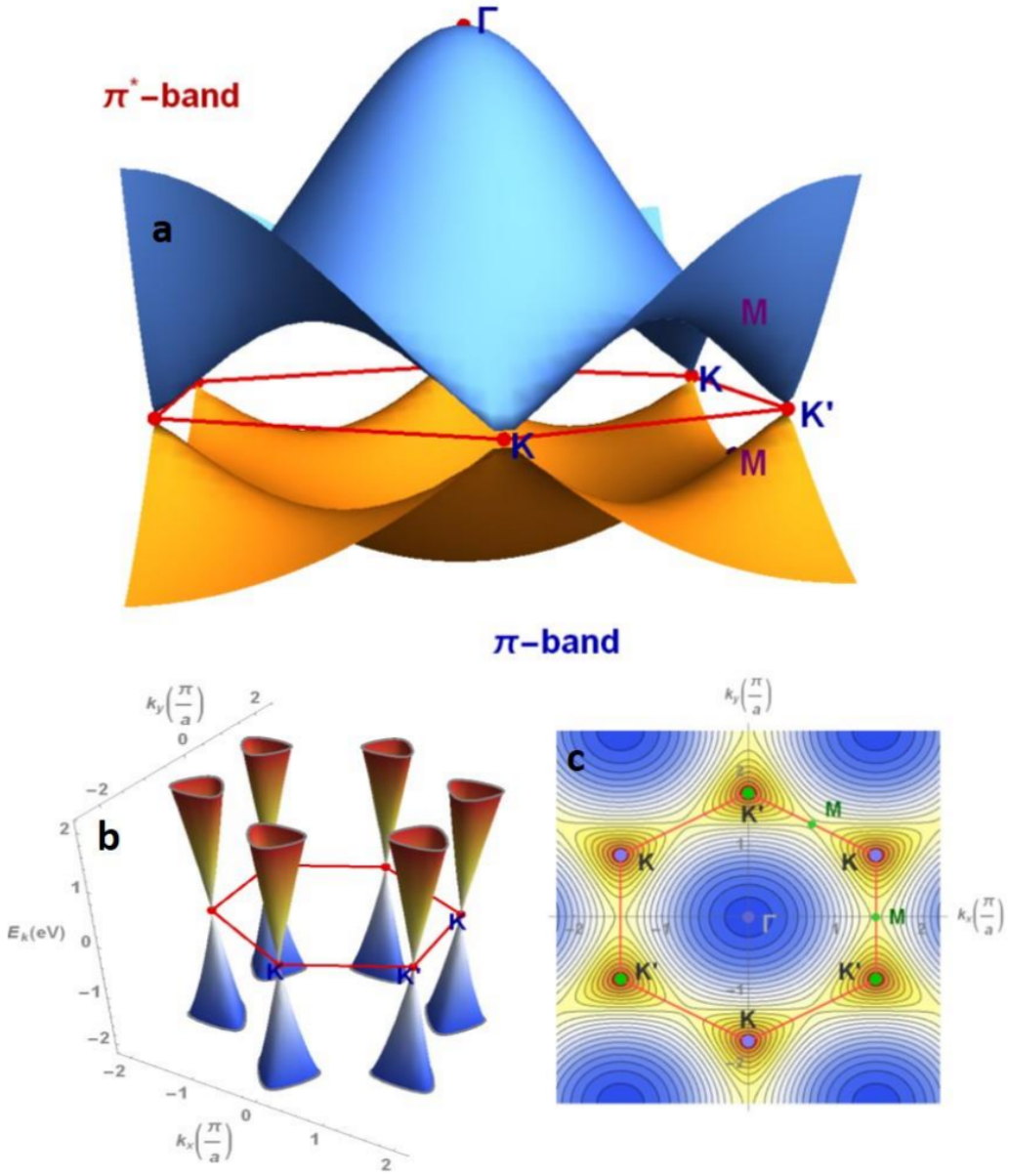

Figure 1.8: a) Energy dispersion for the electrons in the π and π^* bands of single layer graphene in the first Brillouin zone. b) Dirac cones near the K points. c) Constant energy contour map in the first Brillouin zone for the electrons in the π valence band. [5]

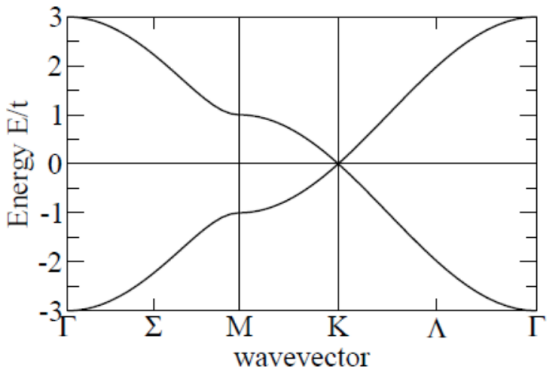

Figure 1.9: Band structure of graphene plotted along the lines connecting high symmetry points.

result in a high temperature dependent electron mobility up to $\sim 170,000 cm^2/Vs$ [78]. Moreover, graphene exhibits the ballistic charge transport with the long mean free path of 600 *nm* [79].

The uniform $\sim 2\%$ broad band absorption [80] along with high electron mobility renders graphene potentially useful in optoelectronic applications, for instance near infrared and THz detectors and saturable absorbers [81, 82]. The optical absorption in graphene occurs by means of two fundamentally different processes, namely inter- and intraband electron transitions schematically illustrated in Figure 1.10. Intraband transitions are dominant in the far infrared region and occur via free carrier absorption in the conduction band. Interband transitions are prevailing in the mid to near infrared range and occur by direct electron transitions between the valence and conduction bands [24]. The contribution of the interband transitions to the optical conductivity for high frequencies is equal to [83, 84]:

$$\sigma_{inter}(\omega) = -\frac{e^2\omega}{i\pi\hbar}\int_0^{+\infty}\frac{f_0(-\varepsilon)-f_0(\varepsilon)}{(\omega+i\delta)^2-4\varepsilon^2}d\varepsilon \tag{1.7}$$

The real part can be further derived [83, 84, 85]:

$$\mathrm{Re}\sigma_{inter}(\omega) = \frac{e^2}{8\hbar}\left[\tanh\left(\frac{\hbar\omega-2E_F^e}{4k_BT}\right)+\tanh\left(\frac{\hbar\omega-2E_F^h}{4k_BT}\right)\right] \tag{1.8}$$

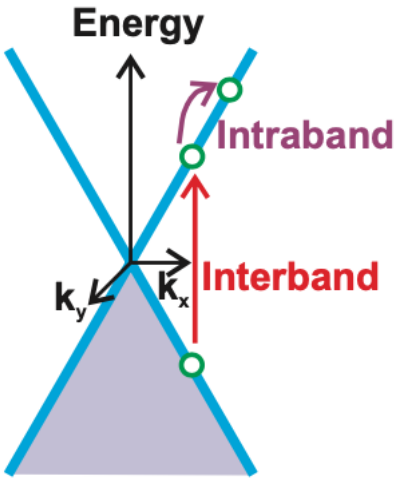

Figure 1.10: Schematic band structure of undoped graphene showing interband and intraband electron transitions [6].

At zero temperature and zero doping, the optical conductivity is frequency independent within used approximations and is referred to as universal conductivity of graphene and related to the fine structure constant $\alpha = \frac{e^2}{4\pi\varepsilon_0\hbar c}$ (Figure 1.11a). This is responsible for $\sim 2\%$ universal absorption in graphene:

$$\mathrm{Re}\sigma_{inter}(\omega) = \frac{e^2}{4\hbar} \tag{1.9}$$

The contribution of the intraband transitions to the optical conductivity can be expressed as [83, 84]:

$$\sigma_{intra}(\omega) = \frac{e^2\omega}{i\pi\hbar}\int_{-\infty}^{+\infty}\frac{|\varepsilon|}{\omega^2}\frac{df_0(\varepsilon)}{d\varepsilon}d\varepsilon, \tag{1.10}$$

where $f_0(\varepsilon) = \frac{1}{\exp[(\varepsilon-\varepsilon_F)/k_BT]+1}$ is the Fermi-Dirac function. To account for the scattering processes we must change ω by $\omega + i\tau^{-1}$. Further integration yields:

$$\sigma_{intra}(\omega) = \frac{ie^2k_BT}{\pi\hbar^2(\omega+i\tau^{-1})}\left[\ln\left(1+e^{E_F^e/k_BT}\right)+\ln\left(1+e^{E_F^h/k_BT}\right)\right] \tag{1.11}$$

The equation above takes the Drude-Boltzmann form for the case of $E_F \gg k_BT$:

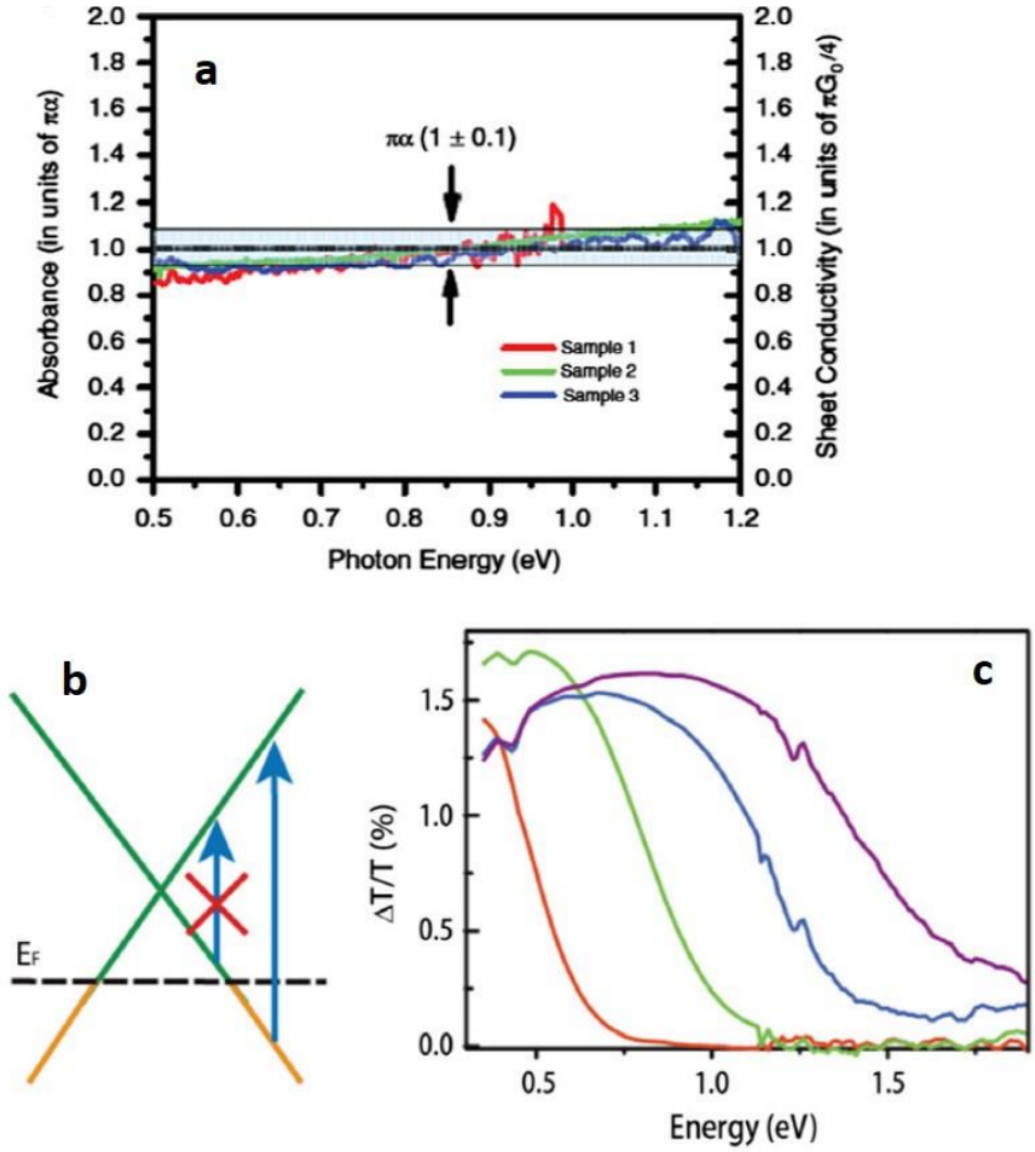

Figure 1.11: a) Universal absorbance and optical sheet conductivity of graphene. b) Blocked interband transitions with energies below $2|E_F|$ for hole doped graphene. c) Dependence of transmission on hole doping induced by gate voltage[7].

$$\sigma_{intra}(\omega) = \frac{ie^2|E_F|}{\pi\hbar^2(\omega + i\tau^{-1})} \tag{1.12}$$

The real part of the intraband optical conductivity can be further written out as:

$$\sigma_{intra}(\omega) = \frac{e^2 k_B T}{\pi\hbar^2} \frac{\frac{1}{\tau}}{\omega^2 + \frac{1}{\tau^2}} \left[\ln\left(1 + e^{E_F^e/k_B T}\right) + \ln\left(1 + e^{E_F^h/k_B T}\right) \right] \tag{1.13}$$

An accurate description of the optical properties in graphene is possible only when both contributions are taken into account:

$$\mathrm{Re}\sigma_{total}(\omega) = \mathrm{Re}\sigma_{inter} + \mathrm{Re}\sigma_{intra} \tag{1.14}$$

$$\begin{aligned} \mathrm{Re}\sigma_{total}(\omega) = \frac{e^2 k_B T}{\pi\hbar^2} \frac{\frac{1}{\tau}}{\omega^2 + \frac{1}{\tau^2}} \left[\ln\left(1 + e^{E_F^e/k_B T}\right) + \ln\left(1 + e^{E_F^h/k_B T}\right) \right] + \\ + \frac{e^2}{8\hbar} \left[\tanh\left(\frac{\hbar\omega - 2E_F^e}{4k_B T}\right) + \tanh\left(\frac{\hbar\omega - 2E_F^h}{4k_B T}\right) \right] \end{aligned} \tag{1.15}$$

Optical transmission at perpendicular incidence through a single layer graphene of thickness d can be determined by using the magnitude of the electric field:

$$E = A\exp(i\mathbf{k}\cdot\mathbf{r}) = A\exp(ik_0\tilde{n}z) = A\exp(-k_0 kz)\exp(ik_0 nz), \tag{1.16}$$

where $k_0 = \frac{\omega}{c}$ and $\tilde{n} = n + ik$ is the complex index of refraction. The transmittance of single layer graphene t is defined as the ratio of the intensities of the transmitted and incident light:

$$t = \frac{I}{I_0} \tag{1.17}$$

Intensity of light is proportional to the square of the magnitude of the electric field:

$$I \sim E^2 = A^2\exp(-2k_0 kz) \tag{1.18}$$

Hence, transmittance can written as:

$$t = \frac{I}{I_0} = \exp(-2k_0 kd) \approx 1 - 2k_0 kd \tag{1.19}$$

To express k in terms of the optical conductivity we use the following relations between the polarization density, susceptibility and the the polarization current density:

$$\mathbf{P}(\omega) = \varepsilon_0 \chi \mathbf{E}(\omega) \tag{1.20}$$

$$\mathbf{J}(\omega) = \sigma_{3D}(\omega)\mathbf{E}(\omega) \tag{1.21}$$

$$\mathbf{J}_P(\tau) = \frac{\partial \mathbf{P}(\tau)}{\partial \tau} \tag{1.22}$$

Since the time dependence of the electric field is $\exp(-i\omega\tau)$, we get

$$\mathbf{J}(\omega) = -i\omega\varepsilon_0 \chi(\omega)\mathbf{E}(\omega) \tag{1.23}$$

Hence, the relation between the susceptibility and the optical conductivity is:

$$\chi(\omega) = \frac{i\sigma_{3D}(\omega)}{\varepsilon_0 \omega} \tag{1.24}$$

The two dimensional optical conductivity is:

$$\sigma_{2D}(\omega) = d\sigma_{3D}(\omega) \tag{1.25}$$

Hence, for the susceptibility we get:

$$\chi(\omega) = \frac{i\sigma_{2D}(\omega)}{\varepsilon_0 \omega d} \tag{1.26}$$

The expression for the complex refractive index $\tilde{n}$ in terms of the relative permittivity $\varepsilon_r =$

$1+\chi$ and the relative permeability $\mu_r \approx 1$ for graphene is given by:

$$\tilde{n} = \sqrt{\varepsilon_r \mu_r} = \sqrt{1+\chi} \approx 1 + \frac{1}{2}\chi \tag{1.27}$$

$$\tilde{n} = 1 + \frac{i\sigma_{2D}(\omega)}{2\varepsilon_0 \omega d} \tag{1.28}$$

Hence, k is found by taking the real part of the two dimensional optical conductivity:

$$k(\omega) = \frac{\mathrm{Re}\sigma_{2D}(\omega)}{2\varepsilon_0 \omega d} \tag{1.29}$$

Hence, the expression for transmittance t becomes:

$$t(\omega) = 1 - \frac{k_0 \mathrm{Re}\sigma_{2D}(\omega)}{\varepsilon_0 \omega} = 1 - \frac{\mathrm{Re}\sigma_{2D}(\omega)}{\varepsilon_0 c} \tag{1.30}$$

In the regime of the universal absorption with the constant optical conductivity $\sigma_0 = \frac{e^2}{4\hbar}$ transmittance is equal to:

$$t(\omega) = 1 - \frac{\sigma_0}{\varepsilon_0 c} = 1 - \pi\alpha \approx 0.98 \tag{1.31}$$

Since the conduction band is empty at zero doping, any incident photon energy can be absorbed by creation of an electron-hole pair, which ensures broadband absorption in a wide spectral range. However, as illustrated in Figure 1.11b, the presence of doping, i. e. a shift in the Fermi level, blocks interband transitions with energies below $2|E_F|$ due to Pauli exclusion principle. Pauli blocking of the interband transitions with energies below $2|E_F|$ provides a method for estimating the Fermi level of graphene. As shown in Figure1.11c, the estimate for $2|E_F|$ is given by the energy threshold, beyond which absorption increases.

As illustrated in Figure 1.12, optical transmission in graphene deviates significantly from the universal conductivity behavior, which is relevant only within the Dirac cone approximation, and peaks at $4.62eV$. The asymmetric peak observed at 4.62 eV is explained

by excitonic effects observed in graphene in a wide spectral range including the π band saddle point singularity [86]. Phenomenologically, the observed excitonic effect is explained as a Fano interference between a band continuum and a strongly coupled excitonic state [86].

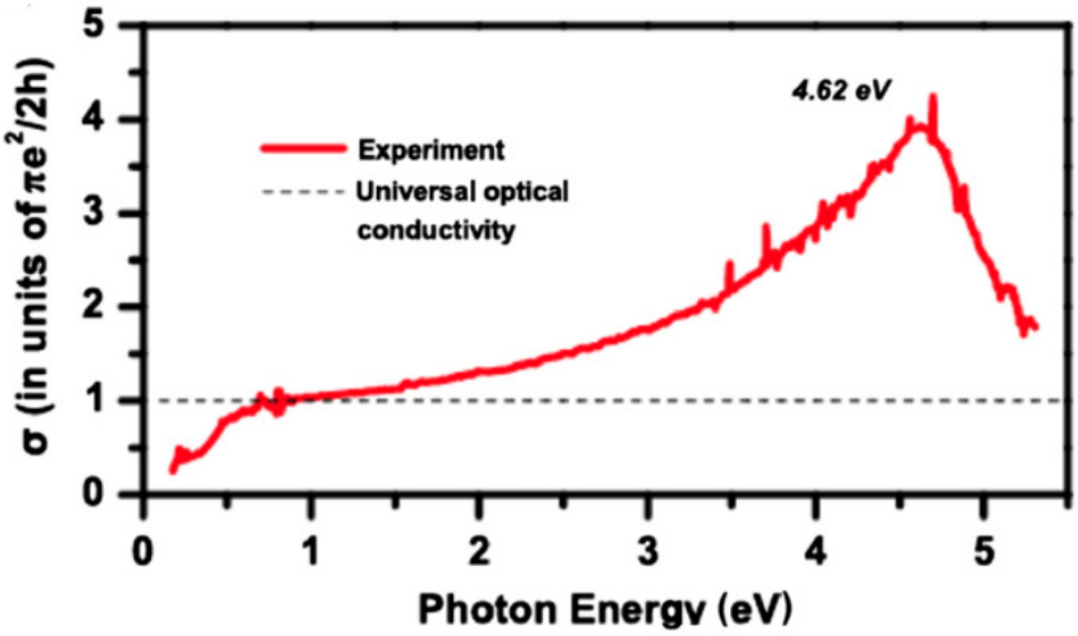

Figure 1.12: Experimental optical conductivity (solid red line) and universal conductivity (dashed line) of graphene in the 0.2 to 5.5 *eV* spectral range [7].

Chapter 2

Experimental techniques

2.1 Chemical vapor deposition graphene

Chemical vapor deposition (CVD) graphene growth is one of the most promising methods for transitioning graphene production into the industry due to large area of growth, high degree of control and reproducibility as well as the electrical properties comparable to exfoliated graphene [87, 88, 89, 90]. Since single layer graphene was successfully exfoliated [91], there have been attempts to grow larger area graphene on metals. Studies have shown that most transition metals are capable of catalyzing decomposition of hydrocarbons into graphitic materials [92]. However, copper has been widely used for CVD graphene growth due to extremely low carbon solubility and low cost. The surface catalysis ensures self-termination of the growth process, thus producing uniform single layer graphene on the surface.

2.1.1 CVD graphene growth

The growth of CVD graphene on copper foil is preceded by annealing the copper coil at high temperatures $\sim 1000^{o}C$ to remove oxides from the surface and subsequent exposure to a hydrocarbon precursor. The reactants from the precursor catalyzed on copper facilitate the nucleation of graphene. Low pressure of a few millitorrs employed in the growth process provides uniform deposition of single layer graphene membranes. CVD graphene growth kinetics has been thought to be dominated by crystallization from initially supersaturated surface with carbon adatoms. This in turn implies that after the nucleation stage the growth process is independent of hydrocarbon precursor addition. However, Celebi *et al.* [8] proposed an alternative growth model based on their observations supporting the claim that the growth is affected by adsorption-desorption dynamics as well as catalytic

dissociation and dehydrogenation of hydrocarbon precursors on copper. As illustrated in Figure 2.1, adsorption of the hydrocarbon precursor with subsequent catalytic decomposition and dehydrogenation results in a mixture of carbon adatoms, dimers and intermediate hydrocarbons on the copper surface. The mixture of reactants on the surface of copper can themselves go through dissociation and hydrogenation until they are attached to the lattice or desorbed. Desorption is augmented on the exposed surface due to copper sublimation. The reactants can diffuse around the surface and subsurface region of the copper foil as well as beneath the graphene flakes. Carbon reactants captured beneath the expanding graphene flakes are protected from sublimation enhanced desorption. Hence, the reactants on the surface can accumulate, while the graphene flakes continue to grow after the initial carbon supersaturation is depleted.

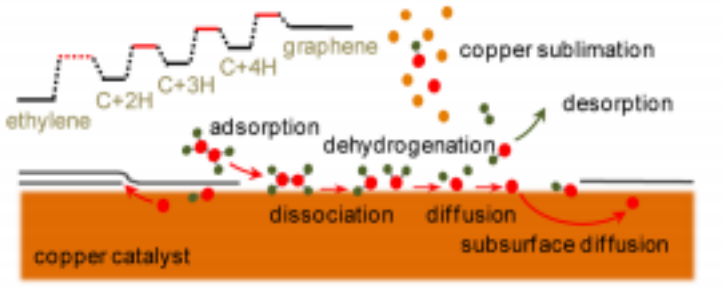

Figure 2.1: CVD graphene growth scheme and associated mechanisms [8].

2.1.2 CVD graphene transfer

CVD growth method provides high quality, large area graphene to address the need for mass fabrication, however, reliable transfer of large area single layer graphene onto desired substrates is an equally crucial step in using CVD graphene for practical applications. Poly-methyl methacrylate (PMMA) method has been widely used for small production of graphene. PMMA method has been employed as a support material for transferring carbon nanotubes [93] and mechanically exfoliated graphene flakes [94, 95] as well as for transferring CVD grown graphene onto substrates [96, 97]. Shortly described, PMMA is

spun on top of graphene to serve as a support material. Afterwards, the copper is etched away resulting in a standalone graphene membrane supported by PMMA. The PMMA/-graphene membrane can then be mechanically transferred onto a desired substrate. The PMMA layer is subsequently removed after transfer onto the desired substrate. The described transfer process is schematically shown in Figure 2.2. Despite the obvious advantages of the PMMA method such as simplicity and large areas, there are also disadvantages like the formation of cracks and wrinkles as well as difficulties in removing the PMMA residue. Previous research in our group addressed the issue and resulted in an optimized recipe yielding clean graphene with little amounts of the unwanted PMMA residue [5]. The PMMA coating is spun on top of a copper foil at 4500 rpm. The PMMA layer thickness depends on the spin coating speed as well as anisole concentrations as illustrated in Figure 2.3. In the past research of our group, the role of the parameters such as anisole concentration and the spin coated PMMA layer thickness was carefully studied [5]. According to the experiments, the thinner layer (40 nm) obtained by using A2 does not ensure the secure support of graphene required for all steps in the transfer. It was found that 180 nm of PMMA A4 is the optimum balance between support provided by the PMMA layer and thickness for effective removal [5]. It was noticed that small deformations in the copper foil result in inhomogeneous PMMA layer coverage during the spin coating process, which compromises the overall quality of transfer. It was found that a thermal release tape attached to the back of the copper foil helps to mitigate deformations of the copper surface by the vacuum suction, thus contributing to the improvement of graphene transfer [5].

Etching process of the copper foil is a critical step in the CVD graphene transfer. The choice of an etchant has implications for the quality of graphene. Ferric Chloride ($FeCl_3$) is generally favored due to slow etching rate. Absence of bubbles during the etching process is another advantage of Ferric Chloride, which makes it more favorable when compared to etchants like HNO_3, which generate H_2 bubbles during the copper etching leading to tears and cracks. After etching away the copper foil, the floating PMMA/graphene membrane

floating must be properly cleaned of the copper etchant to ensure high quality transfer. If the PMMA/graphene membrane is not properly cleaned of the copper etchant residue, a layer between graphene and the substrate may be formed leading to deterioration of transfer quality. It is generally suggested to do a few deionized water baths for 10-60 minutes. However, according to the previous research in the group the suggested amount of time may not be enough for thorough cleaning. It was found that doing multiple baths and leaving the PMMA/graphene layer in deionized water for over 24 hour period leads to better results.

The PMMA removal is the last step in the CVD graphene transfer process, the importance of which can be hardly underestimated. As illustrated in Figure 2.4, the difference between a clean graphene transfer and an inferior one with an insufficient PMMA removal can be quite dramatic. The polymer residue of a few nanometer thickness remaining on the graphene surface after treatment with organic solvents is considered to be one of the major disadvantages of the PMMA method. For instance, the remaining PMMA on the surface has been shown to cause a weak p doping in graphene [98]. The bulk of PMMA is generally removed by dissolving the polymer in acetone and afterwards rinsing with isopropanol. In order to enhance the PMMA removal it was experimented with leaving samples in acetone for different periods of time up to 48 hours, heated acetone baths and sonicating the samples in acetone, which showed to result in smaller amounts of the PMMA residue, although a thin PMMA residue still remained on the samples indicating that the use of acetone alone does not ensure the complete PMMA removal [5].

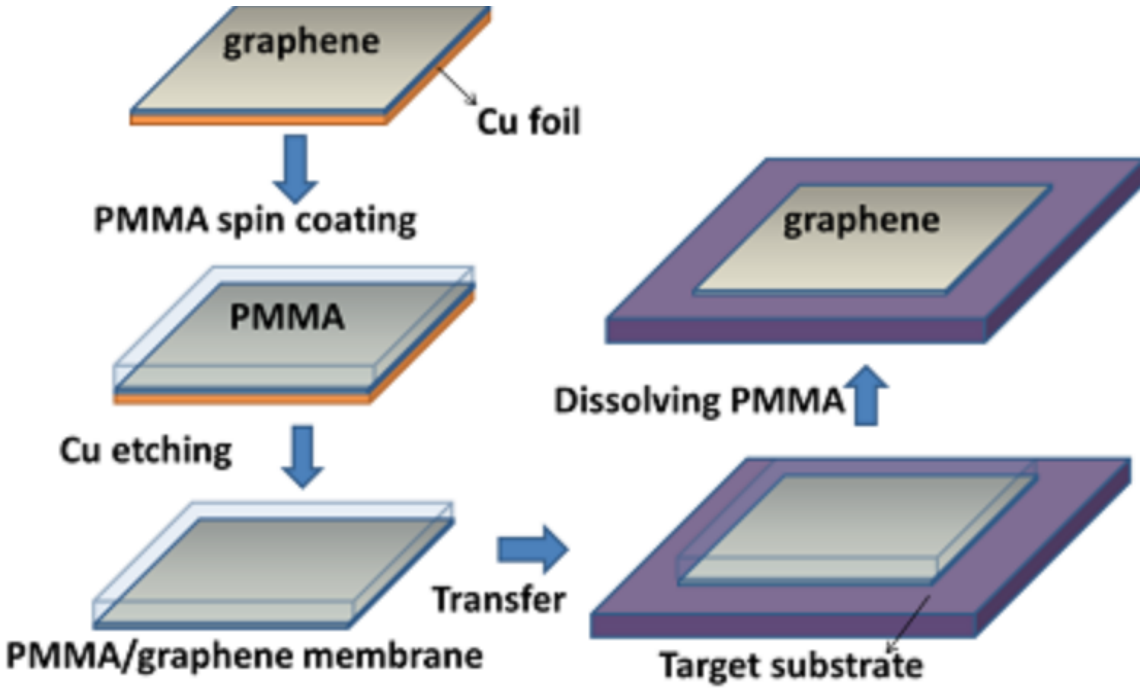

Figure 2.2: The CVD graphene transfer process.

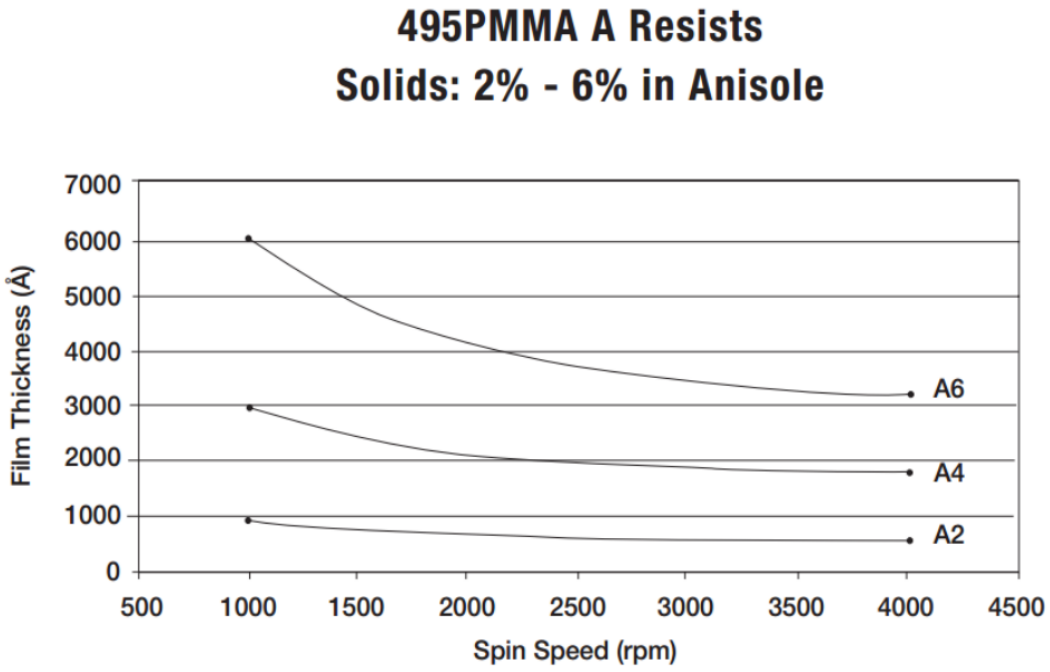

Figure 2.3: PMMA layer thickness dependence on the spin speed for different anisole concentrations [5].

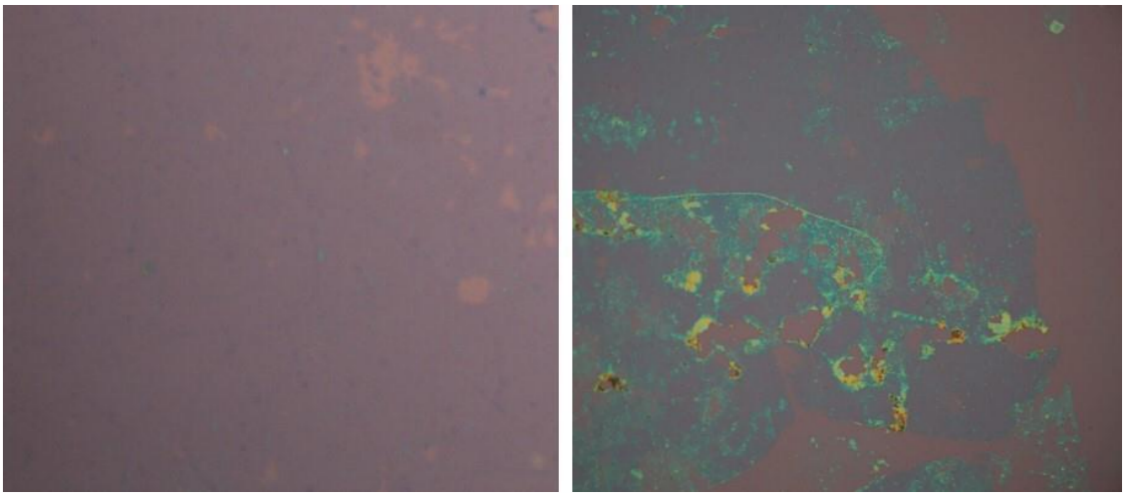

Figure 2.4: Single layer graphene on SiO_2/Si substrates with and without PMMA residue [5].

Thermal annealing in gaseous atmospheres is known to complement the solvent cleaning for improving the PMMA residue removal. Specifically, there have been studies on annealing graphene in argon and hydrogen gases as well as their mixtures [99, 100, 101]. Annealing in ultra-high vacuum significantly enhancing the mobility of CVD graphene [98] complemented by annealing in oxygen and hydrogen/argon has been demonstrated to be effective in removing the PMMA residue [102]. Experiments performed in the previous research of the group revealed that the best results are achieved by a two-step thermal annealing after removing the most of the PMMA residue by solvents treatment. The two-step annealing process is more advantageous in view of lesser contamination of the chamber due to lower amounts of the PMMA remnants. The best results were obtained by first annealing the samples at 300^oC on a hot plate for 30 minutes in ambient air and then hot furnace annealing in argon or hydrogen at 400^oC for 3 hours [5].

2.2 Graphene characterization by Raman Spectroscopy

Light impinging on a crystal can be reflected, transmitted, absorbed or scattered depending on the light wavelength and the crystal energy band structure. Elastic light scatter-

ing also known as Rayleigh scattering involves no change in the wavelength of the scattered light. Elastic scattering occurs when the radius of particles is much smaller than the wavelength of the incoming light. Inelastic light scattering results in the wavelength change of the scattered light. During the interaction process schematically illustrated in Figure 2.5 , incident light of frequency ω_1 and wave vector $\mathbf{k}_1$ is scattered by a phonon (or other excitations) of frequency Ω and wave vector $\mathbf{q}$. The scattered light has frequency ω_2 and wave vector $\mathbf{k}_2$. Particularly, Raman scattering is inelastic light scattering from optical phonons.

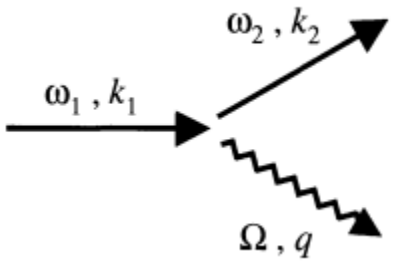

Figure 2.5: An inelastic light scattering process [9].

As a result of Raman scattering, the scattered photon can either gain (Stokes) or lose (Anti-Stokes) energy. The law of energy conservation demands that $\hbar\omega_{Sc} = \hbar\omega_L \pm \hbar\Omega$, where the positive sign is for the Anti-Stokes process and the negative sign is for the Stokes process.The two processes are outlined in Figure 2.6. The ratio of the Stokes and Anti-Stokes events is given by [9]

$$\frac{I_{Anti-Stokes}}{I_{Stokes}} = \exp(-\frac{\hbar\Omega}{k_B T}) \tag{2.1}$$

Non-resonant Raman scattering occurs when the energy of an incoming photon does not match transition energy to a stationary state. If the photon energy is chosen to cause transition to a specific energy level, resonant Raman scattering takes place. Raman spectroscopy is a widely used characterization tool for determining graphene layer number, strain and doping. Rayleigh scattering signal exceeds Raman scattering by a few orders of magnitude, which used to be an obstacle in extraction of the Raman signal. With the invention of

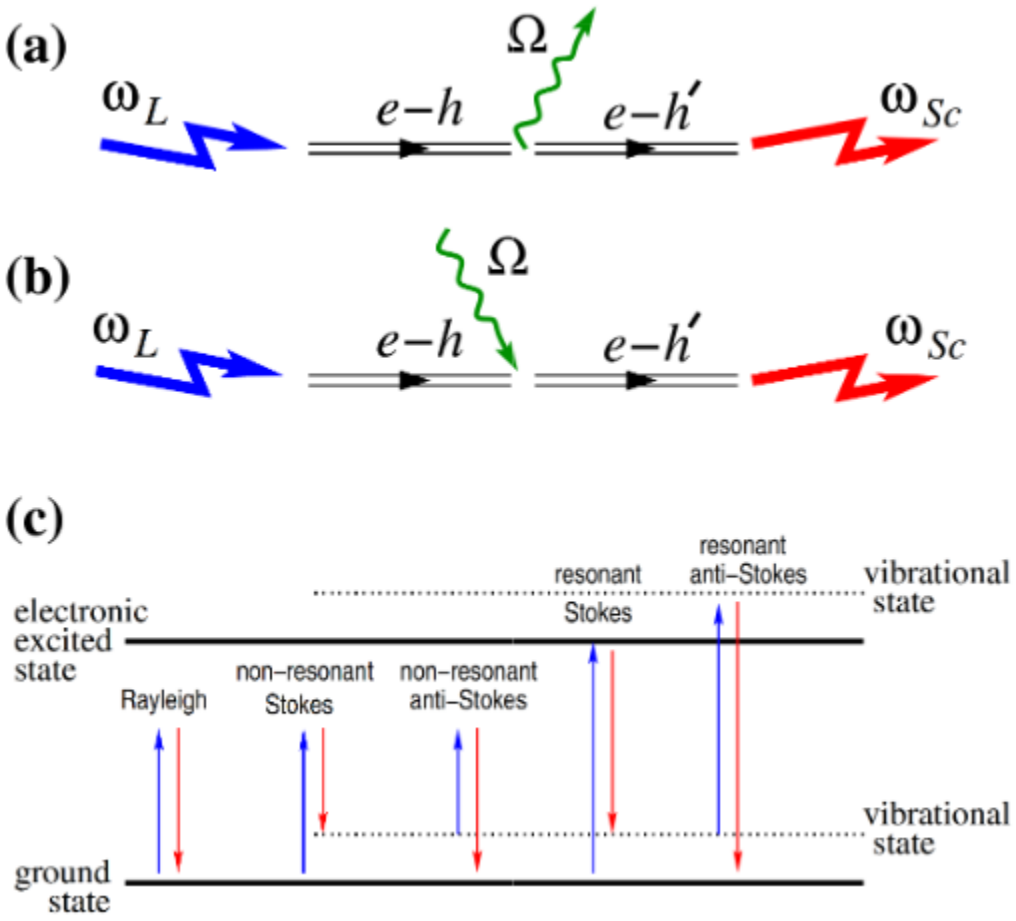

Figure 2.6: Raman Scattering [10]. a) The Stokes process. b) The Anti-Stokes process. c) Resonant and non-resonant Rayleigh and Raman scattering.

monochromatic light sources and selective light filters Raman spectroscopy has become a universal tool for characterization of materials. Since 2006 it has been demonstrated that Raman spectroscopy is a powerful technique for determining graphene layer number [103], defect concentration [104, 105], doping [106, 14, 107] and strain [108, 109, 110]. Raman spectroscopy is well suited for studying atomic and electronic structure of graphene due to the zero band gap and any incident wavelength resonance. Interaction of electrons and phonons is crucial to Raman scattering, which means that altering of the electronic properties of graphene by applying the electric/magnetic field or doping has effect on position, width and intensity of the Raman peaks [111, 112].

Analysis of the origin of Raman peaks in single layer graphene requires understanding of the phonon properties. Phonon dispersion curves bear close relation upon the fundamental properties of solid state materials such as heat capacity, thermal conductivity, velocity of sound, electron-phonon and phonon-phonon interactions. The graphene phonon modes and their dispersion have been studied by a number of groups [113, 114, 115, 116]. Since graphene has two carbon atoms per unit cell, the phonon dispersion of single layer graphene consists of three acoustic and three optical branches as illustrated in Figure 2.8. One branch from each family corresponds to the out of plane vibrational mode. The other two branches correspond to the in plane transverse and longitudinal modes. The low mass of carbon and the sp^2 bonds result in high energy lattice vibrations. For instance, the optical phonon energy at Γ point is approximately 200 meV. The optical phonon branch is strongly Raman active due to the inversion symmetry. The electronic Brillouin zones (BZ), the first phonon BZ and schematic electronic dispersion are given in Figure 2.7.

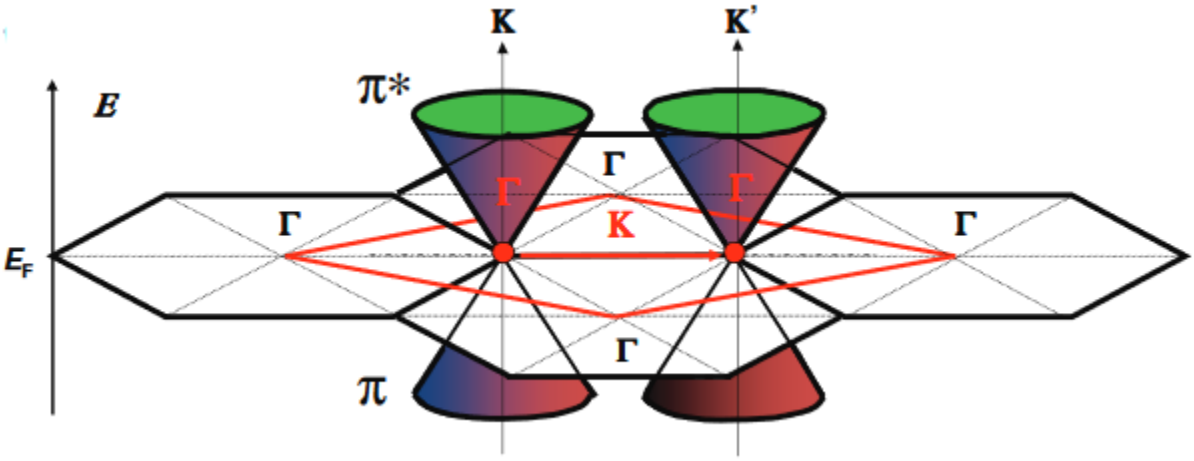

Figure 2.7: Electronic BZs of graphene (black hexagons), the first phonon BZ (red rhombus), and schematic electronic dispersion [10].

The laws of energy and momentum conservation in Raman scattering give

$$\omega_L = \omega_{Sc} \pm \Omega, \tag{2.2}$$

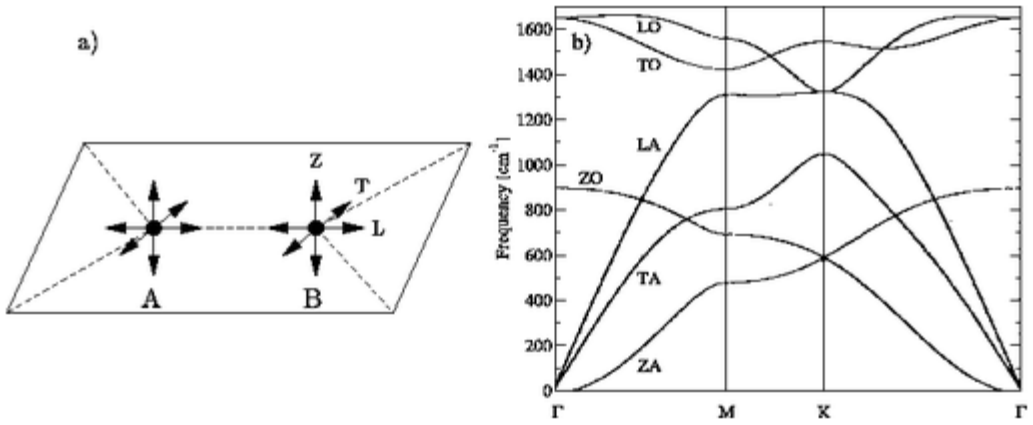

Figure 2.8: a) Vibrations of carbon atoms in graphene along the out of plane (Z), in plane transverse (T) and in plane longitudinal (L) directions. b) The phonon dispersion branches for a single layer graphene [11].

$$\mathbf{k}_L = \mathbf{k}_{Sc} \pm \mathbf{q}, \tag{2.3}$$

where the positive and negative signs pertain to the Stokes and Anti-Stoke processes, respectively. Typical light wavelength used in Raman measurements is in the 229 - 1064 nm range [117, 10]. The lattice parameter a is on the order of a few Å. Particularly, it is equal to 1.42 Å in graphene [118]. Then, the magnitudes of light wavevectors are much smaller than the magnitude of a zone boundary vector $k_L, k_{Sc} \ll \pi/a$. Hence, it follows from the energy and momentum conservation laws that $q \ll \pi/a$. In other words, only scattering from phonons near Γ point is measured because $q \approx 0$. The acoustic phonon branch properties are usually provided by the thermal conductivity measurements as the acoustic phonons are the major heat carriers at room temperature in graphene [119]. Enhanced phonon boundary scattering and modified phonon dispersion as well as density of states in semiconductor nanowires and thin films as compared to their 3D bulk states deteriorate acoustic phonon transport and heat transfer [120, 121]. However, graphene has been demonstrated to have an extremely high thermal conductivity due to quite different phonon transport properties as compared to graphite [122]. Owing to the strong sp^2 carbon bonds, graphene has a large in-plane phonon group velocity. Despite graphene being a semimetal, the heat transfer is

mostly due to the acoustic phonons [123].

A typical Raman spectrum of single layer graphene is shown on Figure 2.9. The three main features of the graphene Raman spectrum are the G peak, the D peak and the 2D peak with neutral positions at $\sim 1580\ cm^{-1}$, $\sim 1350\ cm^{-1}$ and $\sim 2700\ cm^{-1}$, respectively [124, 125, 126, 103, 10] The G peak originates from the high frequency E_{2g} phonon at Γ

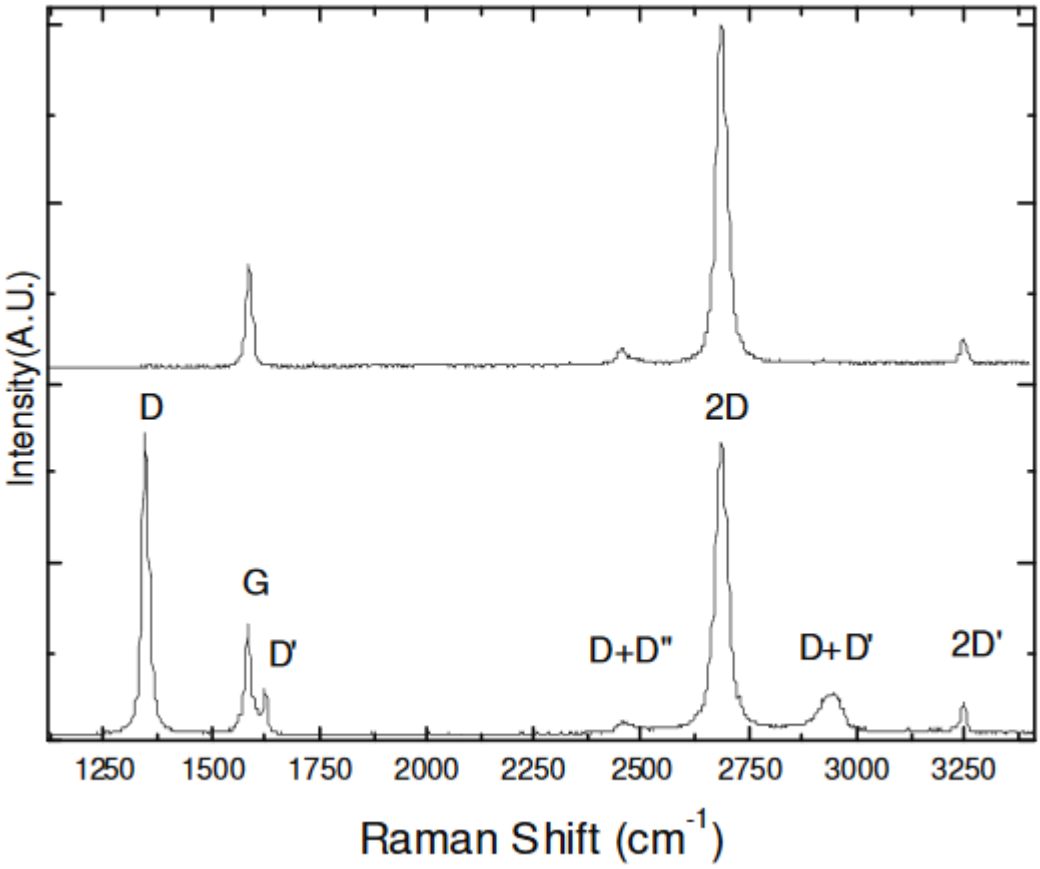

Figure 2.9: Raman spectra of pristine (top) and defected (bottom) graphene [10].

point (Figure 2.11). The D peak reveals itself only in the presence of defects and is due to the breathing modes of six-atom rings (Figure 2.11) [127, 117, 128]. It stems from TO phonons around the BZ edge K [127, 117]. The derivatives of the phonon dispersion curves show jump discontinuities at the Γ and K points of the TO and LO branches, respectively, which are called Kohn anomalies (see Figure 2.10). The D peak is activated by double resonance [128, 129] and is strongly dispersive with respect to excitation energy [130] due

to a Kohn anomaly at K. The D' peak is due to double resonance occurring as intra-valley process by connecting two points of the same cone around K (or K'). The 2D and 2D' peaks are the overtones of the D and D' peaks, respectively. The 2D and 2D' peaks are always revealed in Raman spectra of graphene as they do not require a defect for activation, which is due to the fact that these peaks originate from a process involving two phonons with opposite wavevectors, thus satisfying momentum conservation [131, 132]. The slope of Kohn anomalies bears direct relationship to the electron-phonon coupling strength. The electron-phonon coupling is much stronger at the Γ and K points due to the steepest slopes as compared to other points in the graphene Brillouin zone. Therefore, the Raman peaks corresponding to the phonons at the Γ and K points are dominant.

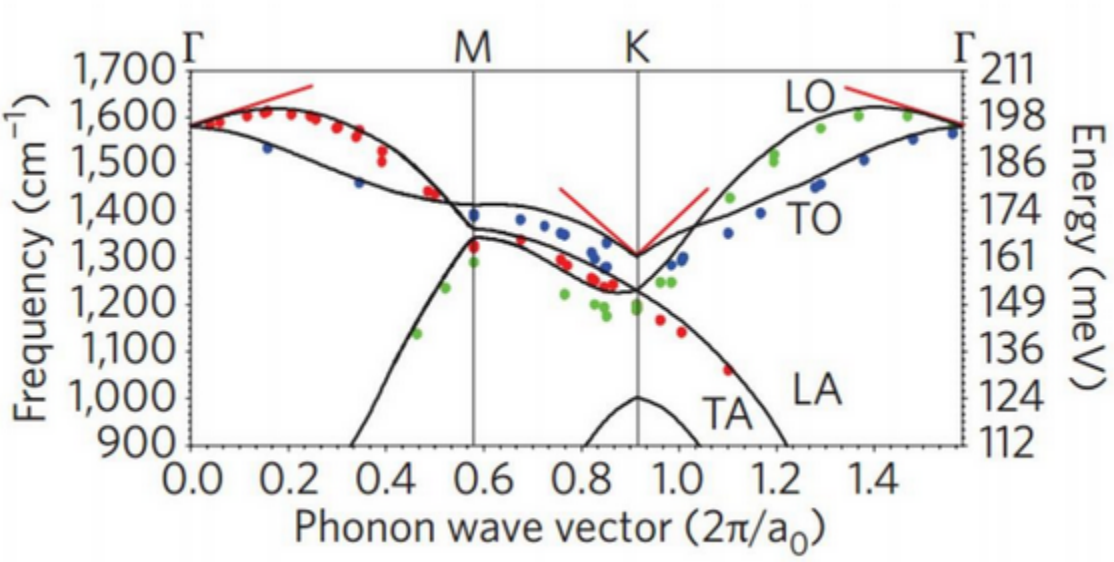

Figure 2.10: The optical phonon dispersions in single layer graphene relevant for the interpretation of Raman spectra [10].

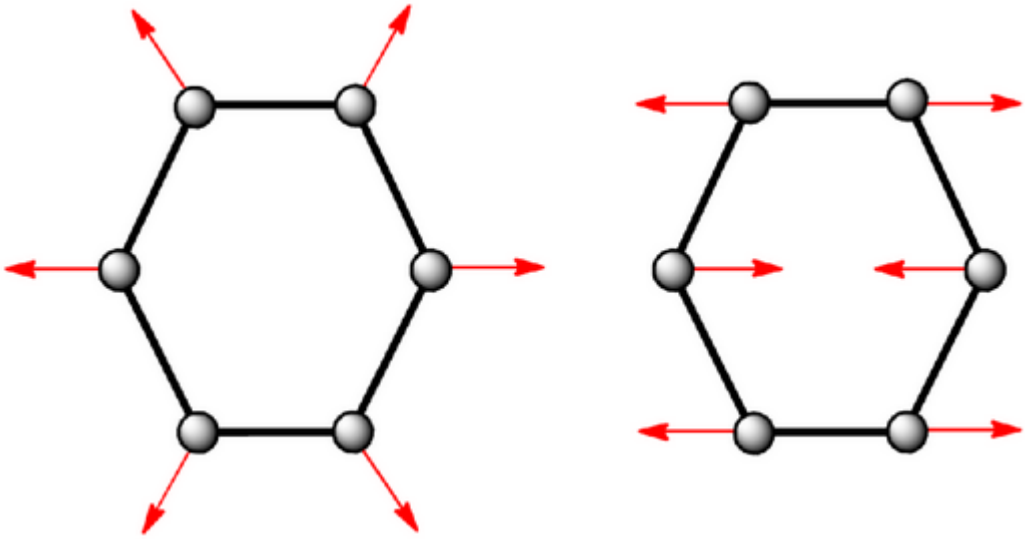

Figure 2.11: E_{2g} vibrational mode (right) gives rise to the G peak in the Raman spectrum. The D and 2D peaks come from A_{1g} breathing mode (left).

The Raman processes corresponding to the origins of the Raman peaks in graphene are illustrated in Figure 2.12. The single phonon process due to the carbon bonds' in-plane stretching modes of vibration at the Γ point give rise to the G peak in the graphene Raman spectrum. An incoming photon generates an electron-hole pair. Then the electron loses energy by phonon emission with wave vector $q = 0$. Upon recombination of the electron with the hole a lower energy photon is emitted, thus observing the laws of energy and momentum conservation. Some single phonon processes may be deactivated by doping as illustrated by a crossed process in Figure 2.12a. The intensity of the G peak increases with the stronger electron-phonon coupling. The phonon wave vector does not have to be zero in the presence of defects in graphene lattice, thus producing the D' and D peaks stemming from intravalley (Figure 2.12b,c) and intervalley (Figure 2.12d-g) scattering mechanisms, respectively. Raman processes illustrated in Figure 2.12b-e involve both an electron and a hole participating in one event of scattering each. As shown in Figure 2.12f,g, there are also contributions from the events, in which only the electron or the hole is scattered. For the two phonon processes momentum conservation can be observed by emitting phonons

with opposite wave vectors. The two phonon processes produce the 2D' peak and the 2D, D+D" peaks occurring due to intravalley (Figure 2.12h) and intervalley (Figure 2.12i-k) scattering, respectively. The two phonon processes, where only the electron or the hole is scattered correspond to Figure 2.12j,k. In the presence of defects, D+D' is produced as a result of one intravalley and one intervalley phonon emission. The contribution from the processes in Figure 2.12f,g,j,k is small. Since the Raman process responsible for the 2D peak does not involve virtual states, the process is, therefore, triple resonant, which explains the highest intensity of the 2D peak.

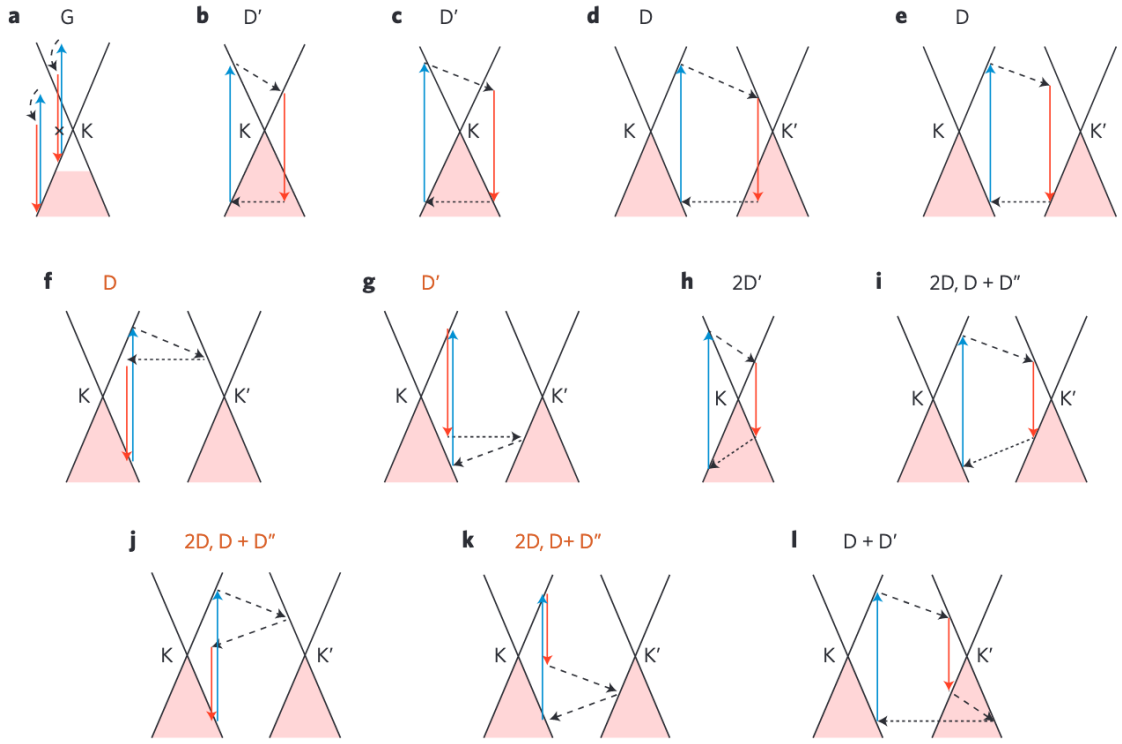

Figure 2.12: Raman processes in graphene. Solid black lines represent electronic dispersion. Shaded areas illustrate occupied states. Blue and red arrows are direct interband transitions occurring by photon absorption or emission, respectively. Dashed arrows indicate intraband transitions by phonon emission. Horizontal dotted arrows represent scattering on a defect[10].

The dependece of the Raman response on the number of graphene layers has made Raman spectroscopy an indispensable and versatile characterization tool. Atomic force

microscopy used to be the only tool for distinguishing between single layer and multiple layer graphene until the capabilities of Raman spectroscopy in identification of graphene layer numbers were demonstrated in 2006 by Ferrari *et al.* [131]. Atomic force microscopy method has its limitations in view of the problems stemming from the existence of wrinkles and folds in graphene. Due to the resonant nature of the 2D peak Raman spectroscopy has become a unique tool for determining the number of graphene layers in a fast and non-destructive manner. The modification of the electronic bands by the layer number as well as the different band structure of single layer and bi-layer graphene result in distinct Raman spectra. The band structure and the double resonant processes are illustrated in Figure 2.13. The interaction between the layers of graphene splits the π and π^* bands into four bands. Hence, the band structure of bi-layer graphene consists of four parabolic bands [133] unlike the linear nature of the band structure of single layer graphene in the vicinity of the K point. The incident photons couple to two of these bands, whereas the TO phonons can couple to all four of the bands. Hence, the 2D peak of bi-layer graphene is influenced by all four double resonant scattering processes, which implies that the 2D peak is the sum of the four Lorentzians, while single layer graphene exhibits a single symmetric Lorentzian 2D peak.

The vibrational and electronic properties associated with bi-layer graphene are dependent on the relative position and the stacking order of the layers. In general, any relative orientation of the two layers is possible. However, the most common stacking order often encountered in graphene is the AB (Bernal) stacking illustrated in Figure 2.14c. The AA stacking configuration in Figure 2.14b is not energetically stable, hence it is not encountered in multilayer graphene structures. The Turbostratic stacking (Figure 2.14d) refers to the stacking configurations with the absence of rotational order. As the electronic band structure of graphene is dependent on the stacking order of layers, the 2D peak in Raman spectroscopy of graphene is influenced by the number of layers as well as the stacking configurations.

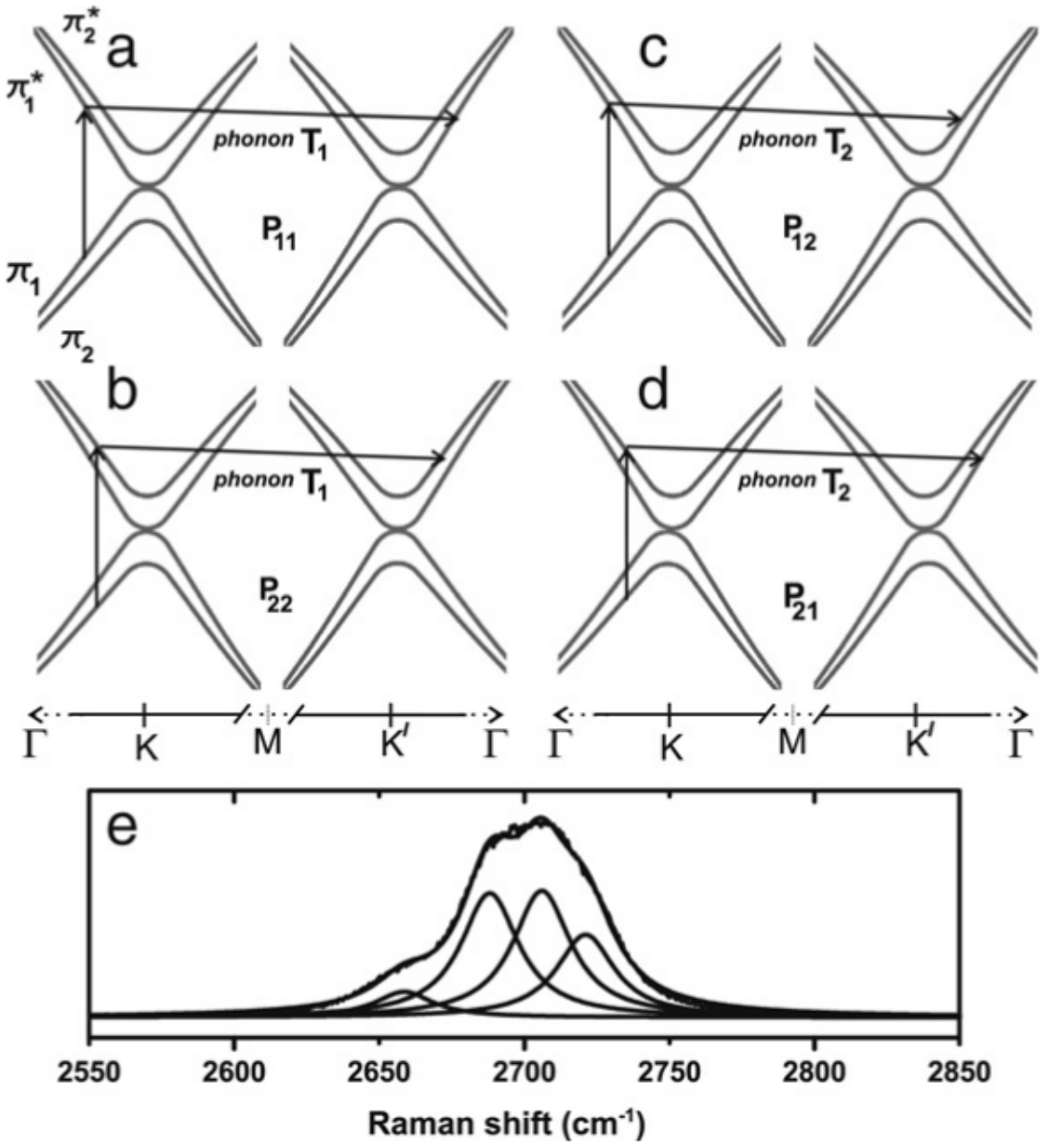

Figure 2.13: a)-d) The schematic electronic dispersion of bi-layer graphene near the K and K' points with π_1 and π_2 bands and the double resonant processes. e) The measured 2D peak with fitted Lorentzians[12].

Hence, the shape of the 2D peak pertains to the interactions between layers in multilayer graphene. It is known that multilayer graphene in turbostratic stacking configuration shows a single Lorentzian 2D peak [134], which implies that the single Lorentzian shape of the 2D peak alone should not be identified with single layer graphene. The similarity of the 2D peak shapes can be explained by the very weak interaction between layers in the turbostratic

stacking configuration as compared to AB stacked graphene [13]. However, in the case of turbostractic graphene, the position of the 2D peak is shifted by approximately 20 cm^{-1} and the FWHM (full width at half maximum) is doubled as compared to single layer graphene. It has been also demonstrated that the area ratio of the 2D and G bands could indicate stacking configuration of graphene [13].

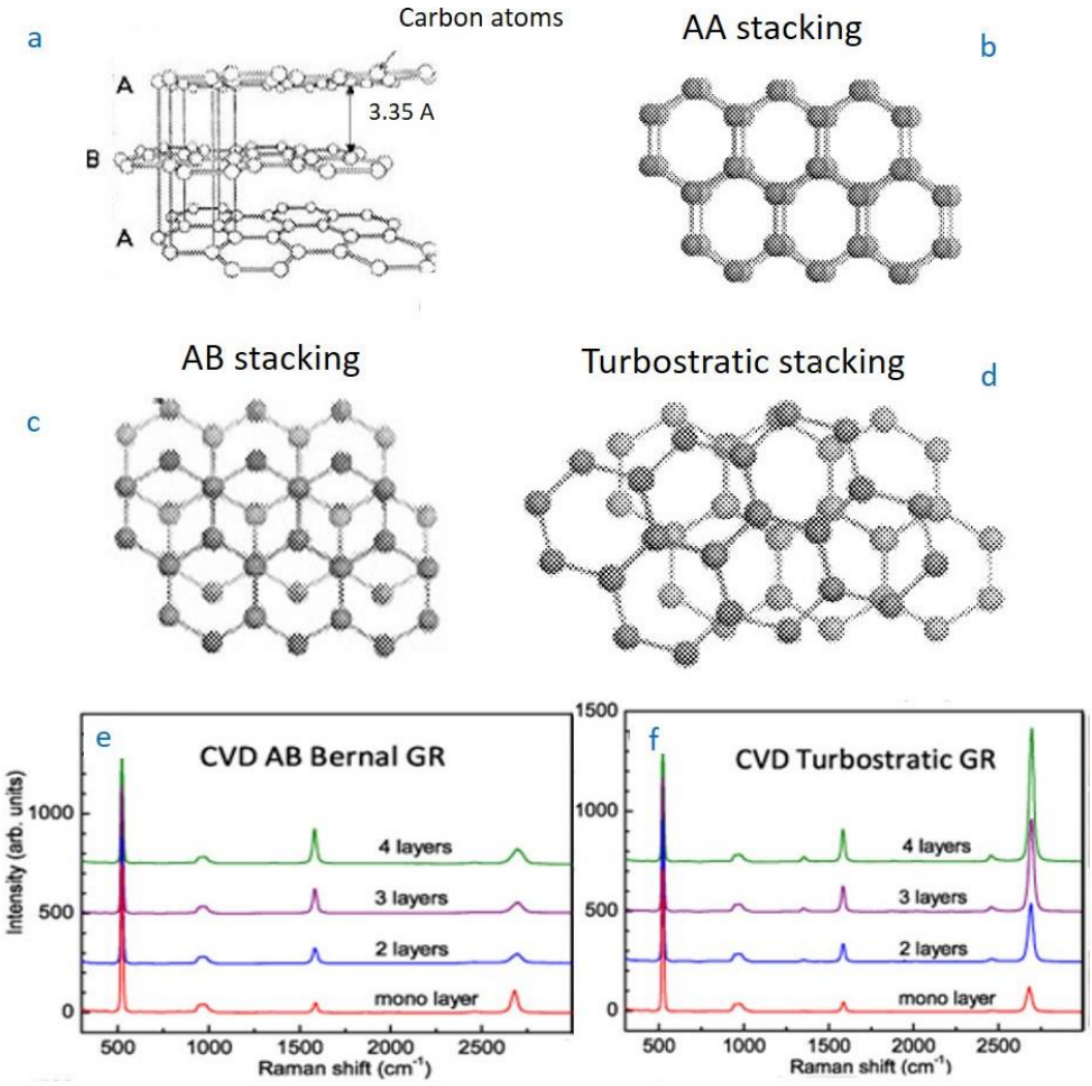

Figure 2.14: a)-d) The stacking order configurations of bi-layer graphene [5]. e),f) Raman spectra of CVD graphene in Bernal and Turbostratic stacking configurations[13].

As discussed before, defects in graphene render single phonon scattering possible without violation of the Raman selection rules. The D and D' peaks arise from the elastic scatter-

ing by a defect in graphene lattice. Specifically, the D peak originates from the intervalley scattering of TO phonons near the K point, while the D' peak stems from the intravalley scattering of LO phonons near the Γ point. Hence, edges and grain boundaries in graphene are related to the occurrence of the D peak in Raman spectrum owing to the sensitivity of the D peak to the lattice defects and dislocations. Thus, Raman spectroscopy is an effective technique for identification and quantification of the lattice defects in graphene. The seminal paper by Tuinstra and Koenig demonstrated that the intensity ratio of the D and G peaks is inversely proportional to the crystal size of graphene:

$$\frac{I(D)}{I(G)} = \frac{C(\lambda)}{L_a}, \tag{2.4}$$

where $C(514\ nm) \sim 4.4\ nm$ [127, 135, 136]. It is understood in theory as well as experimentally verified that the D peak is generated in a small region of the crystal ($\sim 3-4\ nm$) in close proximity to a defect or an edge [137, 138, 139, 140]. Thus, the intensity ratio of the D and G peaks provides a quick way of estimating the presence and concentration of defects in the graphene lattice.

Raman spectroscopy finds one of its most extensive uses in application to determination of the electron-hole doping levels due to the dependence of the G and 2D peaks on the electronic doping. The effect of doping on the Raman peaks was studied by Das *et al.* [14] by using electrochemical top gating to induce a wide range of doping levels accompanied by in situ Raman measurements to track changes in the Raman spectrum corresponding to different carrier concentrations. A gate voltage creating potential difference between the gate electrode and graphene changes the electron concentration, which in turn shifts the Fermi level position. The Fermi energy dependent on the electron concentration can be written as $E_F(n) = \hbar|\upsilon_F|\sqrt{\pi n}$ with υ_F and n denoting the Fermi velocity and the electron concentration in cm^{-2}, respectively. The applied top gate voltage changes the electron

concentration according to the following equation [14]:

$$V_{TG}(volts) = 1.16 \times 10^{-7}\sqrt{n} + 0.723 \times 10^{-13} n, \tag{2.5}$$

where n is in units of cm^{-2}. As seen from Figure 2.15 [14], in situ Raman measurements reveal that the position and the FWHM of the G peak are both affected by the doping concentrations. The stiffening and sharpening of the G peak occurs with increasing doping levels. Excess carriers introduced by doping induce the crystal lattice to expand or contract causing the equilibrium lattice constant to change, which modifies the phonon properties and entails the changes in the G peak position. The shift of the G peak position to higher energies is considered to be caused by the non-adiabtic elimination of Kohn anomaly at the Γ point [141]. The sharpening of the G peak, i.e. the decrease in the FWHM, is caused by the elimination of the phonon to electron-hole pair decay path due to the Pauli blocking [14]. As demonstrated in Figure 2.15a,b, the Fermi level and carrier concentration may be estimated from the G peak position shift. However, the G peak alone does not provide any information on the type of the doping because it shifts in the same direction for both electron and hole doping. The shift in the 2D peak position can be used instead to determine the doping type. As seen from Figure 2.15c, the 2D peak position is shifted to lower energies for the electron doping and towards higher energies for the hole doping [14]. The changes in the 2D peak position with doping are likewise explained in terms of the modification of the lattice parameters by the excess charge resulting in altered phonon properties. It can also be noted from Figure 2.15a that the intensity of the 2D peak decreases with the electron or hole doping, which can be understood by considering the changes in the scattering rates of charge carriers [142].

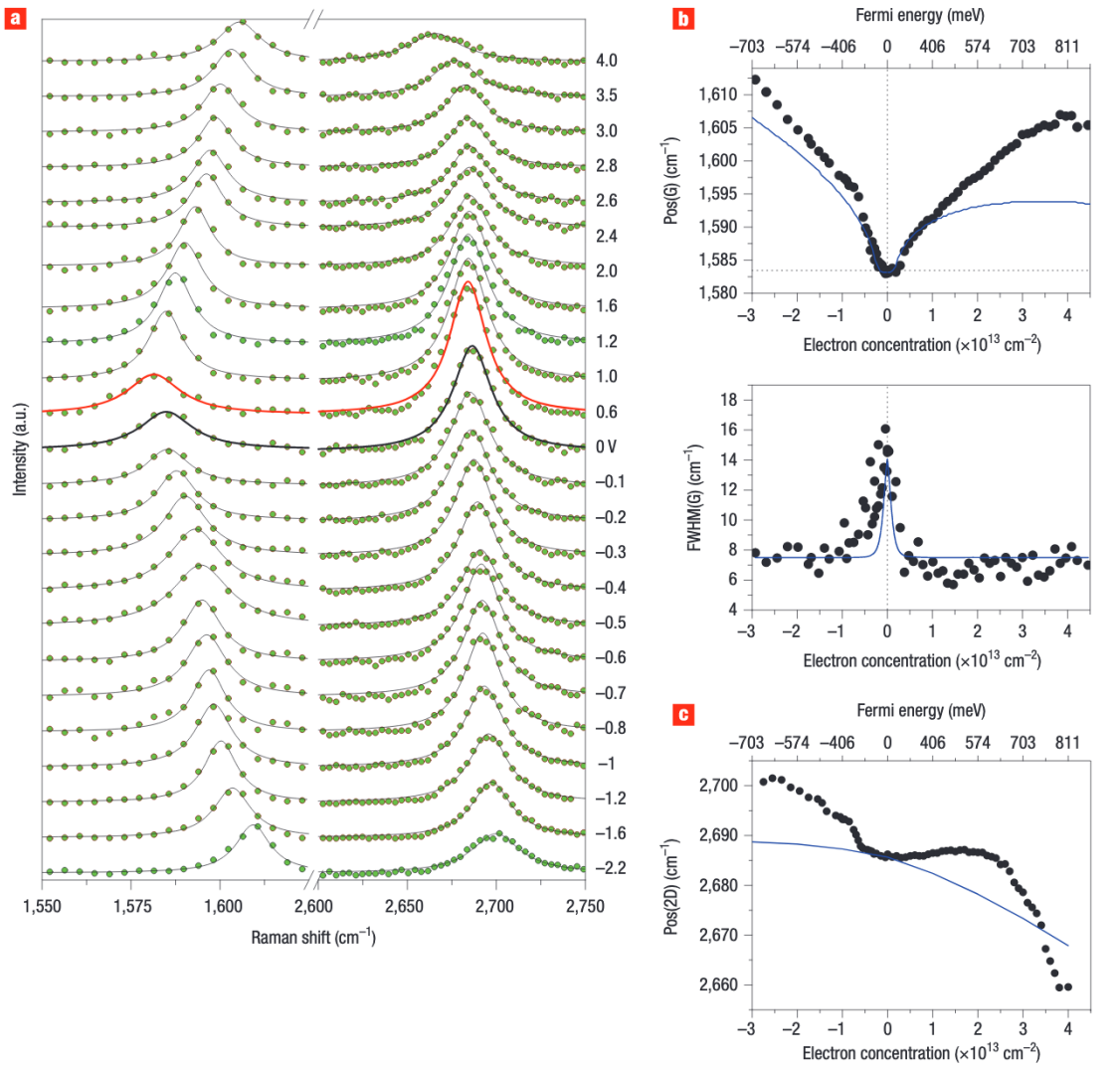

Figure 2.15: a) In situ Raman spectra of graphene measured as a function of gate voltage. b) The G peak position and its FWHM as a function of Fermi level (electron concentration). c) The 2D peak position as function of Fermi level (electron concentration)[14].

2.3 Ultrafast pump-probe measurements

The observed electronic and optical material properties stem from a complex combination of lattice, electronic and spin related phenomena generally occurring on a timescale ranging from 10^{-18} to 10^{-9}s. Standard electrical measurement techniques typically involve the use of the electrical apparatus such as network analyzers and capacitance ridge circuits as well as a wide variety of other different methods. The temporal resolution of these electrical measurements techniques is limited by a maximum bandwidth determined by the response time constant *RC* of the system circuit components. Electronic signals faster than the response time constant are rapidly suppressed and, hence, cannot be detected by the measurement apparatus. Thus, modern electrical measurement techniques are capable of resolving electrical signals on timescales exceeding 0.1 *ns*. On a shorter timescale less that 0.1 *ns* other nonelectrical methods must be used in order to bypass the response time limitation.

Experimental techniques allowing us to measure time evolution of the material properties on a femtosecond timescale transformed understanding of the electronic and optical properties. Pump-probe spectroscopy is probably the simplest ultrafast optical technique. In a typical pump-probe experiment, a high-intensity pump pulse perturbs and drives the system out of equilibrium and a time-delayed weak probe pulse measures changes in the transmission or reflection due to the photoexcitation as a function of time delay. Electronic detection limitation is bypassed by using sampling techniques in pump-probe measurements and reconstructing the dynamical response on a femtosecond timescale. Pump-probe spectroscopy has been successfully applied to study the nonequilibrium dynamics of the electron-electron interactions, the coupling phenomena between electrons, phonons and spins etc.

Pump-probe spectroscopy measurements give transient changes in optical properties with a time resolution greatly exceeding the limitations of the system electronics. As outlined above, the superior temporal resolution beyond the response time limitations of the

electronics is achieved by employing a sampling technique to reconstruct the signal. The full ultrafast signal in the time domain is not obtained at once in a single measurement. The ultrafast pump-probe signal is reconstructed by measuring the pump induced changes in the transmission of reflection multiple times for each particular time delay by means of the probe beam. Hence, each individual data point on a pump-probe spectrum is the average signal over many reflected or transmitted probe pulses at a particular time delay, which eliminates the detector electronics response time as a limiting factor of the temporal resolution. In an ultrafast pump-probe experiment, limitation on the minimum temporal resolution is imposed by the duration of the pump and probe pulses as well as the minimum step of a time delay stage. Thus, ultrafast pump-probe spectroscopy enhances time resolution to less than 50 fs despite the detector response time being much greater than 0.1 ns.

An example of a degenerate, noncollinear pump-probe setup is shown schematically on Figure 2.16. The laser beam incident on a beam splitter is separated into two components.

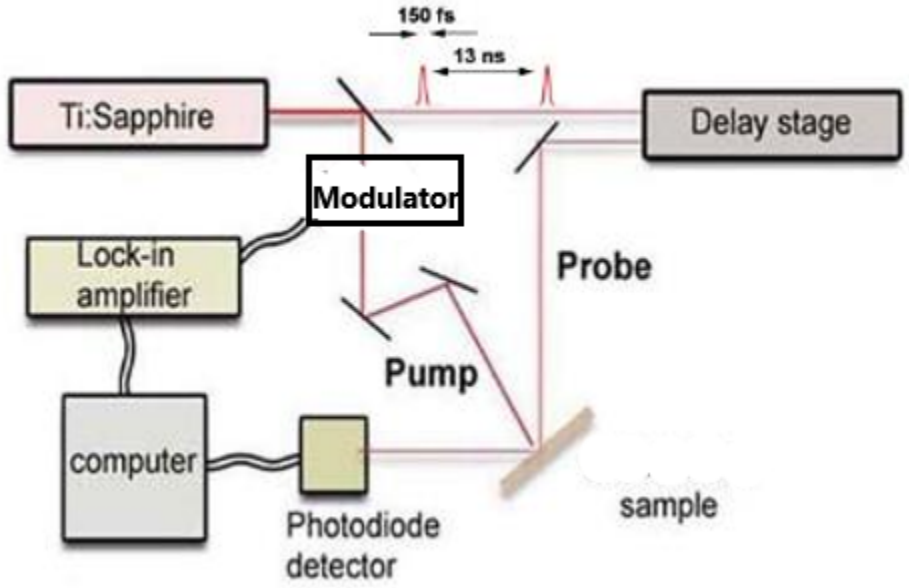

Figure 2.16: A degenerate, noncollinear pump-probe setup in reflection geometry.

The transmitted beam carries the biggest part of optical power and, hence, acts as a pump

to drive the system under study out of equilibrium. The reflected beam has much less of optical power and becomes a probe, which measures the state of a sample at a certain time delay arising from the difference in the pump and probe path lengths. The pump beam is usually sent through a broadband half-wave plate so that it becomes ŝ polarized, which perpendicular to the probe beam polarization p̂. An optical chopper is used to modulate the pump beam at a frequency of a few kHz, which is used as the reference input for a lock-in amplifier. The pump beam is focused on a sample by means of a lens or off-axis parabolic mirror. The lens for the pump beam has to have a shorter focal length as compared to a lens used to focus the probe beam so that the pump spot is larger than the probe spot. The ratio of the pump-probe power should be ideally greater than 10:1 so that the probe beam itself does not significantly alter the material properties at each time delay. The probe beam travels through a delay stage with variable length. The relative time of the pump and probe incidence on the sample is controlled by varying the length of the delay stage. Hence, the delay stage is responsible for the temporal delay and the ultrafast resolution. The minimum step size of the stage and the laser pulse width together determine the limit of the temporal resolution. The probe beam is then focused onto the surface of the sample and spatially overlapped with the pump beam spot. The probe beam spot size should be at least twice smaller than the pump beam spot so that the probe only samples the uniformly excited region, which cam be achieved by using a lens with a smaller focal length having a smaller diffraction limited spot size. Since the pump and the probe wavelengths are identical in degenerate pump-probe spectroscopy, it makes it difficult to isolate the transmitted or reflected probe beam from the scattered pump light, which is different from nondegenerate ultrafast pump-probe spectroscopy, where the problem can be solved by using a wavelength filter blocking the pump and transmitting the probe. Thus, in a degenerate pump-probe spectroscopy a significant background signal is present due to both the pump and the probe beams having a component at the chopper frequency and the lock-in amplifier being unable to distinguish between them. Therefore, the polarization

optics are the indispensable components of the equipment required in this experiment to prevent the pump beam from dominating the signal and saturating the lock-in amplifier. The polarization of the pump beam is turned into $\hat{s}$ by the half-wave plate before incidence on the sample. A polarizing cube beam splitter or broadband polarizer is positioned before the detector to split the $\hat{s}$ polarized pump beam from the $\hat{p}$ polarized probe beam. After passing through the polarizing beam splitter, the probe beam is focused on a detector and the pump beam is diverted in a different path. The probe light incident on a detector is then converted into an electrical signal. As mentioned before, the detector does not need to have a tera- or petahertz bandwidth to measure the ultrafast pump-probe signal. Instead, the detector must have the time resolution at the chopper frequency. A lock-in amplifier then measures the electrical signal at the chopper frequency to extract changes in the probe beam transmission or reflection. The temporal resolution in the experiment stems from the optical path length difference between the pump and the probe pulses. The complete ultrafast spectrum results from averaging repeated measurements of the photoinduced changes in the probe transmission or reflection over the entire range time delays between the pump and the probe.

The laser wavelength, i. e. the photon energy, used in an ultrafast pump-probe experiment determines the electronic transitions that the pump pulse excites and the probe pulse scans. The fluence defines as the pulse energy per unit area is related to the local heating and density of photogenerated quasiparticles by the absorbed pump pulse. The value of fluence must be large enough in order to induce measurable changes in the optical properties of a perturbed system. In other words, the signal to noise ratio must be larger than unity, which determines a lower limit on the required fluence in a particular pump-probe experiment. Lock-in detection employed in ultrafast pump-probe spectroscopy allows measuring relative changes in transmission or reflection as small as 10^{-5} - 10^{-7} by means of using a high repetition rate laser, high frequency modulation and highly sensitive avalanche photodiodes. Lock-in amplifier along with an optical chopper reduce the overall noise by

filtering out the noise not within the frequency pass band of the lock-in. High repetition rate lasers further enhance the signal to noise ratio of the measured signal by means of an increased counting statistics.

The interaction of a pulsed laser light with a sample can be described by the commonly applied two-temperature model. The two interacting subsystems in a material are electrons and phonons. The electrons in a material are internally in thermal equilibrium with the electron temperature T_e, while the thermal equilibrium of phonons is described by the phonon temperature T_p. As the external laser field couples only to the electrons in a material, the energy of laser light is initially deposited into the subsystem of electrons. In the case of the small electron temperature changes, the electron-phonon energy transfer can be approximated as a linear function of the temperature difference between the two subsystems. The time evolution of temperature is then described by the following set of coupled differential equations:

$$\begin{cases} C_e \frac{dT_e}{dt} = -g_{e-p}(T_e - T_p) + P(t), \\ C_p \frac{dT_p}{dt} = g_{e-p}(T_e - T_p), \end{cases} \tag{2.6}$$

where g_{e-p} is the electron-phonon coupling constant, $C_e(T)$ and $C_p(T)$ are in general temperature dependent specific heat capacitities of electrons and phonons, $P(t)$ describes energy deposition due to laser pumping.

The choice of laser pulse width is governed by temporal and spectral resolution. The temporal resolution needs to be small enough in order to resolve the shortest temporal feature and to reconstruct the relaxation process accurately. For instance, in the case when the measured ultrafast relaxation can be modelled as a double exponential decay with the time constants $\tau_1 < \tau_2$, the temporal resolution need to be less than τ_1 in order to accurately measure the relaxation dynamics. The double exponential decay models processes similar to the semiconductor thermalization and recombination dynamics after above band gap photoexcitation with a femtosecond pulse, where τ_1 and τ_2 represent the thermalization ($< 1\ ps$) and recombination ($> 1\ ps$) time constants, respectively. The time domain signal

for the case of instantaneous excitation, i. e. when the excitation process is much faster than the temporal resolution, can be written as:

$$g_0(t) = u(t)\left[A_1 \exp\left(-\frac{t}{\tau_1}\right) + A_2 \exp\left(-\frac{t}{\tau_2}\right)\right], \tag{2.7}$$

where $u(t)$ is a step function and A_1 and A_2 are the amplitudes of the two exponents.

As mentioned above, the laser pulse width must be short enough in order to resolve the shorter lifetime τ_1. The temporal profile of a typical laser pump and probe pulses is described by a Gaussian with a pulse width σ and a central frequency ν_0:

$$p(t) = B \exp\left(-\frac{t^2}{\sigma^2}\right) \sin(2\pi\nu_0 t) \tag{2.8}$$

In the equation for the double exponential decay signal it is assumed that the rise time is instantaneous. However, in practice the pump pulse width σ is finite and, hence, results in a finite rise time of an ultrafast pump-probe signal. This essentially corresponds to the case when the pump pulse energy is deposited to the system over the temporal profile $p(t)$, which causes a finite rise time of the actual response of the system. It is important to understand that in this case the finite rise time of a signal does not represent any property of the studied material, but stems from the experimental apparatus (see Figure 2.17). In this case, the actual measured ultrafast pump-probe signal is a convolution integral of the model relaxation dynamics $g_0(t)$ and the pump pulse temporal profile $p(t)$:

$$g_1(t) = \int_{-\infty}^{+\infty} g_0(x)p(x-t)dx \tag{2.9}$$

The finite pulse width of the probe beam also causes a modification of the detected pump induced dynamics signal. Each individual probe pulse measures the pump induced change in the optical properties of the studied material over the temporal profile of the probe pulse. Hence, the detected signal is a second convolution integral of the pump altered signal $g_1(t)$

and the probe pulse temporal profile $p(t)$:

$$g_2(t) = \int_{-\infty}^{+\infty} g_1(y) p_{probe}(y-t)dy = \int_{-\infty}^{+\infty} \left[\int_{-\infty}^{+\infty} g_0(x) p_{pump}(x-y)dx \right] p_{probe}(y-t)dy \tag{2.10}$$

$$g_2(t) = \int_{-\infty}^{+\infty} g_0(x) \left[\int_{-\infty}^{+\infty} p_{pump}(x-y) p_{probe}(y-t)dy \right] dx \tag{2.11}$$

Exchanging the order of integration in the above equation yields an autocorrelation integral $C(\tau)$ representing the temporal overlap between the pump and probe pulse profiles:

$$C(\tau) = \int_{-\infty}^{+\infty} p_{pump}(z) p_{probe}(z-\tau)dz = \int_{-\infty}^{+\infty} B^2 \exp\left(-\frac{z^2}{\sigma^2}\right) \exp\left(-\frac{(z-\tau)^2}{\sigma^2}\right) dz \tag{2.12}$$

$$C(\tau) = B^2 \exp\left(-\frac{\tau^2}{2\sigma^2}\right) = C_0 \exp\left(-\frac{\tau^2}{w^2}\right) \tag{2.13}$$

Hence, for the two Gaussian pulses the autocorrelation function is a Gaussian with a width $w = \sigma\sqrt{2}$ with σ being the temporal pulse width of the pump and probe pulses. Thus, given the model relaxation function $g_0(t)$ and the pump and probe autocorrelation function $C(\tau)$, the actual detected signal is found by:

$$g_2(t) = \int_{-\infty}^{+\infty} g_0(x) C(x-t)dx \tag{2.14}$$

$$g_2(t) = \int_{-\infty}^{+\infty} \left[A_1 \exp\left(-\frac{x}{\tau_1}\right) + A_2 \exp\left(-\frac{x}{\tau_2}\right) \right] C_0 \exp\left(-\frac{(x-(t-t_0))^2}{w^2}\right) dx \tag{2.15}$$

The integral above can be written in terms of the error function integral:

$$\begin{aligned} g_2(t) = {} & D_1 \exp\left(-\frac{t-t_0}{\tau_1}\right) \left[1 - erf\left(\frac{w}{2\tau_1} - \frac{t-t_0}{w}\right) \right] + \\ & + D_2 \exp\left(-\frac{t-t_0}{\tau_2}\right) \left[1 - erf\left(\frac{w}{2\tau_2} - \frac{t-t_0}{w}\right) \right] \end{aligned} \tag{2.16}$$

This function can be fitted to experimental ultrafast pump-probe data to find the relative amplitudes $D_1 = C_0 A_1$ and $D_2 = C_0 A_2$ as well as the time constants characterizing the fast

and slow relaxation components τ_1 and τ_2 for a given cross correlation width $w = \sigma\sqrt{2}$. It is clear from the above equations that processes with lifetimes shorter than the cross correlation width cannot be monitored in a pump-probe experiment.

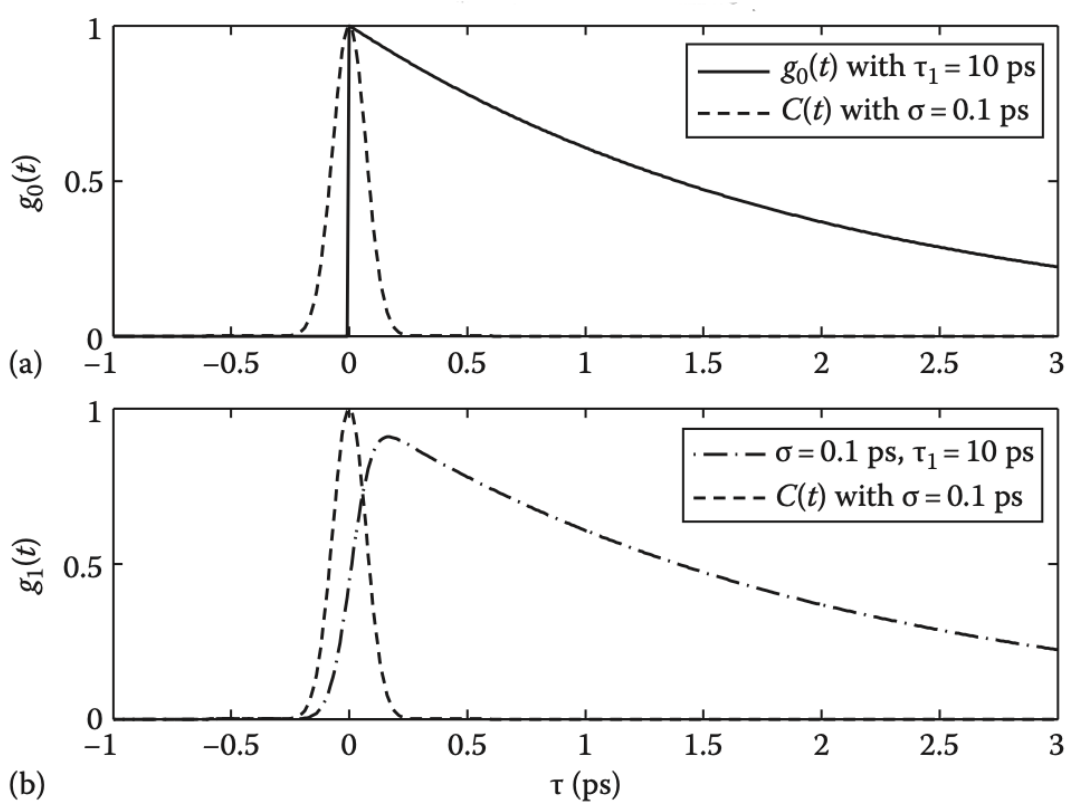

Figure 2.17: Pulse width limited system response in an ultrafast pump-probe experiment. a) The instantaneous response of the system for a delta function pump input. b) The finite rise time of the system response due to the finite pulse width. [15]

Chapter 3

Experimental data

3.1 Sample characterization and experimental configuration

Single layer CVD graphene on a copper foil was transferred onto a soda-lime glass substrate by means of a wet transfer method. The substrate was confirmed to be soda-lime glass with UV-VIS transmission and Raman measurements (see Figures 3.1 and 3.2). First, poly-methyl methacrylate (PMMA) was spun coated on top of the graphene/copper sample at 4500 rpm. Then, the sample was left in Iron Chloride ($FeCl_3$) for 24 hours to etch away copper. After the copper foil is etched, the PMMA/graphene layer was cleaned of the copper etchant residue by consequently dipping it in Deionized Water (DI) and then leaving it in DI for 24 hours. Next, the PMMA/graphene sample was mechanically transferred onto a soda-lime glass substrate. As the last step, we removed PMMA layer by dissolving it in acetone, which followed by an isopropanol (IPA) rinse. The quality and uniformity of the transferred graphene layer was confirmed by Raman spectroscopy using a Thermo Scientific DXR Raman Microscope. Figure 3.3 shows Raman spectrum averaged over ten different points on the sample, with positions of G and 2D peaks being $1591.6 \pm 1.5\ cm^{-1}$ and $2681 \pm 3\ cm^{-1}$, respectively. The type of Fermi level was determined from Figure 3.4 [19]. The red and blue solid lines in Figure 3.4 show the correlation between the G and 2D Raman peaks of graphene doped with various densities of holes and electrons, respectively, by an electrical method [20, 19]. The point on the graph corresponding to the positions of the G and 2D peaks of our graphene sample (1591 cm^{-1}, 2681 cm^{-1}) rests on the blue line in Figure 3.4. Hence, we infer the n-type of Fermi level for our sample. The shift of 11 cm^{-1} in the G peak position provides an estimate of the Fermi level (n-type) at 306 meV as seen from Figure 3.5 [21].

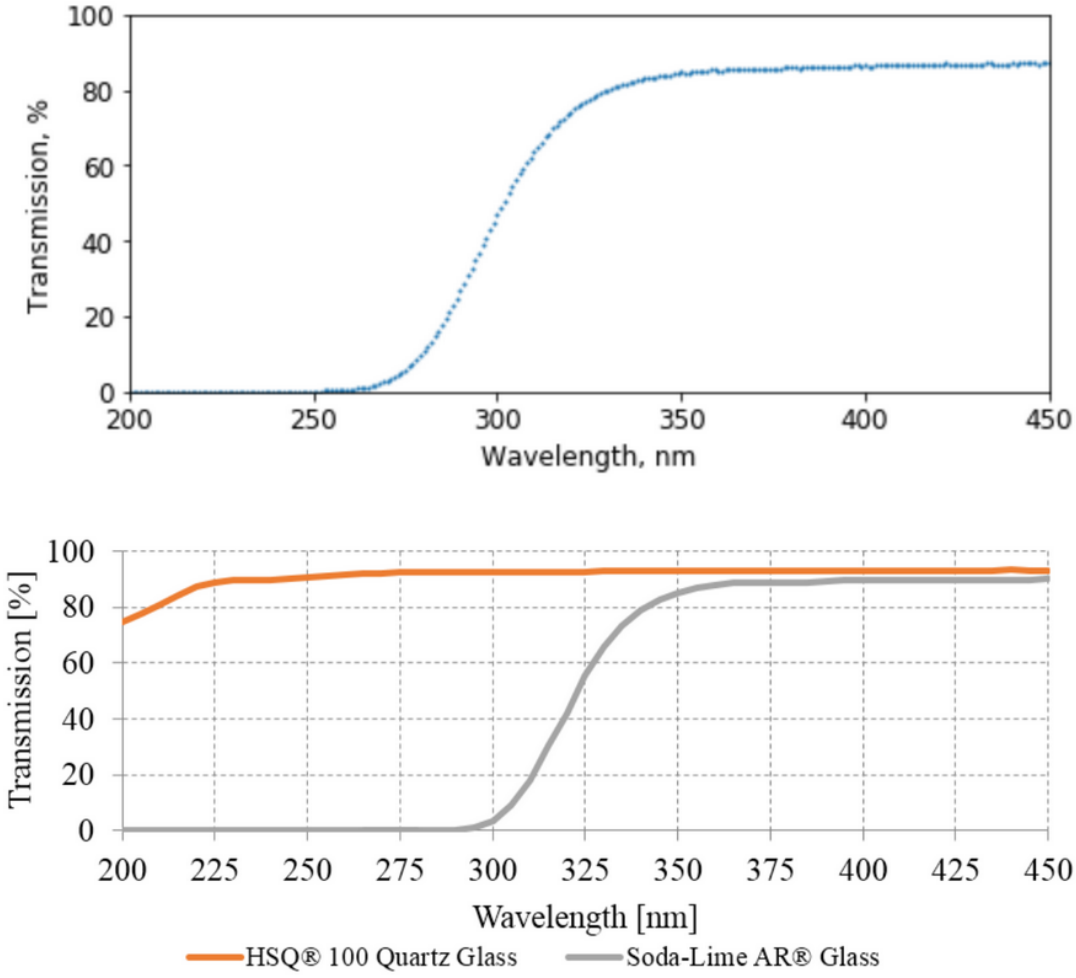

Figure 3.1: (Top) Transmission spectrum of our substrate with a thickness of 2mm. (Bottom) Transmission of HSQ 100 quartz glass (orange) and soda-lime glass (gray) with a thickness of 1 mm [16].

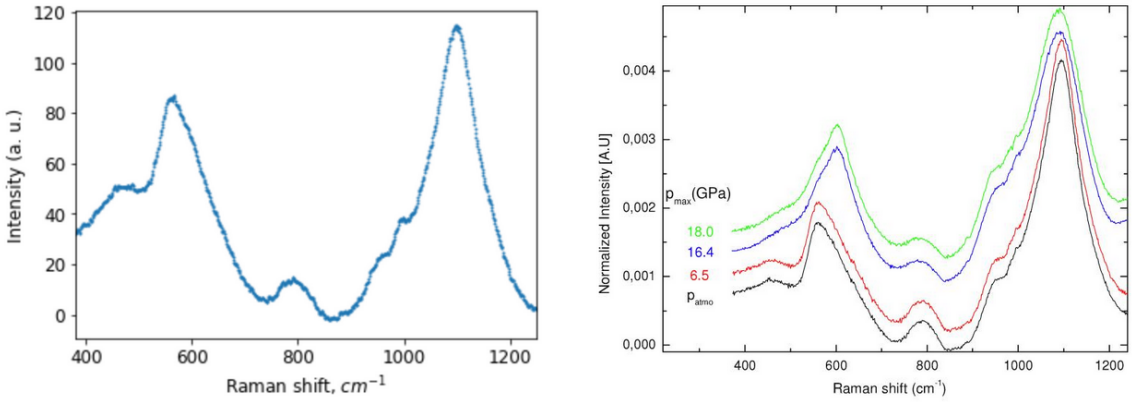

Figure 3.2: (Left) Raman spectrum of our substrate. (Right) Raman spectra of soda-lime glass under different pressures [17].

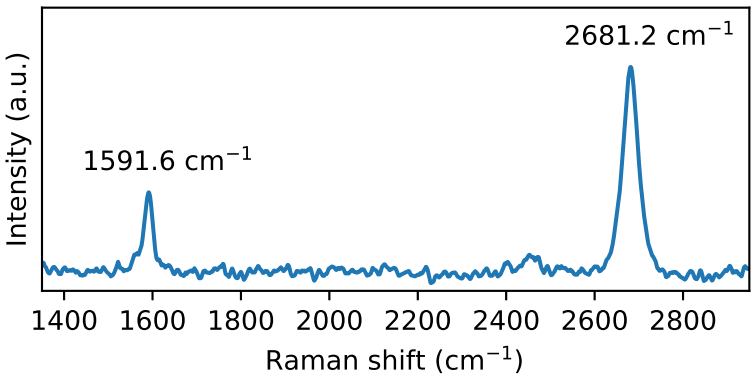

Figure 3.3: Raman spectrum of graphene on a soda-lime glass substrate taken with 532 nm CW laser. The detected G and 2D peaks are centered at 1591.6 ± 1.5 cm^{-1} and 2681 ± 3 cm^{-1} [18].

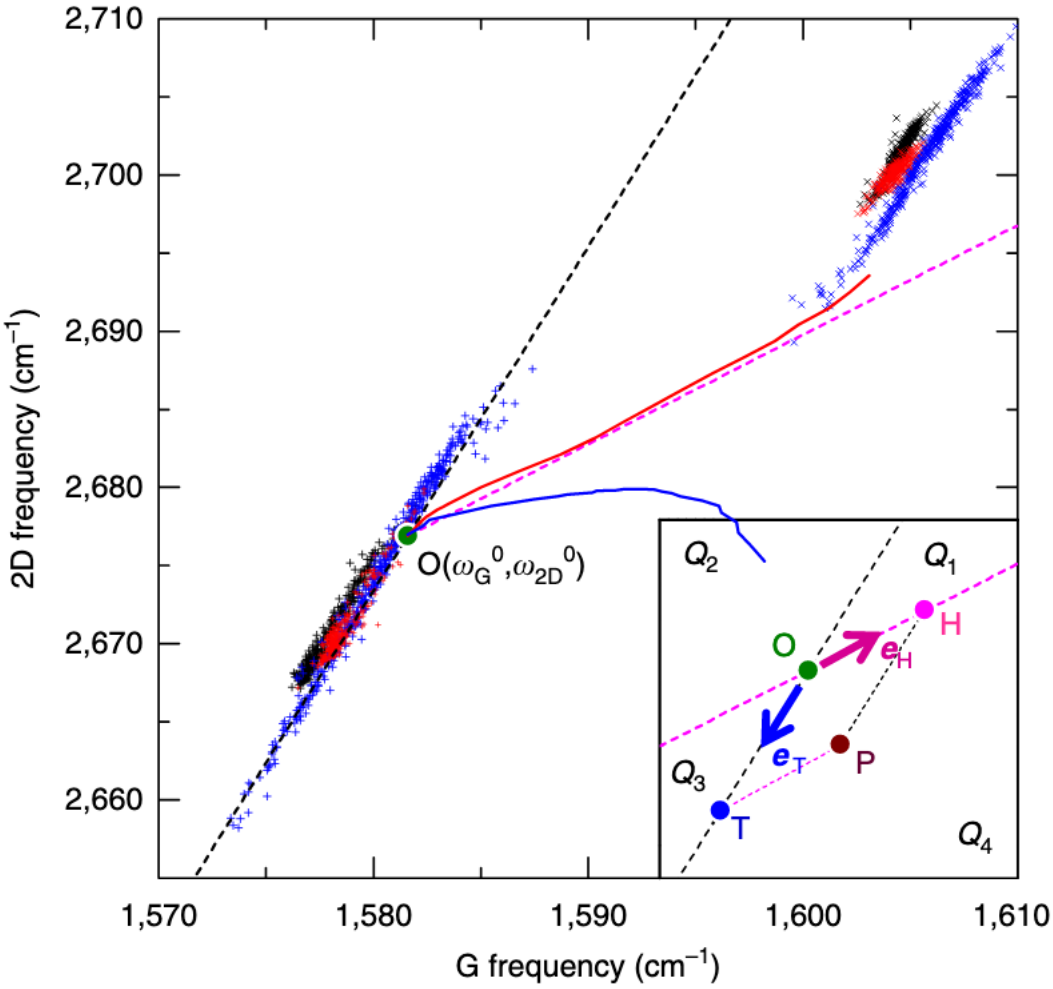

Figure 3.4: Correlation between the frequencies of the G and 2D Raman peaks of graphene [19]. The red and blue solid lines show the correlation between the G and 2D Raman peaks of graphene doped with various densities of holes and electrons, respectively, by an electrical method [20].

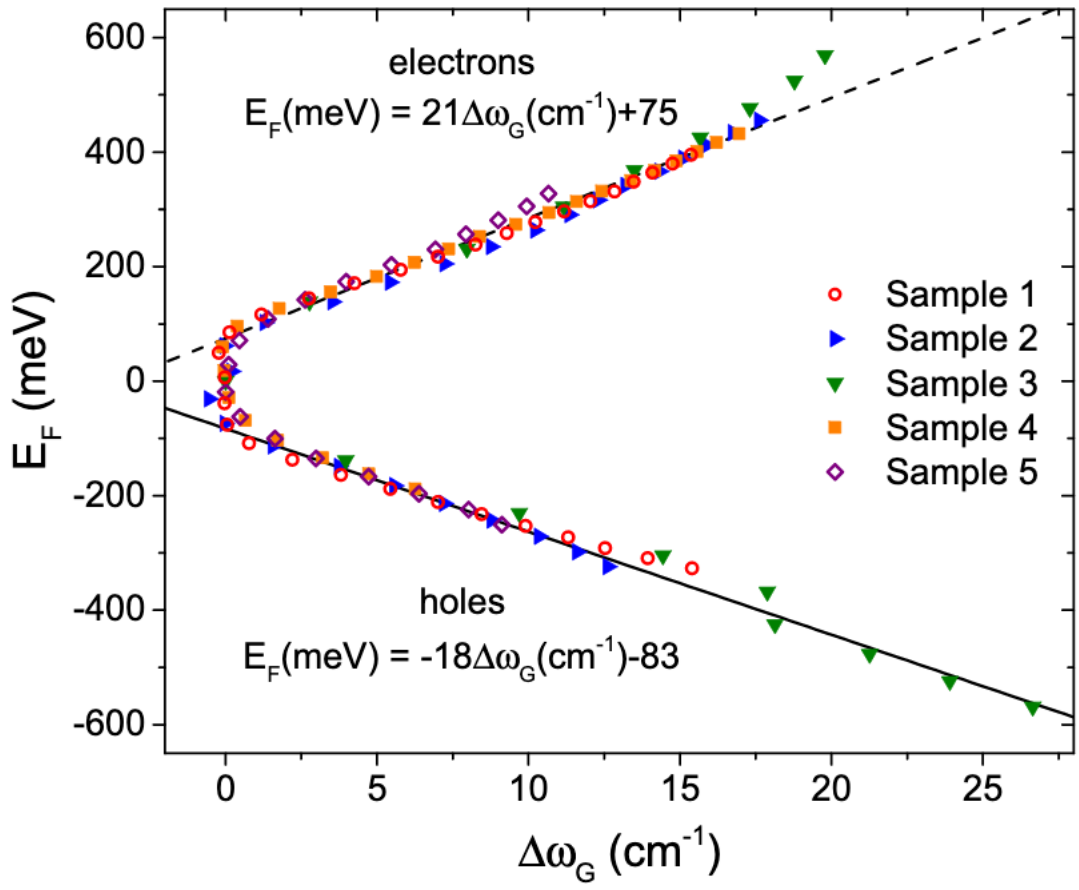

Figure 3.5: Fermi energy as a function of the relative frequency of the G peak [21].

Ultrafast pump-probe transmission measurements were carried out using a Ti:Sapphire oscillator producing 120 fs pulses at a 76 MHz repetition rate. Pump and probe wavelengths were initially both set to 800 nm (1.55 eV) and subsequently changed to 775 nm (1.60 eV), 825 nm (1.51 eV) and 850 nm (1.46 eV). Both beams were focused onto the specimen with spot diameters of 80 μm and 50 μm for pump and probe, respectively. The pump beam was chopped using a SR540 optical chopper operating at about 4 kHz. The differential transmission signal was detected using a Lock-In amplifier.

3.2 Pump-probe transmission data

Figures 3.6a, 3.7a, 3.8a and 3.9a show the pump fluence dependent DTD at 800 nm, 775 nm, 825 nm and 850 nm, respectively. After the initial positive spike in the differential transmission due to Pauli blocking of the interband transitions upon photoexcitation, the slow recovery differential transmission dynamics can be either positive or negative depending on the pump fluence. At high fluences (above 20 μJ/cm^2, 25 μJ/cm^2, 33 μJ/cm^2 and 39 μJ/cm^2 for 775 nm, 800 nm, 825 nm and 850 nm, respectively), the differential transmission is fully positive due to predominant contribution of interband transitions [70], while for lower fluences (below 20 μJ/cm^2, 25 μJ/cm^2, 33 μJ/cm^2 and 39 μJ/cm^2 for 775 nm, 800 nm, 825 nm and 850 nm, respectively) the differential transmission becomes negative past $\approx$0.5 ps due to greater contribution of intraband transitions [70]. At intermediate fluences (see data at the fluences of 20 μJ/cm^2 in Fig. 3.7a, 25 μJ/cm^2 in Fig. 3.6b, 33 μJ/cm^2 in Fig. 3.8a and 39 μJ/cm^2 in Fig. 3.9a for 775 nm, 800 nm, 825 nm and 850 nm, respectively), where a transition from intra- to interband dominated response occurs, much faster relaxation dynamics of DT is observed as compared to low and high fluences (indicated schematically by arrows in Figs. 3.6b, 3.7a, 3.8a and 3.9a).

3.3 Bi-exponential analysis of transmission relaxation curves

In order to characterize relaxation of the differential transmission, we fit a bi-exponential decay convoluted with Gaussian pump and probe pulses to our data using the following equation [15]:

$$g(t) = \int_{-\infty}^{+\infty} \left[A_1 \exp\left(-\frac{x}{\tau_1}\right) + A_2 \exp\left(-\frac{x}{\tau_2}\right) \right] C_0 \exp\left(-\frac{(x-(t-t_0))^2}{w^2}\right) dx \qquad (3.1)$$

$$\begin{aligned} g(t) =& D_1 \exp\left(-\frac{t-t_0}{\tau_1}\right) \left[1 - erf\left(\frac{w}{2\tau_1} - \frac{t-t_0}{w}\right)\right] + \\ &+ D_2 \exp\left(-\frac{t-t_0}{\tau_2}\right) \left[1 - erf\left(\frac{w}{2\tau_2} - \frac{t-t_0}{w}\right)\right], \end{aligned} \qquad (3.2)$$

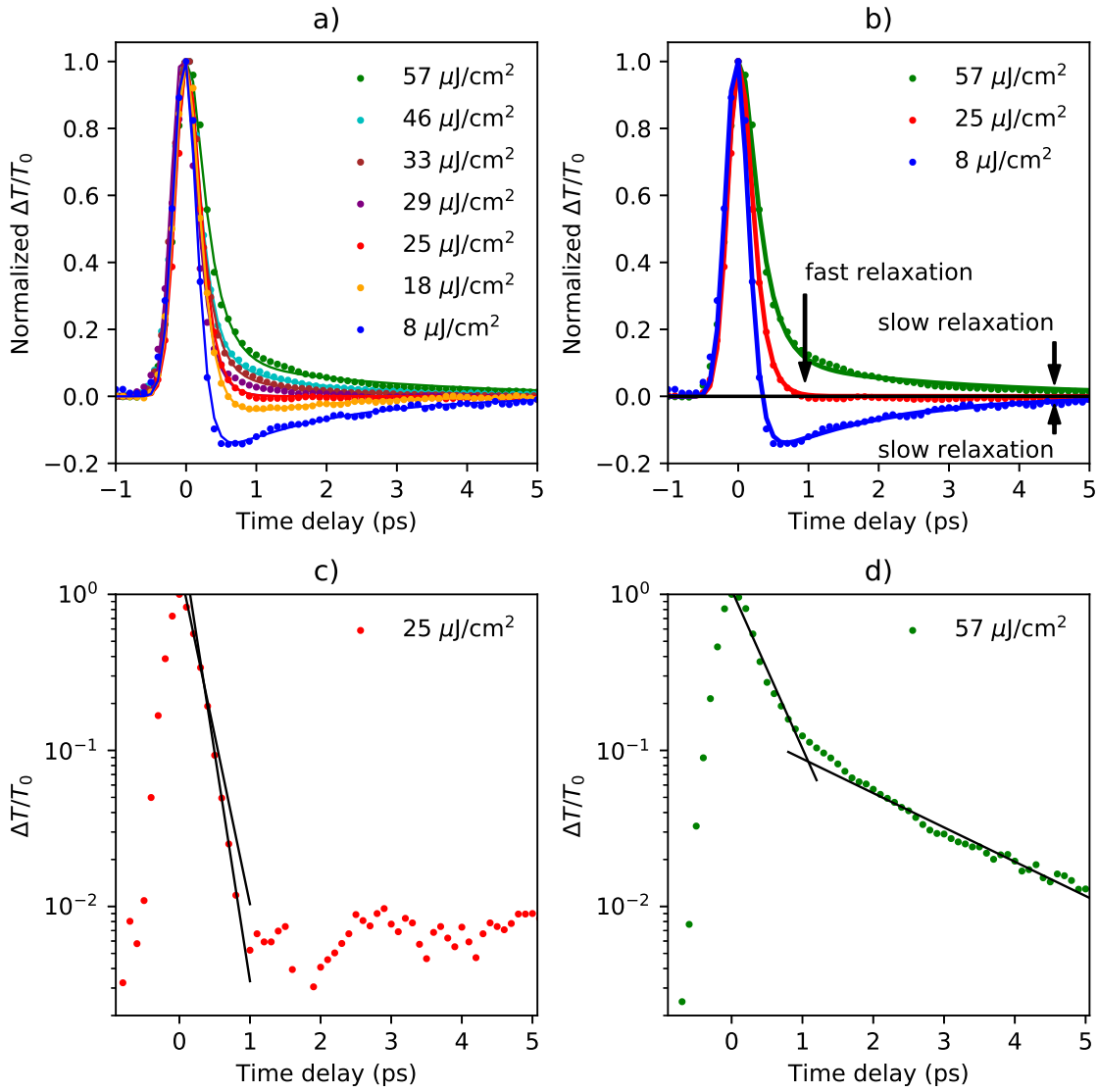

Figure 3.6: Pump-probe response of graphene on quartz at 800 nm using various pump fluences. The dots represent experimental data and the solid lines are the fits. a) Normalized pump-probe data. b) An order of magnitude faster differential transmission dynamics at a transition from intra- to interband dominated response. The relaxation time decreases from 5 ps to less than 1 ps. c) The differential transmission data at a pump fluence of 25 $\mu J/cm^2$ plotted on a log scale showing almost a single exponential decay. d) The differential transmission data at a pump fluence of 57 $\mu J/cm^2$ plotted on a log scale showing two distinct slopes implying a bi-exponential decay [18].

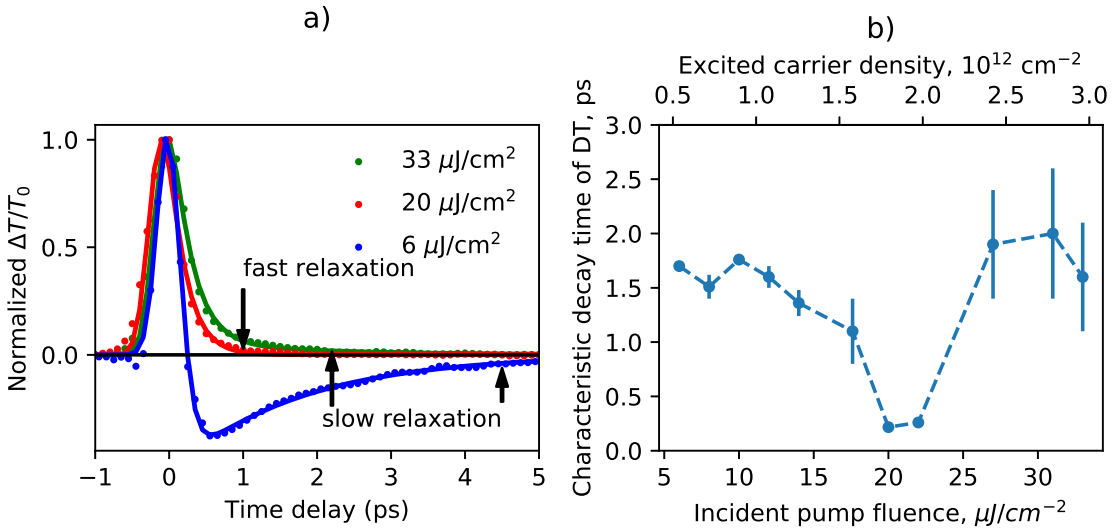

Figure 3.7: Normalized fluence dependent pump-probe data and corresponding characteristic relaxation times of DT at 775 nm. The dots represent experimental data and the solid lines represent the fits. The error bars represent s.d. of the fit [18].

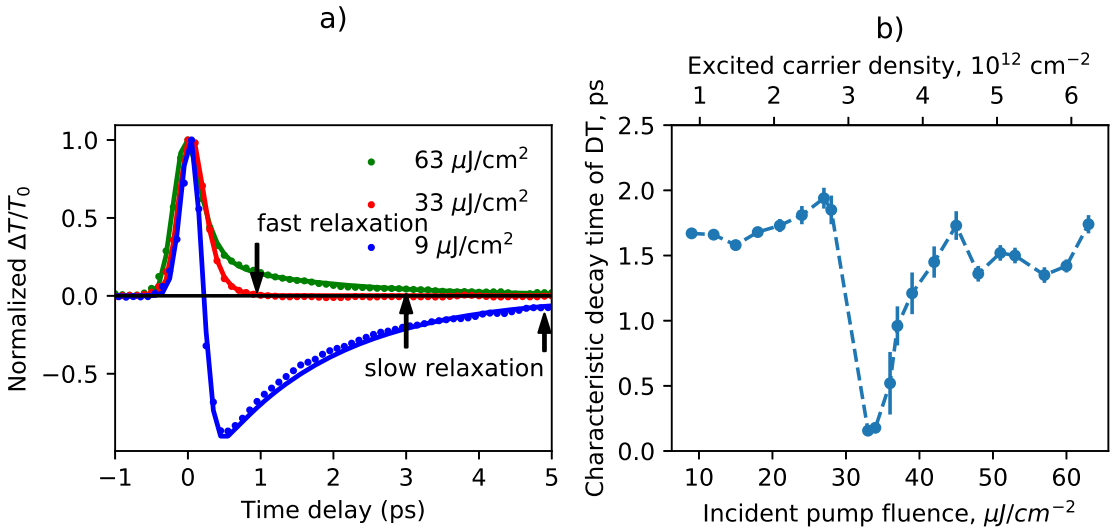

Figure 3.8: Normalized fluence dependent pump-probe data and corresponding characteristic relaxation times of DT at 825 nm. The dots represent experimental data and the solid lines represent the fits. The error bars represent s.d. of the fit [18].

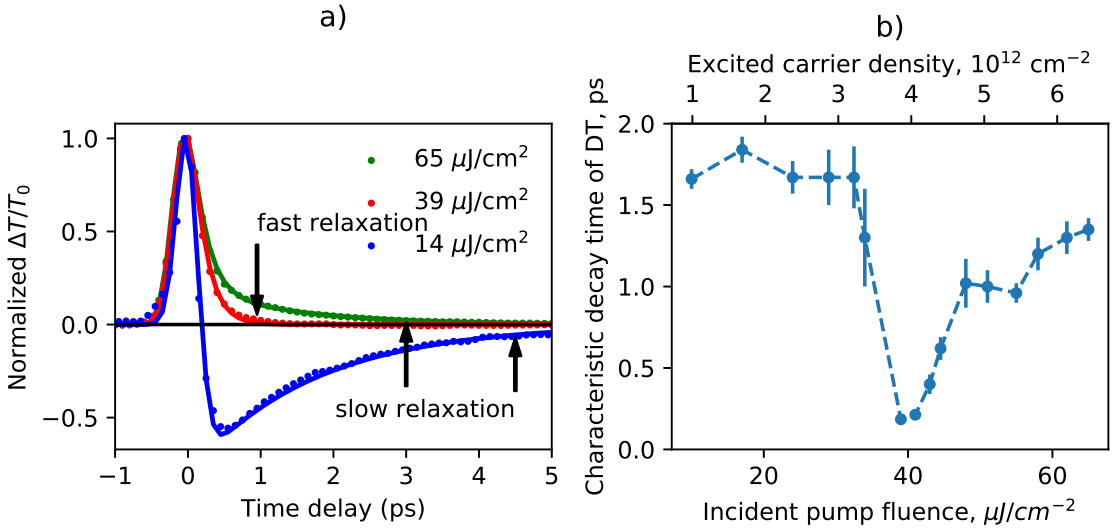

Figure 3.9: Normalized fluence dependent pump-probe data and corresponding characteristic relaxation times of DT at 850 nm. The dots represent experimental data and the solid lines represent the fits. The error bars represent s.d. of the fit [18].

where $D_1, D_2, t_0, \tau_1, \tau_2$ are the fitting parameters. $w = \sigma\sqrt{2}$ is the width of the autocorrelation function with σ being the width of the the Gaussian pump and probe pulses. The time constants τ_1 and τ_2 refer to fast and slow decay processes, respectively. Since our pulse width is 120 fs, we do not have enough temporal resolution to measure the time constant τ_1 accurately. Therefore, we report and focus only on the slow decay characterized by the time constant τ_2, which is sufficient for our needs because τ_2 largely characterizes the total relaxation times of DT. The fitting results using equation 3.2 are shown in Figures 3.7b, 3.10, 3.8b and 3.9b for 775 nm, 800 nm, 825 nm and 850 nm, respectively. The amplitude of the slower exponent corresponding to the relaxation time constant τ_2 changes sign from negative to positive when going from lower to higher fluences, which explains the instability of the biexponential fit at the intermediate pump fluences (see Table 3.11). As the pump fluences approach the intermediate values, at which the aforementioned transition occurs, the double exponential character of the response vanishes and instead becomes a single exponential due to the fact that the amplitude of the slower component is essentially zero at the intermediate fluences. As a result, the characteristic relaxation time of the differ-

ential transmission drops by an order of magnitude at the intermediate fluences. The onset of the single exponential behavior at the intermediate fluences is seen more clearly on the log scale in Fig. 3.6c,d. In the next chapter we show that an order of magnitude faster DTD observed at the intermediate fluences is explained well by a model that accounts for the contributions of both intra- and interband transitions to DTD in graphene, which depend on the temperature of the excited electrons.

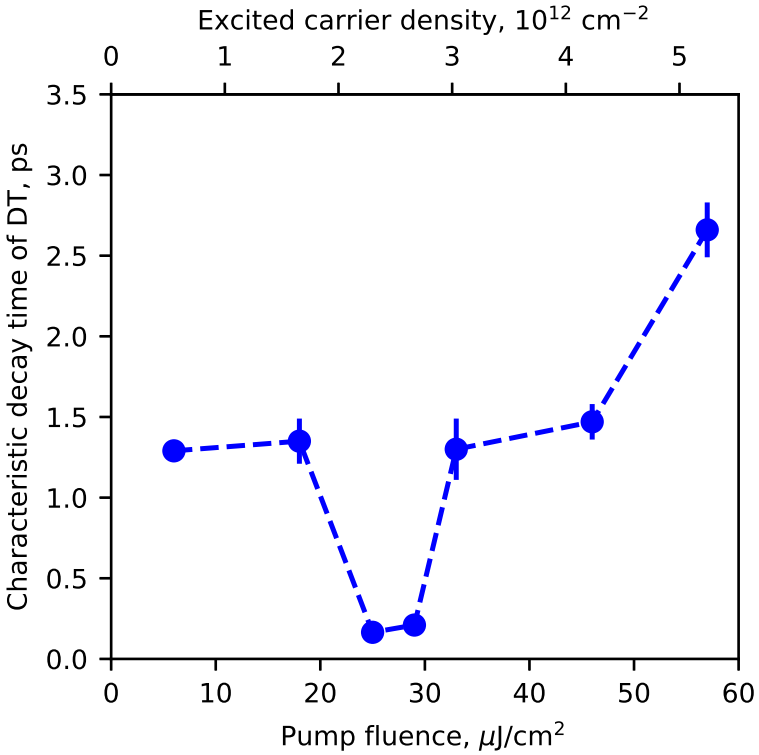

Figure 3.10: Characteristic relaxation times of DT at 800 nm. The error bars represent s. d. of the fit [18].

Fitting parameter	6 μJ/cm^2	18 μJ/cm2	21 μJ/cm2	25 μJ/cm2	33 μJ/cm2	46 μJ/cm2
τ_1, ps	0.039 +/- 0.003	0.170 +/- 0.004	0.165 +/- 4249	0.206 +/- 0.004	0.191 +/- 0.006	0.186 +/- 0.005
τ_2, ps	1.28 +/- 0.06	1.35 +/- 0.14	0.165 +/- 733	1.4 +/- 1.8	1.30 +/- 0.19	1.47 +/- 0.11
D_1	310 +/- 280	0.550 +/- 0.017	0.125 +/- 330326	0.831 +/- 0.015	1.28 +/- 0.04	1.21 +/- 0.04
D_2	0.0195 +/- 0.0007	-0.014 +/- 0.002	0.727 +/- 330326	0.002 +/- 0.003	0.035 +/- 0.007	0.049 +/- 0.005
t_0, ps	0.013 +/- 0.003	-0.109 +- 0.002	-0.090 +/- 0.004	-0.121 +/- 0.002	-0.194 +/- 0.002	-0.189 +/- 0.002
τ			0.165 +/- 0.003	0.210 +/- 0.002		
D			0.85 +/- 0.02	0.82 +/- 0.01		
t_0			-0.090 +/- 0.002	-0.121 +/- 0.001		

Figure 3.11: Table with the best-fit parameters of the bi-exponential fit to 800 nm data.

Chapter 4

Data analysis and modelling

4.1 Model for transmission and optical conductivity

Applying the optical boundary conditions at the air/graphene/substrate interfaces, the optical transmission $t(\omega)$ through the single layer graphene on a substrate normalized to the transmission through the substrate can be expressed as [143, 56]

$$t(\omega) = \frac{1}{|1+\sigma(\omega)Z_0/(1+n_s)|^2}, \tag{4.1}$$

where $\sigma(\omega)$ is the complex optical conductivity of graphene, Z_0 is the vacuum impedance and n_s is the refraction index of the substrate. Since the absolute value of the second term in the denominator of equation 4.1 is much less than unity,

$$|\sigma(\omega)|Z_0/(1+n_s) \ll 1, \tag{4.2}$$

contribution of the imaginary part of the optical conductivity is negligible. Hence, the equation for transmission of the sample becomes

$$t(\omega) = \frac{1}{(1+Re[\sigma(\omega)]Z_0/(1+n_s))^2}, \tag{4.3}$$

The further simplification of equation 4.3 may be achieved upon Taylor expansion. Keeping the terms up to the first order, transmission is approximated as follows

$$t(\omega) \approx 1 - 2Re[\sigma(\omega)]Z_0/(1+n_s) \tag{4.4}$$

The expression for $\frac{\Delta t}{t_0}$ then becomes:

$$\frac{\Delta t}{t_0} = \frac{-\frac{2Z_0}{1+n_s}\Delta Re\sigma}{1-\frac{2Z_0}{1+n_s}Re\sigma_0} \tag{4.5}$$

The optical conductivity of single layer graphene is given by[144]

$$\begin{aligned}\frac{\mathrm{Re}\left(\sigma\left(\omega\right)\right)}{\sigma_Q} = \frac{4k_BT}{\pi\hbar}\left[\ln\left(1+e^{E_F^e/k_BT}\right)+\ln\left(1+e^{E_F^h/k_BT}\right)\right]\frac{\tau}{\omega^2\tau^2+1}+ \\ \frac{1}{2}\left[\tanh\left(\frac{\hbar\omega-2E_F^e}{4k_BT}\right)+\tanh\left(\frac{\hbar\omega-2E_F^h}{4k_BT}\right)\right],\end{aligned} \tag{4.6}$$

where $\sigma_Q = e^2/4\hbar$ is the universal quantum conductivity, k_B is Boltzmann constant, T is carrier temperature, $E_F^e(E_F^h)$ is the electron (hole) Fermi level, τ is the momentum scattering time. The first term in equation 4.6 describes a Drude-like intraband contribution to optical conductivity whereas the second term arises from interband transitions. The measured differential transmission is proportional to $-\Delta\left[\mathrm{Re}\left(\sigma\left(\omega\right)\right)/\sigma_Q\right]$ according to equation 4.5. Considering high n-type doping ($E_F^e >> 2k_BT$) and neglecting the contribution from minority carriers (holes), the optical conductivity can be written as

$$\frac{Re\left(\sigma\left(\omega\right)\right)}{\sigma_Q} = \frac{4E_F^e}{\pi\hbar}\frac{\tau}{\omega^2\tau^2+1}+\frac{1}{2}\tanh\left(\frac{\hbar\omega-2E_F^e}{4k_BT}\right). \tag{4.7}$$

The Fermi level, E_F^e, and temperature, T, of electrons in the equation 4.7 are, in general, time dependent quantities.

4.2 The electron temperature

The dynamics of the electron temperature is approximated to be governed by the following system of first order linear differential equations corresponding to the two temperature model, where the electrons and strongly coupled optical phonons are described by temperatures T and T_{op}, respectively. The initial electron cooling occurs through the emission of

optical phonons followed by anharmonic decay into acoustic modes.

$$\begin{cases} \frac{dT}{dt} = \alpha(T_{op} - T), & T(0) = T_1, \\ \frac{dT_{op}}{dt} = \beta(T - T_{op}) + \gamma(T_0 - T_{op}), & T_{op}(0) = T_0, \\ \frac{dT_{ac}}{dt} = 0, & T_{ac}(0) = T_0, \end{cases} \tag{4.8}$$

where T, T_{op} and T_{ac} are the electron, optical and acoustic phonon temperatures, respectively, $\alpha = G_{el,op}/C_{el} > 0$, $\beta = G_{el,op}/C_{op} > 0$, $\gamma = G_{op,ac}/C_{op} > 0$ with G and C denoting coupling constants and heat capacities of electrons and phonons, and $\alpha \gg \beta, \gamma$. Ignoring temperature dependence of the coefficients α, β and γ, the given system of differential equations can be solved analytically. As derived in Appendix B, the analytical solution is given by a double exponential function with the time constants τ_1 and τ_2 characterizing the faster and the slower relaxation components, respectively:

$$T = \frac{T_1 - T_0}{2}[(1+k)e^{-\frac{t}{\tau_1}} + (1-k)e^{-\frac{t}{\tau_2}}] + T_0, \tag{4.9}$$

$$\tau_1 = \frac{2}{(\alpha+\beta+\gamma) + \sqrt{(\alpha+\beta-\gamma)^2 + 4\beta\gamma}} \tag{4.10}$$

$$\tau_2 = \frac{2}{(\alpha+\beta+\gamma) - \sqrt{(\alpha+\beta-\gamma)^2 + 4\beta\gamma}} \tag{4.11}$$

$$\tau_1 < \tau_2 \tag{4.12}$$

$$0 < k = \frac{\alpha-\beta-\gamma}{\sqrt{(\alpha-\beta-\gamma)^2 + 4\alpha\beta}} < 1 \tag{4.13}$$

Apparently, there is some misunderstanding in literature, as it seems that some papers [58] use a double exponential electron temperature referencing papers showing a bi-exponential decay of the differential transmission [57, 64, 47, 66, 61]. We have shown that the double exponential electron temperature is premised on the temperature independence of the coefficients in the two temperature model. Since in our case $\alpha \gg \beta, \gamma$, the expressions for τ_1 and τ_2 can assume much simpler form. Factoring out $(\alpha+\beta-\gamma)^2$ from the square root in

the expressions for τ_1 and τ_2 and doing Taylor expansion on the square root, to first order we get

$$\tau_1 \approx \frac{1}{\alpha} \tag{4.14}$$

$$\tau_2 \approx \frac{1}{\gamma} \tag{4.15}$$

Thus, equations 4.14 and 4.15 imply that τ_1 characterizes the electron-phonon thermalization and τ_2 characterizes the hot optical phonon relaxation. Finally, the electron temperature as a function of time can be written as

$$T(t) = \frac{T_1 - T_0}{2}[(1+k)e^{-\frac{t}{\tau_{e-ph}}} + (1-k)e^{-\frac{t}{\tau_{op}}}] + T_0, \tag{4.16}$$

where $k = \frac{\alpha-\beta-\gamma}{\sqrt{(\alpha-\beta-\gamma)^2+4\alpha\beta}}$, $\tau_{e-ph} = \frac{1}{\alpha}$ and $\tau_{op} = \frac{1}{\gamma}$.

4.3 Implementation and results

The initial electron temperature, T_1, and Fermi level, E_F^e are estimated from energy conservation [68, 144]:

$$U_e(T_0, N) + \Delta Q = U_e(T_1, N+n) + U_h(T_1, p), \tag{4.17}$$

where

$$U_{e,h} = \frac{4k_B^3 T^3}{\pi v^2 \hbar^2} F_2\left(\frac{E_F^{e,h}}{k_B T}\right), \tag{4.18}$$

$$n, p = \frac{2k_B^2 T^2}{\pi v^2 \hbar^2} F_1\left(\frac{E_F^{e,h}}{k_B T}\right). \tag{4.19}$$

F_1 and F_2 are the first- and second-order Fermi integrals, respectively. $v = 10^6$ m/s is the Fermi velocity in graphene, N is the electron concentration at equilibrium. The time dynamics of the Fermi level, E_F^e is taken into account by solving equation 4.19 with carrier densities recombining exponentially, $n = N + n_0 e^{-t/\tau_R}$. The effective recombination time

$\tau_R = 1.3$ ps [68] was fixed for all fits. The results of the fitting procedures are shown in Figures 4.3a-f below. In all following Figures 4.3a-f the normalized differential transmission $\frac{\Delta T}{T_0}$ is plotted on the vertical axis and time delay Δt in picoseconds on the horizontal axis. The red circles represent experimental data. The fitting curves are in blue.

Figure 4.2b shows the pump fluence dependence of the relaxation time constant τ_{op}. Clearly, τ_{op} monotonically increases with increasing pump fluence and does not drop abruptly in the vicinity of the critical pump fluence. Hence, we conclude that such fast relaxation of the differential transmission is not due to a change in the relaxation mechanism, but due to inter- and intraband transitions contributing almost equally with opposite signs to the optical conductivity of graphene in the vicinity of the threshold pump fluence. The monotonic changes in τ_{op} as a function of pump fluence occur as a result of ignoring the temperature dependence of the electron-phonon coupling constant and the electron and phonon heat capacities. While microscopic theories describing ultrafast dynamics in graphene without invoking any fitting parameters have been developed [70, 145], the present approach is sufficient to demonstrate that an order of magnitude faster DTD at the intermediate pump fluences is well described by the model applied here accounting for intra- and interband transitions. Furthermore, an order of magnitude difference between the characteristic relaxation time of DT at the threshold pump fluences τ_1 and the characteristic relaxation time of the electron temperature τ_{op} indicates significant changes in the optical properties without altering the electron and phonon relaxation mechanisms.

Figure 4.1 shows the dependence of the threshold pump fluence on the wavelength as measured in our experiments. At the threshold pump fluence, a perfect balance between intra- and interband transitions leads to an order of magnitude faster DT relaxation. Beyond this fluence interband transitions dominate the signal. As seen from Figure 4.1, the threshold pump fluence as well as the corresponding excited carrier density are greater for lower probe energies. This behavior can be qualitatively understood based on Equation 4.7 describing the contributions of intra- and interband transitions to the optical conductivity

of graphene. The first Drude-like intraband term increases with decreasing probe energies. In other words, intraband absorption is more significant at lower probe energies. The only way to make the interband term have greater contribution is to reach higher electron temperatures so that the changes in the optical conductivity due to that interband term become greater. Hence, one needs to excite more electrons in order to reach higher temperatures and, consequently, overcome intraband absorption.

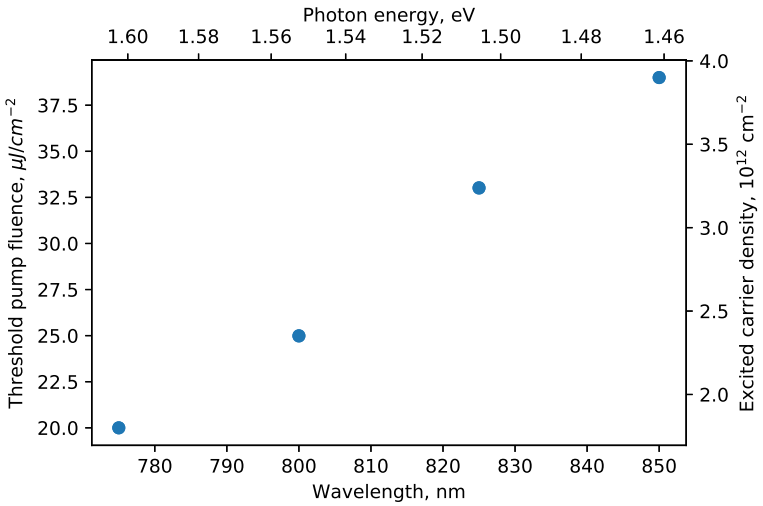

Figure 4.1: Threshold pump fluence versus wavelength [18].

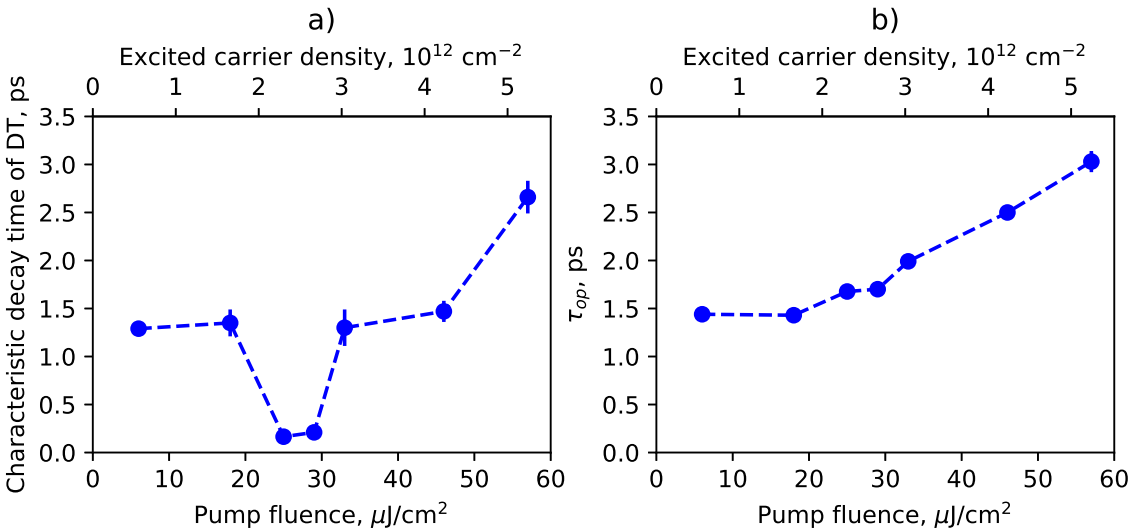

Figure 4.2: a) Characteristic relaxation times of DT at 800 nm obtained from the bi-exponential fit. At the pump fluences of 25 μJ/cm^2 and 29 μJ/cm^2 the bi-exponential fit parameters have huge uncertainties because the amplitude of τ_2 exponent is close to zero. Hence, the differential transmission dynamics is essentially characterized by a single exponent with time constant τ_1 at intermediate fluences of 25 μJ/cm^2 and 29 μJ/cm^2. As a result, an order of magnitude faster differential transmission relaxation times are observed. b) The phenomenological optical phonon relaxation time constant characterizing the relaxation of the electron temperature obtained by fitting the model accounting for inter- and intraband transitions to the DT data at 800 nm. The error-bars arise from the fitting procedure [18].

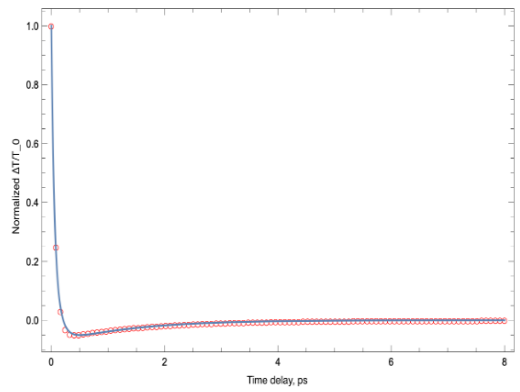

(a) 6 $\mu J/cm^2$

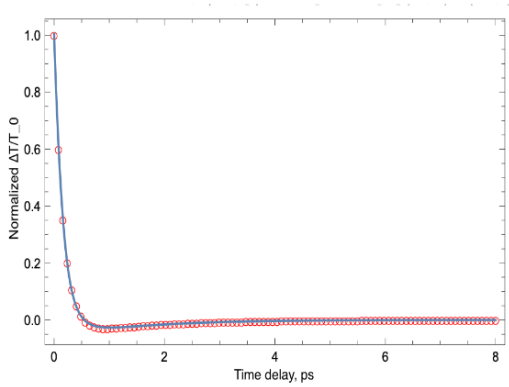

(b) 18 $\mu J/cm^2$

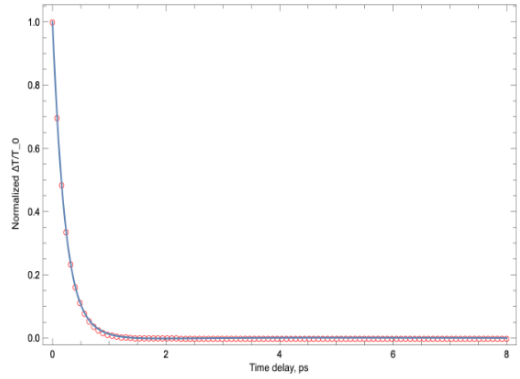

(c) 21 $\mu J/cm^2$

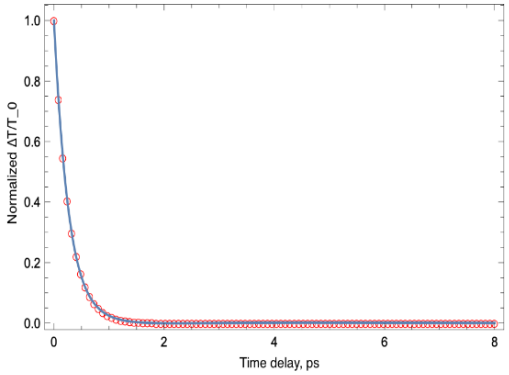

(d) 25 $\mu J/cm^2$

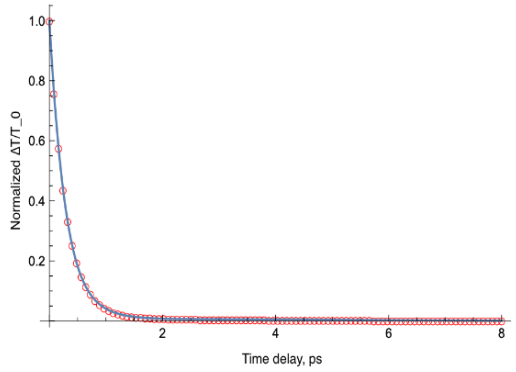

(e) 33 $\mu J/cm^2$

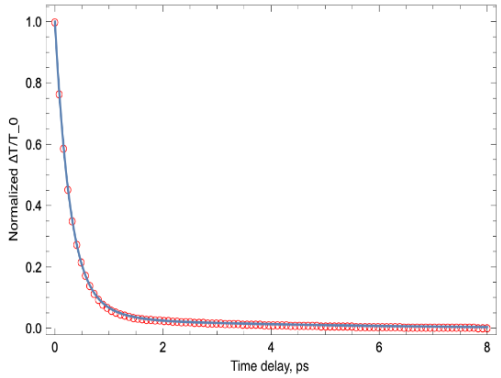

(f) 46 $\mu J/cm^2$

Figure 4.3: The experimental pump-probe differential transmission data at 800 nm(red circles) and the fitting curves (blue) at different pump fluences based on the model for the optical conductivity and the electron temperature.

Chapter 5

Ultrafast relaxation dynamics of graphene on patterned quartz

5.1 Introduction

The use of graphene in numerous applications frequently involves placing it on a substrate. The intrinsic properties of graphene are very dependent on the surrounding environment. Consequently, a substrate can significantly influence equilibrium and non-equilibrium dynamics in graphene. The effect of substrate on carrier relaxation mechanisms has been already explored in many studies [48, 49, 50, 51, 146, 62, 39]. In the study conducted by Hale *et al.* [146] relaxation dynamics was reported to be faster in suspended than supported graphene, whereas Gao *et al.* [62] found faster relaxation dynamics for supported graphene on a substrate. In the study by Wang *et al.* [39] relaxation dynamics was found to be independent of the substrate or graphene growth method. It is also known that carriers in graphene can lose their energy to coupled surface optical phonons of polar substrates through long range Fröhlich interactions [48, 49, 50, 51].

The project presented in this chapter is premised on the fact that it is generally understood that the ultrafast carrier relaxation dynamics is different for suspended and supported graphene. If single layer graphene is transferred onto a patterned substrate, i. e. a substrate with a certain percentage of holes, its ultrafast carrier dynamics should be modified. Thus, by varying relative percentage of suspended to supported graphene it should be possible to tune the ultrafast carrier relaxation dynamics in graphene. In the next section the experimental results as obtained from pump-probe experiments on single layer graphene transferred onto a patterned quartz substrate with hole densities of 16%, 33% and 50% are presented.

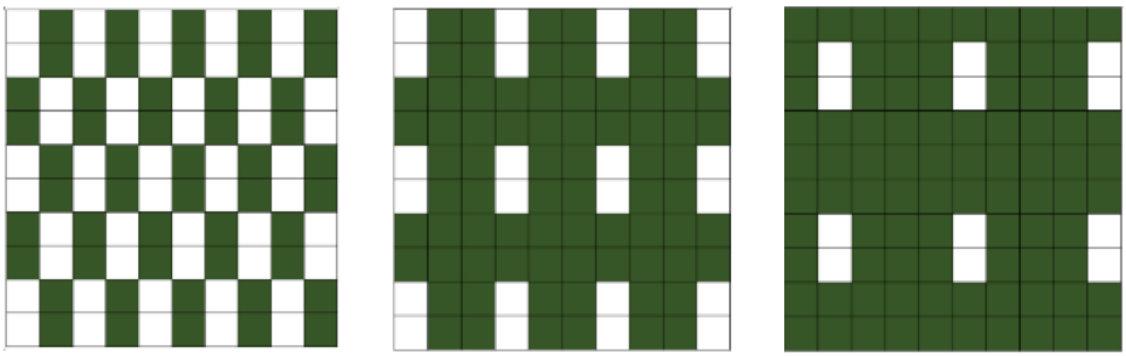

Figure 5.1: Schematic representation of the quartz substrate. The white regions represent suspended portions and the green regions represent supported portions of graphene. Each pattern is 400 by 400 micrometers. Hole size is 1 by 2 micrometers. The same graphene sheet covers all three patterns. From left to right the hole densities are 50%, 33% and 16%.

5.2 Experimental results and conclusions

Single layer CVD graphene grown on a copper foil was transferred onto a quartz substrate with a wet transfer method (see section 3.1 for details). The substrate had three periodic patterns of holes with densities of 16%, 33% and 50%. The hole size was one by two micrometers. The size of each pattern was 400 by 400 micrometers. The same graphene sheet covered all three pattern simultaneously. The sample configuration is shown schematically on Figure 5.1. Raman spectroscopy confirmed single layer graphene on all patterns as illustrated on Figure 5.2. The dependence of G and 2D peak positions on the percentage of suspended graphene is given in Figure 5.3.

Ultrafast pump-probe measurements were conducted using a Ti:Sapphire oscillator producing 120 fs at a 76 MHz repetition rate. Pump and probe wavelengths were both set to 800 nm (1.55 eV). Pump and probe spot diameters were 80 μm and 50 μm, respectively. The pump beam was chopped using a SR540 optical chopper operating at about 4 kHz. The differential transmission signal was detected using a Lock-In amplifier. The pump-probe data were taken at a few different spots for each sample. In order to characterize the ultrafast relaxation dynamics, we fitted a bi-exponential decay convoluted with Gaussian pump and probe pulses to our data using equation 3.2, in which $D_1, D_2, t_0, \tau_1, \tau_2$ are the fitting

parameters. The key fitting parameter characterizing the ultrafast differential transmission relaxation dynamics is τ_2. The values of τ_2 obtained from the bi-exponential fit for each individual spot on every pattern are show on Figure 5.5. The average values of τ_2 along with the standard deviation for each pattern are shown on Figure 5.4. As seen from Figure 5.4, the average values of τ_2 do not depend on the percentage of suspended graphene. The variations of τ_2 obtained from experiments are within the standard deviation. Thus, we conclude that patterning the substrate does not significantly affect the ultrafast relaxation dynamics in graphene. Speaking in more rigorous terms, the anticipated effect of a patterned substrate is overridden by non-uniformity of the sample, i. e. the statistical variations of τ_2 due to the non-uniformity are much larger than due to the effect of the patterned substrate. By examining Figure 5.4 we finally conclude that any variations of τ_2 due to the effect of a patterned substrate must be less than 0.2 ps.

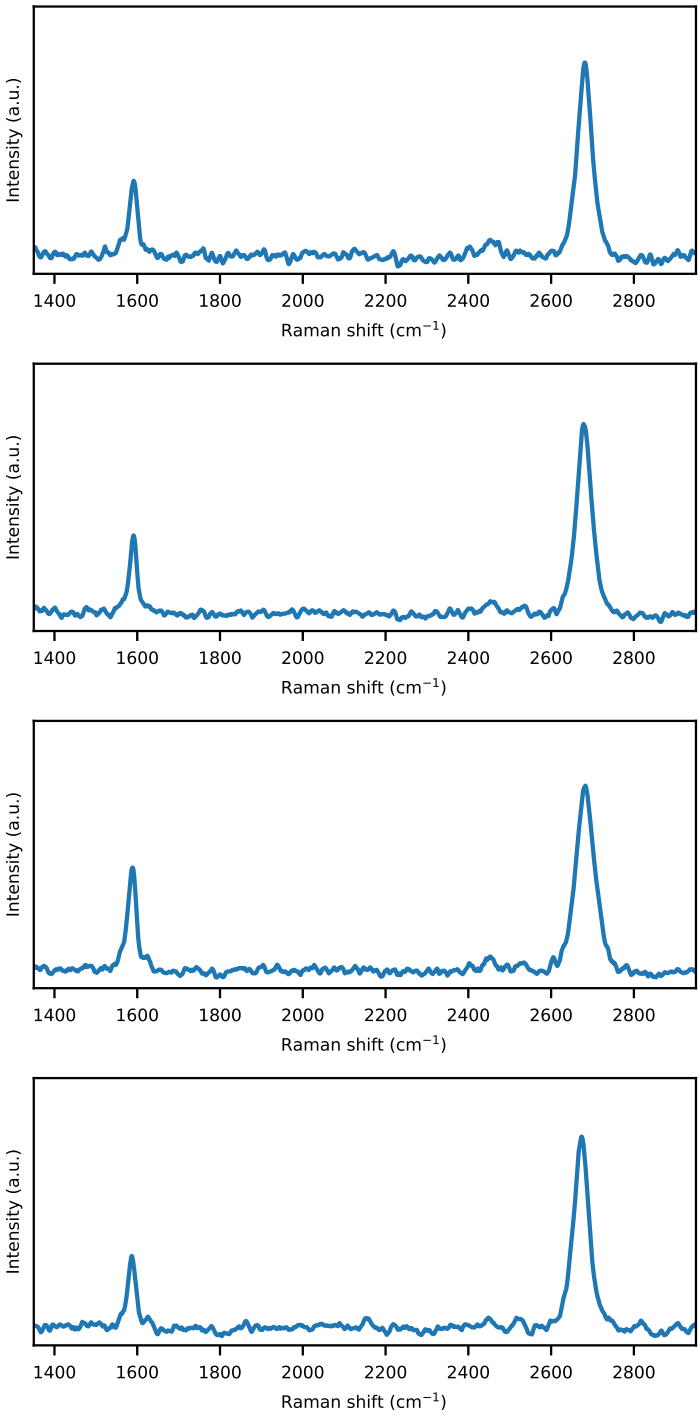

Figure 5.2: Raman spectra of graphene on the patterns with 0% (top), 16%, 33% and 50% (bottom) suspended graphene.

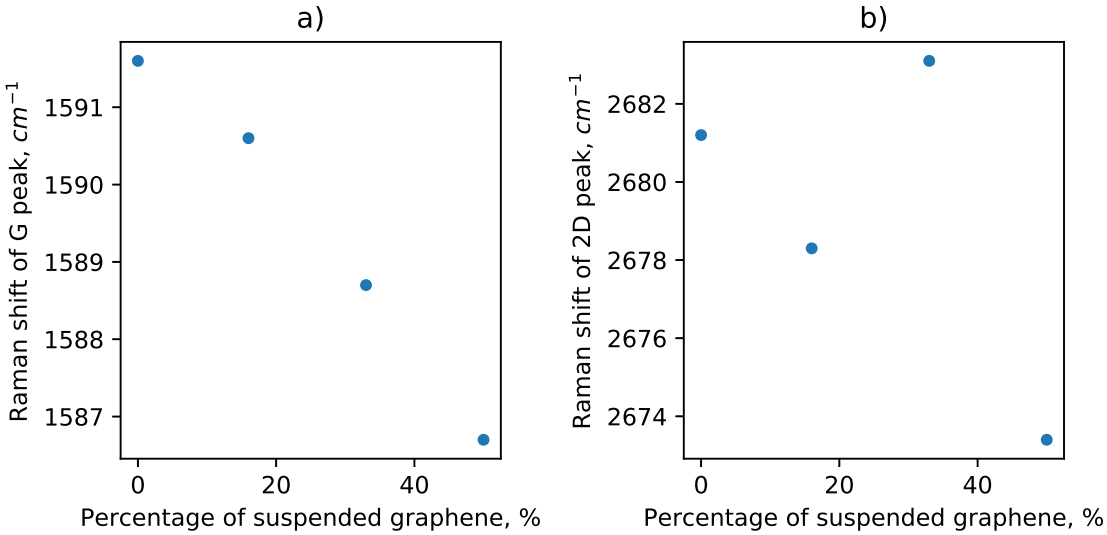

Figure 5.3: a) Positions of the G (a) and 2D (b) peaks as a function of the percentage of suspended graphene.

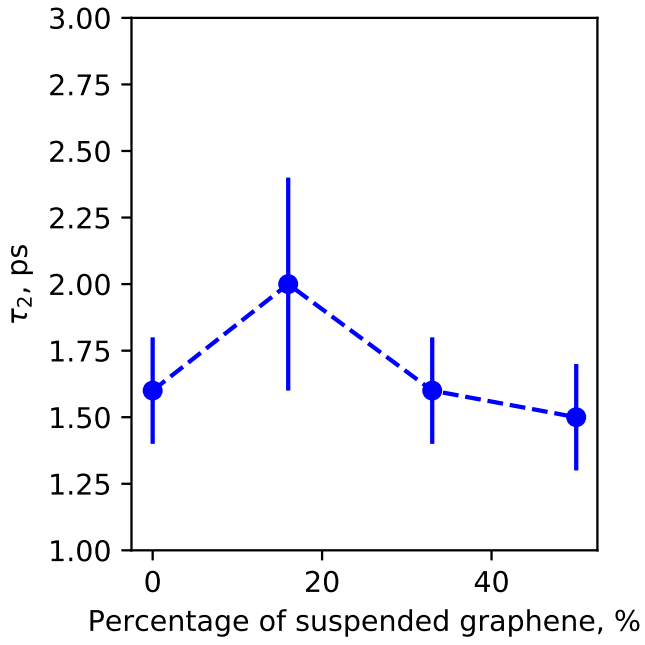

Figure 5.4: The average value of τ_2 as a function of the percentage of suspended graphene.

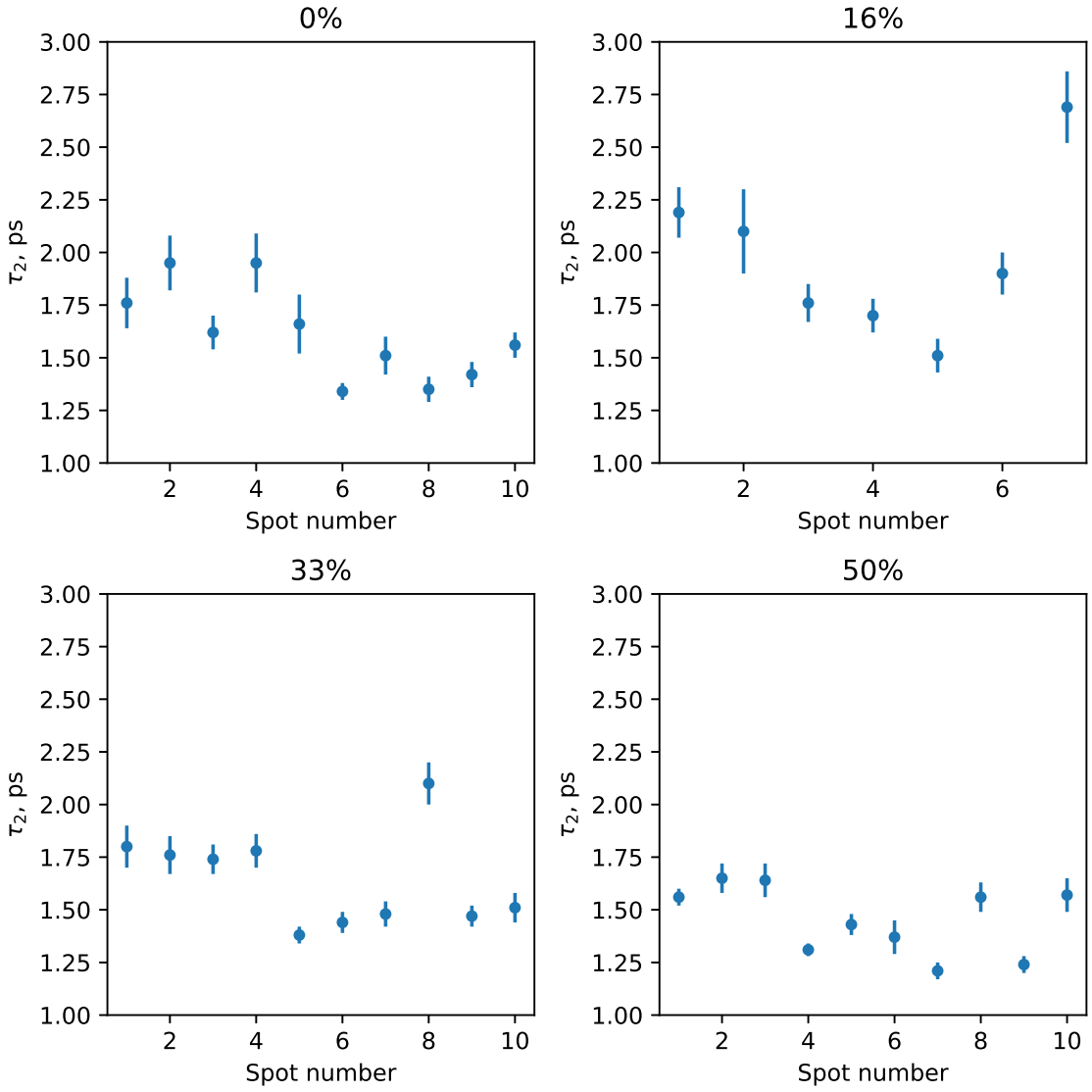

Figure 5.5: The extracted values of τ_2 from the bi-exponential fit to pump-probe data for each individual spot on each pattern of the substrate.

Chapter 6

Overview and conclusions

We investigated ultrafast carrier-phonon relaxation in graphene supported on a soda-lime glass substrate using transmission pump-probe spectroscopy. The range of applied pump fluences distinctly shows different regimes of transmission relaxation dynamics (see Figures 3.6, 3.7, 3.8 and 3.9). At low pump fluences, the differential transmission initially rises up after initial photoexcitation and then drops below zero due to prevailing induced absorption from the intraband transitions of the photoexcited electrons. At high pump fluences, the ultrafast optical response of graphene is positive, i.e. the differential transmission curve as a function of time delay lies entirely above zero due to dominating bleaching of the interband transitions by Pauli blocking. We studied the crossover from decreased to enhanced differential transmission, which occurs in the vicinity of the threshold pump fluence. The main result is the observation that there exists an order of magnitude faster decay of the differential transmission in the vicinity of the threshold pump fluence, at which the crossover from decreased to enhanced differential transmission occurs. This fact was verified by carrying out bi-exponential analysis of the ultrafast differential transmission relaxation curves. To better understand such unconventional behavior of the differential transmission, we applied a model for transmission of graphene on a substrate, which relates it to the optical conductivity depending on the time varying temperature of the Fermi-Dirac distributed electrons. The temporal evolution of electron temperature was modelled by a system of first order linear differential equations with constant coefficients describing the cooling of the electron system and the coupled optical phonons via emission of lower energy phonons, which possessed analytic solution conveniently relating temperature relaxation time constants to the phenomenological electron-phonon thermalization and optical phonon relaxation rates. Fitting the measured differential transmission spectra with

our model, which is generally based on previous models [68, 144, 41, 69], showed that the time constant characterizing the electronic temperature relaxation monotonically increases with pump fluence, while the relaxation time constant characterizing the differential transmission is non-monotonic and has a minimum in the vicinity of the threshold pump fluence as shown in Figure 4.2. Indeed, the phenomenological relaxation time constant of the optical phonons did not show any abrupt changes in the vicinity of the threshold pump fluence, from which it followed that there was no change in the electron relaxation mechanism. Approximately equal contribution (with opposite signs) of inter- and intraband terms to the optical conductivity in the vicinity of the threshold pump fluence results in the relaxation time constant for the differential transmission to be 10 times smaller as compared to high and low fluences. The value of the threshold pump fluence and the critical excited electron density, at which the faster relaxations are observed, increase with decreasing probe energies as the intraband absorption is greater at lower probe energies. Interestingly, it was also found that electron temperature took approximately ten times longer to relax as compared to the differential transmission in the region around the transition pump fluence. This suggests that the optical signal actually decays long before the excited electrons relax to the initial state. In conclusion, this work contributes an important crucial insight into the picture of inter- and intraband transitions influencing the ultrafast pump-probe response of graphene by investigating the crossover from the decreased to enhanced differential transmission regimes. The complete understanding of the dynamical ultrafast pump-probe optical response of graphene as well as carrier relaxation dynamics is of significance to fundamental graphene related research as well as to applications of graphene in ultrafast photonic devices. In particular, our new observation of an order of magnitude faster relaxation of the ultrafast pump-probe optical signal may find its application in saturable absorbers, where dynamic response, i.e. how fast it recovers, is one of the key parameters.

Appendix A

Relation between transmission and optical conductivity

Applying the optical boundary conditions at the air/graphene/substrate interfaces, the optical transmission $t(\omega)$ through the single layer graphene on a substrate normalized to the transmission through the substrate can be expressed as [143, 56]

$$t(\omega) = \frac{1}{|1+\sigma(\omega)Z_0/(1+n_s)|^2}, \tag{A.1}$$

where $\sigma(\omega)$ is the complex optical conductivity of graphene, Z_0 is the vacuum impedance and n_s is the refraction index of the substrate. Since the absolute value of the second term in the denominator of equation A.1 is much less than unity,

$$|\sigma(\omega)|Z_0/(1+n_s) \ll 1, \tag{A.2}$$

contribution of the imaginary part of the optical conductivity is negligible. Hence, the equation for transmission of the sample becomes

$$t(\omega) = \frac{1}{(1+\mathrm{Re}[\sigma(\omega)]Z_0/(1+n_s))^2 + (\mathrm{Im}[\sigma(\omega)]Z_0/(1+n_s))^2} \tag{A.3}$$

$$t(\omega) = \frac{1}{(1+\mathrm{Re}[\sigma(\omega)]Z_0/(1+n_s))^2}, \tag{A.4}$$

due to the fact that $\mathrm{Re}[\sigma(\omega)]Z_0/(1+n_s) \ll 1$ and $\mathrm{Im}[\sigma(\omega)]Z_0/(1+n_s) \ll 1$ The further simplification of equation A.4 may be achieved upon Taylor expansion.

$$t(\omega) = \frac{1}{1+2Re[\sigma(\omega)]Z_0/(1+n_s) + [Re[\sigma(\omega)]Z_0/(1+n_s)]^2}, \tag{A.5}$$

Since $\frac{1}{1+x} \approx 1-x$ for $x \ll 1$,

$$t(\omega) = 1 - 2Re[\sigma(\omega)]Z_0/(1+n_s) - [Re[\sigma(\omega)]Z_0/(1+n_s)]^2 \tag{A.6}$$

Keeping the terms up to the first order, transmission is approximated as follows

$$t(\omega) = 1 - 2Re[\sigma(\omega)]Z_0/(1+n_s) \tag{A.7}$$

Next, we can find the expression for $\frac{\Delta t}{t_0}$.

$$\frac{\Delta t}{t_0} = \frac{(1 - \frac{2Z_0}{1+n_s}Re\sigma) - (1 - \frac{2Z_0}{1+n_s}Re\sigma_0)}{1 - \frac{2Z_0}{1+n_s}Re\sigma_0} \tag{A.8}$$

$$\frac{\Delta t}{t_0} = \frac{-\frac{2Z_0}{1+n_s}\Delta Re\sigma}{1 - \frac{2Z_0}{1+n_s}Re\sigma_0} \tag{A.9}$$

Appendix B

Derivation of the electron temperature

The dynamics of electron temperature is approximated to be governed by the following system of first order linear differential equations corresponding to the two temperature model, where the electrons and strongly coupled optical phonons are described by temperatures T and T_{op}, respectively. The initial electron cooling occurs through the emission of optical phonons followed by the anharmonic decay into acoustic modes.

$$\begin{cases} \frac{dT}{dt} = \alpha(T_{op} - T), & T(0) = T_1, \\ \frac{dT_{op}}{dt} = \beta(T - T_{op}) + \gamma(T_0 - T_{op}), & T_{op}(0) = T_0, \\ \frac{dT_{ac}}{dt} = 0, & T_{ac}(0) = T_0, \end{cases} \tag{B.1}$$

where T, T_{op} and T_{ac} are the electron, optical and acoustic phonon temperatures, respectively, $\alpha = G_{el,op}/C_{el} > 0$, $\beta = G_{el,op}/C_{op} > 0$, $\gamma = G_{op,ac}/C_{op} > 0$ with G and C denoting coupling constants and heat capacities of electrons and phonons, and $\alpha \gg \beta, \gamma$. Ignoring temperature dependence of the coefficients α, β and γ, the given system of differential equations can be solved analytically. By subtracting the second equation from the first equation we get

$$\frac{d}{dt}(T - T_{op}) = -(\beta + \alpha)(T - T_{op}) + \gamma(T_{op} - T_0) \tag{B.2}$$

Upon differentiation equation B.2 becomes

$$\frac{d^2}{dt^2}(T - T_{op}) = -(\beta + \alpha)\frac{d}{dt}(T - T_{op}) + \gamma\frac{d}{dt}(T_{op} - T_0) \tag{B.3}$$

After plugging equation B.2 in to equation B.3 we obtain

$$\frac{d^2}{dt^2}(T - T_{op}) = -(\beta + \alpha)[-(\beta + \alpha)(T - T_{op}) + \gamma(T_{op} - T_0)] + \gamma \frac{d}{dt} T_{op} \tag{B.4}$$

Next, we plug the second equation from B.1 into equation B.4 to get

$$\frac{d^2}{dt^2}(T - T_{op}) = (\beta + \alpha)^2(T - T_{op}) + \gamma(\beta + \alpha)(T_{op} - T_0) + \gamma\beta(T - T_{op}) + \gamma^2(T_0 - T_{op}) \tag{B.5}$$

Combining like terms

$$\frac{d^2}{dt^2}(T - T_{op}) = [(\beta + \alpha)^2 + \gamma\beta](T - T_{op}) + [\gamma^2 + \gamma(\beta + \alpha)](T_0 - T_{op}) \tag{B.6}$$

Expressing $T_0 - T_{op}$ from equation B.2 and pluggnig it into equation B.6

$$\frac{d^2}{dt^2}(T - T_{op}) = [(\beta + \alpha)^2 + \gamma\beta](T - T_{op}) + [\gamma^2 + \gamma(\beta + \alpha)](-\frac{1}{\gamma})[(\alpha + \beta)(T - T_{op}) + \frac{d}{dt}(T - T_{op})] \tag{B.7}$$

Combining like terms

$$\frac{d^2}{dt^2}(T - T_{op}) = [(\beta + \alpha)^2 + \gamma\beta - \gamma(\beta + \alpha) - (\beta + \alpha)^2](T - T_{op}) - [\alpha + \beta + \gamma]\frac{d}{dt}(T - T_{op}) \tag{B.8}$$

$$\frac{d^2}{dt^2}(T - T_{op}) = [-\gamma\alpha](T - T_{op}) - [\alpha + \beta + \gamma]\frac{d}{dt}(T - T_{op}) \tag{B.9}$$

Finally, by moving all the terms to the left-hand side of the equation we bring the differential equation with respect to $T - T_{op}$ to a standard form

$$\frac{d^2}{dt^2}(T - T_{op}) + [\alpha + \beta + \gamma]\frac{d}{dt}(T - T_{op}) + [\alpha\gamma](T - T_{op}) = 0 \tag{B.10}$$

Thus, we have to solve a linear second-order homogeneous differential equation with constant coefficients. The corresponding characteristic equation is an algebraic quadratic equa-

tion

$$\lambda^2 + (\alpha+\beta+\gamma)\lambda + \alpha\gamma = 0 \tag{B.11}$$

The discriminant of the given quadratic equation is

$$D = (\alpha+\beta+\gamma)^2 - 4\alpha\gamma \tag{B.12}$$

Opening the brackets and combining like terms

$$D = \alpha^2+\beta^2+\gamma^2+2\alpha\beta+2\alpha\gamma+2\beta\gamma-4\alpha\gamma \tag{B.13}$$

$$D = \alpha^2+\beta^2+\gamma^2+2\alpha\beta+2\beta\gamma-2\alpha\gamma \tag{B.14}$$

$$D = \alpha^2+\beta^2+\gamma^2+2\alpha\beta-2\beta\gamma-2\alpha\gamma+4\beta\gamma \tag{B.15}$$

$$D = (\alpha+\beta-\gamma)^2+4\beta\gamma \tag{B.16}$$

The discriminant D is positive because $\alpha,\beta,\gamma > 0$. Thus,

$$D = (\alpha+\beta+\gamma)^2 - 4\alpha\gamma = (\alpha+\beta-\gamma)^2+4\beta\gamma > 0 \tag{B.17}$$

Hence, the characteristic equation has two real roots.

$$\lambda_1 = \frac{-(\alpha+\beta+\gamma)-\sqrt{(\alpha+\beta+\gamma)^2-4\alpha\gamma}}{2} = \frac{-(\alpha+\beta+\gamma)-\sqrt{(\alpha+\beta-\gamma)^2+4\beta\gamma}}{2} < 0 \tag{B.18}$$

$$\lambda_2 = \frac{-(\alpha+\beta+\gamma)+\sqrt{(\alpha+\beta+\gamma)^2-4\alpha\gamma}}{2} = \frac{-(\alpha+\beta+\gamma)+\sqrt{(\alpha+\beta-\gamma)^2+4\beta\gamma}}{2} < 0 \tag{B.19}$$

The solution to the differential equations is given by

$$T - T_{op} = C_1 e^{\lambda_1 t} + C_2 e^{\lambda_2 t}, \tag{B.20}$$

where C_1, C_2 are constants to be determined from the initial conditions. Particularly, by plugging in $t = 0$ in equation B.20 we obtain an equation relating C_1 and C_2.

$$T(t=0) - T_{op}(t=0) = T_1 - T_0 = C_1 + C_2 \tag{B.21}$$

Since ultimately we are looking for the electron temperature T, we plug equation B.20 into the differential equation B.1 for T.

$$\frac{dT}{dt} = -\alpha(C_1 e^{\lambda_1 t} + C_2 e^{\lambda_2 t}) \tag{B.22}$$

By taking the antiderivative we get

$$T = -\frac{\alpha C_1}{\lambda_1} e^{\lambda_1 t} - \frac{\alpha C_2}{\lambda_2} e^{\lambda_2 t} + C_3 \tag{B.23}$$

The constant of integration C_3 is determined by plugging in $t \to +\infty$. The first two terms vanish because the coefficients λ_1 and λ_2 are negative.

$$T(t \to +\infty) = T_0 = C_3 \tag{B.24}$$

By plugging $t = 0$ into equation B.23 and combining it with equation B.21 we get two equations with respect to C_1 and C_2.

$$T_1 = -\frac{\alpha C_1}{\lambda_1} - \frac{\alpha C_2}{\lambda_2} + T_0 \tag{B.25}$$

$$C_1 + C_2 = T_1 - T_0 \tag{B.26}$$

Plugging C_2 from equation B.26 into equation B.25

$$T_1 = -\frac{\alpha C_1}{\lambda_1} - \frac{\alpha}{\lambda_2}(T_1 - T_0 - C_1) + T_0 \tag{B.27}$$

$$T_1 - T_0 = C_1\alpha(\frac{1}{\lambda_2} - \frac{1}{\lambda_1}) - \frac{\alpha}{\lambda_2}(T_1 - T_0) \tag{B.28}$$

$$C_1 = \frac{\frac{1}{\alpha} + \frac{1}{\lambda_2}}{\frac{1}{\lambda_2} - \frac{1}{\lambda_1}}(T_1 - T_0) \tag{B.29}$$

We find C_2 by plugging C_1 into equation B.26.

$$C_2 = (1 - \frac{\frac{1}{\alpha} + \frac{1}{\lambda_2}}{\frac{1}{\lambda_2} - \frac{1}{\lambda_1}})(T_1 - T_0) \tag{B.30}$$

$$C_2 = -\frac{\frac{1}{\alpha} + \frac{1}{\lambda_1}}{\frac{1}{\lambda_2} - \frac{1}{\lambda_1}}(T_1 - T_0) \tag{B.31}$$

Thus, the equation for the electron temperature is

$$T = (T_1 - T_0)(c_1 e^{\lambda_1 t} + c_2 e^{\lambda_2 t}) + T_0, \tag{B.32}$$

where c_1 and c_2 are given by

$$c_1 = \frac{\alpha}{\lambda_1}\frac{\frac{1}{\alpha} + \frac{1}{\lambda_2}}{\frac{1}{\lambda_1} - \frac{1}{\lambda_2}} \tag{B.33}$$

$$c_2 = \frac{\alpha}{\lambda_2}\frac{\frac{1}{\alpha} + \frac{1}{\lambda_1}}{\frac{1}{\lambda_2} - \frac{1}{\lambda_1}} \tag{B.34}$$

Next, we perform some algebraic operation to cast the expressions for c_1 and c_2 into a more sensible and beautiful form.

$$c_1 = \frac{1 + \frac{\alpha}{\lambda_2}}{1 - \frac{\lambda_1}{\lambda_2}} \tag{B.35}$$

$$c_1 = \frac{\alpha + \lambda_2}{\lambda_2 - \lambda_1} \tag{B.36}$$

After plugging in the expressions B.18 and B.19 for λ_1 and λ_2, respectively, we get

$$c_1 = \frac{\alpha - \frac{\alpha+\beta+\gamma-\sqrt{(\alpha+\beta+\gamma)^2-4\alpha\gamma}}{2}}{\sqrt{(\alpha+\beta+\gamma)^2 - 4\alpha\gamma}} \tag{B.37}$$

$$c_1 = \frac{\alpha - \beta - \gamma + \sqrt{(\alpha+\beta+\gamma)^2 - 4\alpha\gamma}}{2\sqrt{(\alpha+\beta+\gamma)^2 - 4\alpha\gamma}} \tag{B.38}$$

The expression under the square root is transformed in the following way

$$(\alpha+\beta+\gamma)^2 - 4\alpha\gamma = \alpha^2 + \beta^2 + \gamma^2 + 2\alpha\beta + 2\alpha\gamma + 2\beta\gamma - 4\alpha\gamma \tag{B.39}$$

$$(\alpha+\beta+\gamma)^2 - 4\alpha\gamma = \alpha^2 + \beta^2 + \gamma^2 - 2\alpha\beta - 2\alpha\gamma + 2\beta\gamma + 4\alpha\beta \tag{B.40}$$

$$(\alpha+\beta+\gamma)^2 - 4\alpha\gamma = (\alpha - \beta - \gamma)^2 + 4\alpha\beta \tag{B.41}$$

By plugging equation B.41 into equation B.38, we get

$$c_1 = \frac{(\alpha - \beta - \gamma) + \sqrt{(\alpha - \beta - \gamma)^2 + 4\alpha\beta}}{2\sqrt{(\alpha - \beta - \gamma)^2 + 4\alpha\beta}} > 0, \tag{B.42}$$

due to $\alpha \gg \beta, \gamma$. We carry out similar algebraic operations for c_2.

$$c_2 = \frac{\alpha}{\lambda_2} \frac{\frac{1}{\alpha} + \frac{1}{\lambda_1}}{\frac{1}{\lambda_2} - \frac{1}{\lambda_1}} \tag{B.43}$$

$$c_2 = \frac{1 + \frac{\alpha}{\lambda_1}}{1 - \frac{\lambda_2}{\lambda_1}} \tag{B.44}$$

$$c_2 = \frac{\alpha + \lambda_1}{\lambda_1 - \lambda_2} \tag{B.45}$$

Using equations B.18 and B.19 for λ_1 and λ_2, respectively, we get

$$c_2 = \frac{\alpha + \frac{-(\alpha+\beta+\gamma) - \sqrt{(\alpha+\beta+\gamma)^2 - 4\alpha\gamma}}{2}}{-\sqrt{(\alpha+\beta+\gamma)^2 - 4\alpha\gamma}} \tag{B.46}$$

$$c_2 = \frac{\alpha - \beta - \gamma - \sqrt{(\alpha+\beta+\gamma)^2 - 4\alpha\gamma}}{-2\sqrt{(\alpha+\beta+\gamma)^2 - 4\alpha\gamma}} \tag{B.47}$$

Using equation B.41 for the expression under the square root

$$c_2 = \frac{-(\alpha-\beta-\gamma)+\sqrt{(\alpha-\beta-\gamma)^2+4\alpha\beta}}{2\sqrt{(\alpha-\beta-\gamma)^2+4\alpha\beta}} > 0 \tag{B.48}$$

By plugging equations B.42 and B.48 for c_1 and c_2, respectively, in the equation B.32, we get

$$T = \frac{T_1-T_0}{2}[(1+k)e^{\lambda_1 t}+(1-k)e^{\lambda_2 t}]+T_0, \tag{B.49}$$

where $k = \frac{\alpha-\beta-\gamma}{\sqrt{(\alpha-\beta-\gamma)^2+4\alpha\beta}}$. Since $\alpha \gg \beta, \gamma$, it follows that $0 < k < 1$. Equation B.49 can be rewritten as

$$T = \frac{T_1-T_0}{2}[(1+k)e^{-\frac{t}{\tau_1}}+(1-k)e^{-\frac{t}{\tau_2}}]+T_0, \tag{B.50}$$

where

$$\tau_1 = -\frac{1}{\lambda_1} = \frac{2}{(\alpha+\beta+\gamma)+\sqrt{(\alpha+\beta-\gamma)^2+4\beta\gamma}} \tag{B.51}$$

$$\tau_2 = -\frac{1}{\lambda_2} = \frac{2}{(\alpha+\beta+\gamma)-\sqrt{(\alpha+\beta-\gamma)^2+4\beta\gamma}} \tag{B.52}$$

From equations B.51 and B.52 it follows that $0 < \tau_1 < \tau_2$. Thus, the electron temperature $T(t)$ is a biexponential function of time with τ_1 and τ_2 characterizing the faster and the slower relaxation components, respectively. Since in our case $\alpha \gg \beta, \gamma$, the expressions for τ_1 and τ_2 can assume much simpler form. Starting with equation B.51 and factoring out $(\alpha+\beta-\gamma)^2$ from the square root, we get

$$\tau_1 = \frac{2}{(\alpha+\beta+\gamma)+(\alpha+\beta-\gamma)\sqrt{1+\frac{4\beta\gamma}{(\alpha+\beta-\gamma)^2}}} \tag{B.53}$$

Since $\frac{4\beta\gamma}{(\alpha+\beta-\gamma)^2} \ll 1$ due to $\alpha \gg \beta, \gamma$, we can do Taylor expansion on the square root to get

$$\tau_1 = \frac{2}{(\alpha+\beta+\gamma)+(\alpha+\beta-\gamma)(1+\frac{1}{2}\frac{4\beta\gamma}{(\alpha+\beta-\gamma)^2}+o(\frac{1}{\alpha^4}))} \tag{B.54}$$

$$\tau_1 = \frac{2}{\alpha+\beta+\gamma+\alpha+\beta-\gamma+\frac{1}{2}\frac{4\beta\gamma}{\alpha+\beta-\gamma}+o(\frac{1}{\alpha^3})} \tag{B.55}$$

$$\tau_1 = \frac{2}{2(\alpha+\beta)+\frac{2\beta\gamma}{\alpha+\beta-\gamma}+o(\frac{1}{\alpha^3})} \tag{B.56}$$

$$\tau_1 = \frac{1}{\alpha+\beta+\frac{\beta\gamma}{\alpha+\beta-\gamma}+o(\frac{1}{\alpha^3})} \tag{B.57}$$

Hence, to first order we have $\tau_1 \approx \frac{1}{\alpha}$ Similarly, we run the same simplifications for τ_2.

$$\tau_2 = \frac{2}{(\alpha+\beta+\gamma)-(\alpha+\beta-\gamma)\sqrt{1+\frac{4\beta\gamma}{(\alpha+\beta-\gamma)^2}}} \tag{B.58}$$

$$\tau_2 = \frac{2}{(\alpha+\beta+\gamma)-(\alpha+\beta-\gamma)(1+\frac{1}{2}\frac{4\beta\gamma}{(\alpha+\beta-\gamma)^2}+o(\frac{1}{\alpha^4}))} \tag{B.59}$$

$$\tau_2 = \frac{2}{\alpha+\beta+\gamma-\alpha-\beta+\gamma-\frac{2\beta\gamma}{\alpha+\beta-\gamma}-o(\frac{1}{\alpha^3})} \tag{B.60}$$

$$\tau_2 = \frac{1}{\gamma-\frac{\beta\gamma}{\alpha+\beta-\gamma}-o(\frac{1}{\alpha^3})} \tag{B.61}$$

$$\tau_2 = \frac{1}{\gamma-\gamma o(\frac{1}{\alpha})} \tag{B.62}$$

Consequently, to first order we have $\tau_2 \approx \frac{1}{\gamma}$. Thus, the expressions for τ_1 and τ_2 imply that τ_1 characterizes the electron-phonon thermalization and τ_2 characterizes the hot optical phonon relaxation. Finally, the electron temperature as a function of time can be written as

$$T(t) = \frac{T_1-T_0}{2}[(1+k)e^{-\frac{t}{\tau_{e-ph}}}+(1-k)e^{-\frac{t}{\tau_{op}}}]+T_0, \tag{B.63}$$

where $k = \frac{\alpha-\beta-\gamma}{\sqrt{(\alpha-\beta-\gamma)^2+4\alpha\beta}}$, $\tau_{e-ph} = \frac{1}{\alpha}$ and $\tau_{op} = \frac{1}{\gamma}$.

BIBLIOGRAPHY

[1] D. Brida, A. Tomadin, C. Manzoni, Y. J. Kim, A. Lombardo, S. Milana, R. R. Nair, K. S. Novoselov, A. C. Ferrari, G. Cerullo, and et al. Ultrafast collinear scattering and carrier multiplication in graphene. *Nature Communications*, 4(1), Jun 2013.

[2] Jahan M. Dawlaty, Shriram Shivaraman, Mvs Chandrashekhar, Farhan Rana, and Michael G. Spencer. Measurement of ultrafast carrier dynamics in epitaxial graphene. *Applied Physics Letters*, 92(4):042116, 2008.

[3] Faris Kadi, Torben Winzer, Ermin Malic, Andreas Knorr, F. Göttfert, M. Mittendorff, S. Winnerl, and M. Helm. Microscopic description of intraband absorption in graphene: The occurrence of transient negative differential transmission. *Phys. Rev. Lett.*, 113:035502, Jul 2014.

[4] Antonio Maffucci, Sergey Maksimenko, Giovanni Miano, and Gregory Slepyan. *Electrical Conductivity of Carbon Nanotubes: Modeling and Characterization*, pages 101–128. 01 2017.

[5] Zeynab Jarrahi. *Effect of Substrate and Morphology on the Relaxation Dynamics of Carriers and Phonons in Graphene*. PhD thesis, Vanderbilt University, 2016.

[6] Ibraheem Al-Naib, J. Sipe, and Marc Dignam. High harmonic generation in undoped graphene: Interplay of inter- and intraband dynamics. *Physical Review B*, 07 2014.

[7] Kin Fai Mak, Long Ju, Feng Wang, and Tony F. Heinz. Optical spectroscopy of graphene: From the far infrared to the ultraviolet. *Solid State Communications*, 152(15):1341 – 1349, 2012. Exploring Graphene, Recent Research Advances.

[8] Kemal Celebi, Matthew T. Cole, Jong Won Choi, Frederic Wyczisk, Pierre Legagneux, Nalin Rupesinghe, John Robertson, Kenneth B. K. Teo, and Hyung Gyu Park.

Evolutionary kinetics of graphene formation on copper. *Nano Letters*, 13(3):967–974, 2013. PMID: 23339597.

[9] Mark Fox. *Optical Properties of Solids*, volume 70. 01 2001.

[10] Andrea C. Ferrari and Denis M. Basko. Raman spectroscopy as a versatile tool for studying the properties of graphene. *Nature Nanotechnology*, 8(4):235–246, Apr 2013.

[11] R Saito, G Dresselhaus, and M S Dresselhaus. *Physical Properties of Carbon Nanotubes*. PUBLISHED BY IMPERIAL COLLEGE PRESS AND DISTRIBUTED BY WORLD SCIENTIFIC PUBLISHING CO., 1998.

[12] L.M. Malard, M.A. Pimenta, G. Dresselhaus, and M.S. Dresselhaus. Raman spectroscopy in graphene. *Physics Reports*, 473(5):51 – 87, 2009.

[13] Jih-Shang Hwang, Yu-Hsiang Lin, Jeong-Yuan Hwang, Railing Chang, Surojit Chattopadhyay, Chang-Jiang Chen, Peilin Chen, Hai-Pang Chiang, Tsong-Ru Tsai, Li-Chyong Chen, and Kuei-Hsien Chen. Imaging layer number and stacking order through formulating raman fingerprints obtained from hexagonal single crystals of few layer graphene. *Nanotechnology*, 24(1):015702, dec 2012.

[14] A. Das, S. Pisana, B. Chakraborty, S. Piscanec, S. K. Saha, U. V. Waghmare, K. S. Novoselov, H. R. Krishnamurthy, A. K. Geim, A. C. Ferrari, and et al. Monitoring dopants by raman scattering in an electrochemically top-gated graphene transistor. *Nature Nanotechnology*, 3(4):210215, Mar 2008.

[15] Rohit P Prasankumar and Antoinette J Taylor. *Optical techniques for solid-state materials characterization*. CRC Press, 2016.

[16] Andrej Gross, Felix Stangl, Katharina Hoenes, Michael Sift, and Martin Hessling.

Improved drinking water disinfection with uvc-leds for escherichia coli and bacillus subtilis utilizing quartz tubes as light guide. *Water*, pages 4605–4621, 2015.

[17] T Deschamps, C Martinet, J L Bruneel, and B Champagnon. Soda-lime silicate glass under hydrostatic pressure and indentation: a micro-raman study. *Journal of Physics: Condensed Matter*, 23(3):035402, jan 2011.

[18] Rustam Gatamov, Andrey Baydin, Halina Krzyzanowska, and Norman Tolk. Fluence and wavelength dependent ultrafast differential transmission dynamics in graphene. *Materials Research Express*, 7(9):095601, sep 2020.

[19] Ji Eun Lee, Gwanghyun Ahn, Jihye Shim, Young Sik Lee, and Sunmin Ryu. Optical separation of mechanical strain from charge doping in graphene. *Nature Communications*, 3(1):1024, jan 2012.

[20] A. Das, B. Chakraborty, S. Piscanec, S. Pisana, A. K. Sood, and A. C. Ferrari. Phonon renormalization in doped bilayer graphene. *Phys. Rev. B*, 79:155417, Apr 2009.

[21] Guillaume Froehlicher and Stéphane Berciaud. Raman spectroscopy of electrochemically gated graphene transistors: Geometrical capacitance, electron-phonon, electron-electron, and electron-defect scattering. *Phys. Rev. B*, 91:205413, May 2015.

[22] A. H. Castro Neto, F. Guinea, N. M. R. Peres, K. S. Novoselov, and A. K. Geim. The electronic properties of graphene. *Rev. Mod. Phys.*, 81:109–162, Jan 2009.

[23] F. Bonaccorso, Z. Sun, T. Hasan, and A. C. Ferrari. Graphene photonics and optoelectronics. *Nature Photonics*, 4:611–622, Aug 2010.

[24] N. M. R. Peres. Colloquium: The transport properties of graphene: An introduction. *Rev. Mod. Phys.*, 82:2673–2700, Sep 2010.

[25] N. M. Gabor, J. C. W. Song, Q. Ma, N. L. Nair, T. Taychatanapat, K. Watanabe, T. Taniguchi, L. S. Levitov, and P. Jarillo-Herrero. Hot carrierassisted intrinsic photoresponse in graphene. *Science*, 334:648–652, Nov 2011.

[26] Zhipei Sun, Tawfique Hasan, Felice Torrisi, Daniel Popa, Giulia Privitera, Fengqiu Wang, Francesco Bonaccorso, Denis M. Basko, and Andrea C. Ferrari. Graphene mode-locked ultrafast laser. *ACS Nano*, 4(2):803–810, 2010.

[27] Ming Liu, Xiabo Yin, Erick Ulin-Avila, Baisong Geng, Thomas Zentgraf, Long Ju, Feng Wang, and Xiang Zhang. A graphene-based broadband optical modulator. *Nature*, 474:64–67, 2011.

[28] Fengnian Xia, Thomas Mueller, Roksana Golizadeh-Mojarad, Marcus Freitag, Yuming Lin, James Tsang, Vasili Perebeinos, and Phaedon Avouris. Photocurrent imaging and efficient photon detection in a graphene transistor. *Nano Letters*, 9(3):1039–1044, 2009.

[29] Zhenxing Wang, Zhiyong Zhang, Huilong Xu, Li Ding, Sheng Wang, and Lian-Mao Peng. A high-performance top-gate graphene field-effect transistor based frequency doubler. *Applied Physics Letters*, 96(17):173104, 2010.

[30] F. Rana. Graphene terahertz plasmon oscillators. *IEEE Transactions on Nanotechnology*, 7(1):91–99, 2008.

[31] R. Bistritzer and A. H. MacDonald. Hydrodynamic theory of transport in doped graphene. *Phys. Rev. B*, 80:085109, Aug 2009.

[32] Jiwoong Park, Y. H. Ahn, and Carlos Ruiz-Vargas. Imaging of photocurrent generation and collection in single-layer graphene. *Nano Letters*, 9(5):1742–1746, 2009. PMID: 19326919.

[33] Kwangu Kang, Daner Abdula, David G. Cahill, and Moonsub Shim. Lifetimes of optical phonons in graphene and graphite by time-resolved incoherent anti-stokes raman scattering. *Phys. Rev. B*, 81:165405, Apr 2010.

[34] M. Breusing, S. Kuehn, T. Winzer, E. Malić, F. Milde, N. Severin, J. P. Rabe, C. Ropers, A. Knorr, and T. Elsaesser. Ultrafast nonequilibrium carrier dynamics in a single graphene layer. *Phys. Rev. B*, 83:153410, Apr 2011.

[35] Dong Sun, Zong-Kwei Wu, Charles Divin, Xuebin Li, Claire Berger, Walt A. de Heer, Phillip N. First, and Theodore B. Norris. Ultrafast relaxation of excited dirac fermions in epitaxial graphene using optical differential transmission spectroscopy. *Phys. Rev. Lett.*, 101:157402, Oct 2008.

[36] Ryan W. Newson, Jesse Dean, Ben Schmidt, and Henry M. van Driel. Ultrafast carrier kinetics in exfoliated graphene and thin graphite films. *Opt. Express*, 17(4):2326–2333, Feb 2009.

[37] Brian A. Ruzicka, Shuai Wang, Jianwei Liu, Kian-Ping Loh, Judy Z. Wu, and Hui Zhao. Spatially resolved pump-probe study of single-layer graphene produced by chemical vapor deposition. *Opt. Mater. Express*, 2(6):708–716, Jun 2012.

[38] Kuan-Chun Lin, Ming-Yang Li, L. J. Li, D. C. Ling, C. C. Chi, and Jeng-Chung Chen. Ultrafast dynamics of hot electrons and phonons in chemical vapor deposited graphene. *Journal of Applied Physics*, 113(13):133511, 2013.

[39] Haining Wang, Jared H. Strait, Paul A. George, Shriram Shivaraman, Virgil B. Shields, Mvs Chandrashekhar, Jeonghyun Hwang, Farhan Rana, Michael G. Spencer, Carlos S. Ruiz-Vargas, and Jiwoong Park. Ultrafast relaxation dynamics of hot optical phonons in graphene. *Applied Physics Letters*, 96(8):081917, 2010.

[40] Dheeraj Golla, Alexandra Brasington, Brian J. LeRoy, and Arvinder Sandhu. Ul-

trafast relaxation of hot phonons in graphene-hbn heterostructures. *APL Materials*, 5(5):056101, 2017.

[41] Leandro M Malard, Kin Fai Mak, A H Castro Neto, N M R Peres, and Tony F Heinz. Observation of intra- and inter-band transitions in the transient optical response of graphene. *New Journal of Physics*, 15(1):015009, 2013.

[42] Jens Christian Johannsen, Søren Ulstrup, Federico Cilento, Alberto Crepaldi, Michele Zacchigna, Cephise Cacho, I. C. Edmond Turcu, Emma Springate, Felix Fromm, Christian Raidel, Thomas Seyller, Fulvio Parmigiani, Marco Grioni, and Philip Hofmann. Direct view of hot carrier dynamics in graphene. *Phys. Rev. Lett.*, 111:027403, Jul 2013.

[43] Torben Winzer, Andreas Knorr, and Ermin Malic. Carrier multiplication in graphene. *Nano Letters*, 10(12):4839–4843, 2010. PMID: 21053963.

[44] E. H. Hwang, Ben Yu-Kuang Hu, and S. Das Sarma. Inelastic carrier lifetime in graphene. *Physical Review B*, 76(11), Sep 2007.

[45] Ermin Malic, Torben Winzer, Evgeny Bobkin, and Andreas Knorr. Microscopic theory of absorption and ultrafast many-particle kinetics in graphene. *Phys. Rev. B*, 84:205406, Nov 2011.

[46] J. M. Iglesias, M. J. Martn, E. Pascual, and R. Rengel. Hot carrier and hot phonon coupling during ultrafast relaxation of photoexcited electrons in graphene. *Applied Physics Letters*, 108(4):043105, 2016.

[47] Bo Gao, Gregory Hartland, Tian Fang, Michelle Kelly, Debdeep Jena, Huili (Grace) Xing, and Libai Huang. Studies of intrinsic hot phonon dynamics in suspended graphene by transient absorption microscopy. *Nano Letters*, 11(8):3184–3189, 2011. PMID: 21696177.

[48] Tony Low, Vasili Perebeinos, Raseong Kim, Marcus Freitag, and Phaedon Avouris. Cooling of photoexcited carriers in graphene by internal and substrate phonons. *Phys. Rev. B*, 86:045413, Jul 2012.

[49] E. H. Hwang and S. Das Sarma. Surface polar optical phonon interaction induced many-body effects and hot-electron relaxation in graphene. *Phys. Rev. B*, 87:115432, Mar 2013.

[50] Seongjin Ahn, E. H. Hwang, and Hongki Min. Inelastic carrier lifetime in a coupled graphene/electron-phonon system: Role of plasmon-phonon coupling. *Phys. Rev. B*, 90:245436, Dec 2014.

[51] Klaas-Jan Tielrooij, Niels CH Hesp, Alessandro Principi, Mark B Lundeberg, Eva AA Pogna, Luca Banszerus, Zoltán Mics, Mathieu Massicotte, Peter Schmidt, Diana Davydovskaya, et al. Out-of-plane heat transfer in van der waals stacks through electron–hyperbolic phonon coupling. *Nature nanotechnology*, 13(1):41, 2018.

[52] Nicola Bonini, Michele Lazzeri, Nicola Marzari, and Francesco Mauri. Phonon anharmonicities in graphite and graphene. *Phys. Rev. Lett.*, 99:176802, Oct 2007.

[53] Michele Lazzeri, S. Piscanec, Francesco Mauri, A. C. Ferrari, and J. Robertson. Electron transport and hot phonons in carbon nanotubes. *Phys. Rev. Lett.*, 95:236802, Nov 2005.

[54] Eric Pop, David Mann, Jien Cao, Qian Wang, Kenneth Goodson, and Hongjie Dai. Negative differential conductance and hot phonons in suspended nanotube molecular wires. *Phys. Rev. Lett.*, 95:155505, Oct 2005.

[55] Jing Li, Henrique Pereira Coutada Miranda, Yann-Michel Niquet, Luigi Genovese, Ivan Duchemin, Ludger Wirtz, and Christophe Delerue. Phonon-limited carrier mo-

bility and resistivity from carbon nanotubes to graphene. *Phys. Rev. B*, 92:075414, Aug 2015.

[56] Jahan M. Dawlaty, Shriram Shivaraman, Jared Strait, Paul George, Mvs Chandrashekhar, Farhan Rana, Michael G. Spencer, Dmitry Veksler, and Yunqing Chen. Measurement of the optical absorption spectra of epitaxial graphene from terahertz to visible. *Applied Physics Letters*, 93(13):131905, 2008.

[57] Jahan M. Dawlaty, Shriram Shivaraman, Mvs Chandrashekhar, Farhan Rana, and Michael G. Spencer. Measurement of ultrafast carrier dynamics in epitaxial graphene. *Applied Physics Letters*, 92(4):042116, 2008.

[58] Ke Chen, Huihui Li, Lai-Peng Ma, Wencai Ren, Ting-Fung Chung, Hui-Ming Cheng, Yong P. Chen, and Tianshu Lai. Diversity of ultrafast hot-carrier-induced dynamics and striking sub-femtosecond hot-carrier scattering times in graphene. *Carbon*, 72:402–409, jun 2014.

[59] Min Guo, Lai-Peng Ma, Wencai Ren, and Tianshu Lai. Control of the ultrafast photo-electronic dynamics of a chemical-vapor-deposited-grown graphene by ozone oxidation. *Photonics Res.*, 8(1):17–23, 2020.

[60] Jingzhi Shang, Zhiqiang Luo, Chunxiao Cong, Jianyi Lin, Ting Yu, and Gagik G Gurzadyan. Femtosecond uv-pump/visible-probe measurements of carrier dynamics in stacked graphene films. *Appl. Phys. Lett.*, 97(16):163103, 2010.

[61] Jingzhi Shang, Ting Yu, Jianyi Lin, and Gagik G. Gurzadyan. Ultrafast electron-optical phonon scattering and quasiparticle lifetime in CVD-grown graphene. *ACS Nano*, 5(4):3278–3283, 2011. PMID: 21391596.

[62] Libai Huang, Bo Gao, Gregory Hartland, Michelle Kelly, and HuiLi Xing. Ultrafast relaxation of hot optical phonons in monolayer and multilayer graphene on different

substrates. *Surface Science*, 605(17):1657 – 1661, 2011. Graphene Surfaces and Interfaces.

[63] Shuntaro Tani, François Blanchard, and Koichiro Tanaka. Ultrafast carrier dynamics in graphene under a high electric field. *Phys. Rev. Lett.*, 109(16):166603, 2012.

[64] Xin Zhao, Zhi-Bo Liu, Wei-Bo Yan, Yingpeng Wu, Xiao-Liang Zhang, Yongsheng Chen, and Jian-Guo Tian. Ultrafast carrier dynamics and saturable absorption of solution-processable few-layered graphene oxide. *Applied Physics Letters*, 98(12):121905, 2011.

[65] Brian A Ruzicka, Lalani K Werake, Hui Zhao, Shuai Wang, and Kian Ping Loh. Femtosecond pump-probe studies of reduced graphene oxide thin films. *Appl. Phys. Lett.*, 96(17):173106, 2010.

[66] Libai Huang, Gregory V. Hartland, Li-Qiang Chu, Luxmi, Randall M. Feenstra, Chuanxin Lian, Kristof Tahy, and Huili Xing. Ultrafast transient absorption microscopy studies of carrier dynamics in epitaxial graphene. *Nano Letters*, 10(4):1308–1313, 2010. PMID: 20210348.

[67] Paul A George, Jared Strait, Jahan Dawlaty, Shriram Shivaraman, Mvs Chandrashekhar, Farhan Rana, and Michael G Spencer. Ultrafast optical-pump terahertz-probe spectroscopy of the carrier relaxation and recombination dynamics in epitaxial graphene. *Nano Lett.*, 8(12):4248–4251, 2008.

[68] H. Choi, F. Borondics, D. A. Siegel, S. Y. Zhou, M. C. Martin, A. Lanzara, and R. A. Kaindl. Broadband electromagnetic response and ultrafast dynamics of few-layer epitaxial graphene. *Applied Physics Letters*, 94(17):172102, 2009.

[69] Ke Chen, Maruthi Nagavalli Yogeesh, Yuan Huang, Shaoqing Zhang, Feng He, Xianghai Meng, Shaoyin Fang, Nathanial Sheehan, Tiger Hu Tao, Seth R. Bank,

Jung-Fu Lin, Deji Akinwande, Peter Sutter, Tianshu Lai, and Yaguo Wang. Non-destructive measurement of photoexcited carrier transport in graphene with ultrafast grating imaging technique. *Carbon*, 107:233 – 239, 2016.

[70] Faris Kadi, Torben Winzer, Ermin Malic, Andreas Knorr, F. Göttfert, M. Mittendorff, S. Winnerl, and M. Helm. Microscopic description of intraband absorption in graphene: The occurrence of transient negative differential transmission. *Phys. Rev. Lett.*, 113:035502, Jul 2014.

[71] Ryan J Suess, Stephan Winnerl, Harald Schneider, Manfred Helm, Claire Berger, Walter A de Heer, Thomas E Murphy, and Martin Mittendorff. Role of transient reflection in graphene nonlinear infrared optics. *ACS photonics*, 3(6):1069, 2016.

[72] Daniel R. Cooper, Benjamin D'Anjou, Nageswara Ghattamaneni, Benjamin Harack, Michael Hilke, Alexandre Horth, Norberto Majlis, Mathieu Massicotte, Leron Vandsburger, Eric Whiteway, and Victor Yu. Experimental review of graphene, 2011.

[73] I. W. Frank, D. M. Tanenbaum, A. M. van der Zande, and P. L. McEuen. Mechanical properties of suspended graphene sheets. *Journal of Vacuum Science & Technology B: Microelectronics and Nanometer Structures Processing, Measurement, and Phenomena*, 25(6):2558–2561, 2007.

[74] Changgu Lee, Xiaoding Wei, Jeffrey W. Kysar, and James Hone. Measurement of the elastic properties and intrinsic strength of monolayer graphene. *Science*, 321(5887):385–388, 2008.

[75] Alexander A. Balandin, Suchismita Ghosh, Wenzhong Bao, Irene Calizo, Desalegne Teweldebrhan, Feng Miao, and Chun Ning Lau. Superior thermal conductivity of single-layer graphene. *Nano Letters*, 8(3):902–907, 2008. PMID: 18284217.

[76] P. R. Wallace. The band theory of graphite. *Phys. Rev.*, 71:622–634, May 1947.

[77] A. Grüneis, C. Attaccalite, L. Wirtz, H. Shiozawa, R. Saito, T. Pichler, and A. Rubio. Tight-binding description of the quasiparticle dispersion of graphite and few-layer graphene. *Phys. Rev. B*, 78:205425, Nov 2008.

[78] K. I. Bolotin, K. J. Sikes, J. Hone, H. L. Stormer, and P. Kim. Temperature-dependent transport in suspended graphene. *Phys. Rev. Lett.*, 101:096802, Aug 2008.

[79] Claire Berger, Zhimin Song, Xuebin Li, Xiaosong Wu, Nate Brown, Cécile Naud, Didier Mayou, Tianbo Li, Joanna Hass, Alexei N. Marchenkov, Edward H. Conrad, Phillip N. First, and Walt A. de Heer. Electronic confinement and coherence in patterned epitaxial graphene. *Science*, 312(5777):1191–1196, 2006.

[80] A. B. Kuzmenko, E. van Heumen, F. Carbone, and D. van der Marel. Universal optical conductance of graphite. *Physical Review Letters*, 100(11), Mar 2008.

[81] Thomas Mueller, Fengnian Xia, and Phaedon Avouris. Graphene photodetectors for high-speed optical communications. *Nature Photonics*, 4(5):297301, Mar 2010.

[82] Z. Sun, T. Hasan, and A.C. Ferrari. Ultrafast lasers mode-locked by nanotubes and graphene. *Physica E: Low-dimensional Systems and Nanostructures*, 44(6):1082 – 1091, 2012. The proceedings of the European Materials Research Symposium on Science and Technology of Nanotubes, Nanowires and Graphene.

[83] L. A. Falkovsky and A. A. Varlamov. Space-time dispersion of graphene conductivity. *The European Physical Journal B*, 56(4):281284, Apr 2007.

[84] L A Falkovsky. Optical properties of graphene. *Journal of Physics: Conference Series*, 129:012004, oct 2008.

[85] T. Stauber, N. M. R. Peres, and A. K. Geim. Optical conductivity of graphene in the visible region of the spectrum. *Phys. Rev. B*, 78:085432, Aug 2008.

[86] Kin Fai Mak, Jie Shan, and Tony F. Heinz. Seeing many-body effects in single- and few-layer graphene: Observation of two-dimensional saddle-point excitons. *Phys. Rev. Lett.*, 106:046401, Jan 2011.

[87] Toshiyuki Kobayashi, Masashi Bando, Nozomi Kimura, Keisuke Shimizu, Koji Kadono, Nobuhiko Umezu, Kazuhiko Miyahara, Shinji Hayazaki, Sae Nagai, Yukiko Mizuguchi, Yosuke Murakami, and Daisuke Hobara. Production of a 100-m-long high-quality graphene transparent conductive film by roll-to-roll chemical vapor deposition and transfer process. *Applied Physics Letters*, 102(2):023112, 2013.

[88] Adam W. Tsen, Lola Brown, Mark P. Levendorf, Fereshte Ghahari, Pinshane Y. Huang, Robin W. Havener, Carlos S. Ruiz-Vargas, David A. Muller, Philip Kim, and Jiwoong Park. Tailoring electrical transport across grain boundaries in polycrystalline graphene. *Science*, 336(6085):1143–1146, 2012.

[89] Xuelei Liang, Brent A. Sperling, Irene Calizo, Guangjun Cheng, Christina Ann Hacker, Qin Zhang, Yaw Obeng, Kai Yan, Hailin Peng, Qiliang Li, Xiaoxiao Zhu, Hui Yuan, Angela R. Hight Walker, Zhongfan Liu, Lian-mao Peng, and Curt A. Richter. Toward clean and crackless transfer of graphene. *ACS Nano*, 5(11):9144–9153, 2011. PMID: 21999646.

[90] Xuesong Li, Yanwu Zhu, Weiwei Cai, Mark Borysiak, Boyang Han, David Chen, Richard D. Piner, Luigi Colombo, and Rodney S. Ruoff. Transfer of large-area graphene films for high-performance transparent conductive electrodes. *Nano Letters*, 9(12):4359–4363, 2009. PMID: 19845330.

[91] K. S. Novoselov, A. K. Geim, S. V. Morozov, D. Jiang, Y. Zhang, S. V. Dubonos, I. V. Grigorieva, and A. A. Firsov. Electric field effect in atomically thin carbon films. *Science*, 306(5696):666–669, 2004.

[92] Caterina Soldano, Ather Mahmood, and Erik Dujardin. Production, properties and potential of graphene. *Carbon*, 48(8):2127 – 2150, 2010.

[93] Liying Jiao, Ben Fan, Xiaojun Xian, Zhongyun Wu, Jin Zhang, and Zhongfan Liu. Creation of nanostructures with poly(methyl methacrylate)-mediated nanotransfer printing. *Journal of the American Chemical Society*, 130(38):12612–12613, 2008. PMID: 18763767.

[94] Alfonso Reina, Hyungbin Son, Liying Jiao, Ben Fan, Mildred S. Dresselhaus, ZhongFan Liu, and Jing Kong. Transferring and identification of single- and few-layer graphene on arbitrary substrates. *The Journal of Physical Chemistry C*, 112(46):17741–17744, 2008.

[95] C. R. Dean, A. F. Young, I. Meric, C. Lee, L. Wang, S. Sorgenfrei, K. Watanabe, T. Taniguchi, P. Kim, K. L. Shepard, and et al. Boron nitride substrates for high-quality graphene electronics. *Nature Nanotechnology*, 5(10):722726, Aug 2010.

[96] Xuesong Li, Weiwei Cai, Jinho An, Seyoung Kim, Junghyo Nah, Dongxing Yang, Richard Piner, Aruna Velamakanni, Inhwa Jung, Emanuel Tutuc, Sanjay K. Banerjee, Luigi Colombo, and Rodney S. Ruoff. Large-area synthesis of high-quality and uniform graphene films on copper foils. *Science*, 324(5932):1312–1314, 2009.

[97] Keun Soo Kim, Yue Zhao, Houk Jang, and et. al. Large-scale pattern growth of graphene films for stretchable transparent electrodes. *Nature*, 457:706–710, 2009.

[98] A. Pirkle, J. Chan, A. Venugopal, D. Hinojos, C. W. Magnuson, S. McDonnell, L. Colombo, E. M. Vogel, R. S. Ruoff, and R. M. Wallace. The effect of chemical residues on the physical and electrical properties of chemical vapor deposited graphene transferred to sio2. *Applied Physics Letters*, 99(12):122108, 2011.

[99] D. C. Elias, R. R. Nair, T. M. G. Mohiuddin, S. V. Morozov, P. Blake, M. P. Halsall, A. C. Ferrari, D. W. Boukhvalov, M. I. Katsnelson, A. K. Geim, and K. S.

Novoselov. Control of graphene's properties by reversible hydrogenation: Evidence for graphane. *Science*, 323(5914):610–613, 2009.

[100] M W Iqbal, Arun Kumar Singh, M Z Iqbal, and Jonghwa Eom. Raman fingerprint of doping due to metal adsorbates on graphene. *Journal of Physics: Condensed Matter*, 24(33):335301, jul 2012.

[101] Tim J. Booth, Peter Blake, Rahul R. Nair, Da Jiang, Ernie W. Hill, Ursel Bangert, Andrew Bleloch, Mhairi Gass, Kostya S. Novoselov, M. I. Katsnelson, and A. K. Geim. Macroscopic graphene membranes and their extraordinary stiffness. *Nano Letters*, 8(8):2442–2446, 2008. PMID: 18593201.

[102] Yung-Chang Lin, Chuanhong Jin, Jung-Chi Lee, Shou-Feng Jen, Kazu Suenaga, and Po-Wen Chiu. Clean transfer of graphene for isolation and suspension. *ACS Nano*, 5(3):2362–2368, 2011. PMID: 21351739.

[103] A. C. Ferrari, J. C. Meyer, V. Scardaci, C. Casiraghi, M. Lazzeri, F. Mauri, S. Piscanec, D. Jiang, K. S. Novoselov, S. Roth, and A. K. Geim. Raman spectrum of graphene and graphene layers. *Phys. Rev. Lett.*, 97:187401, Oct 2006.

[104] Axel Eckmann, Alexandre Felten, Artem Mishchenko, Liam Britnell, Ralph Krupke, Kostya S. Novoselov, and Cinzia Casiraghi. Probing the nature of defects in graphene by raman spectroscopy. *Nano Letters*, 12(8):3925–3930, 2012. PMID: 22764888.

[105] L. G. Canado, A. Jorio, E. H. Martins Ferreira, F. Stavale, C. A. Achete, R. B. Capaz, M. V. O. Moutinho, A. Lombardo, T. S. Kulmala, and A. C. Ferrari. Quantifying defects in graphene via raman spectroscopy at different excitation energies. *Nano Letters*, 11(8):3190–3196, 2011. PMID: 21696186.

[106] Martin Kalbac, Alfonso Reina-Cecco, Hootan Farhat, Jing Kong, Ladislav Kavan, and Mildred S. Dresselhaus. The influence of strong electron and hole doping on

the raman intensity of chemical vapor-deposition graphene. *ACS Nano*, 4(10):6055–6063, 2010. PMID: 20931995.

[107] Matteo Bruna, Anna K. Ott, Mari Ijs, Duhee Yoon, Ugo Sassi, and Andrea C. Ferrari. Doping dependence of the raman spectrum of defected graphene. *ACS Nano*, 8(7):7432–7441, 2014. PMID: 24960180.

[108] Zhen Hua Ni, Ting Yu, Yun Hao Lu, Ying Ying Wang, Yuan Ping Feng, and Ze Xiang Shen. Uniaxial strain on graphene: Raman spectroscopy study and band-gap opening. *ACS Nano*, 2(11):2301–2305, 2008. PMID: 19206396.

[109] T. M. G. Mohiuddin, A. Lombardo, R. R. Nair, A. Bonetti, G. Savini, R. Jalil, N. Bonini, D. M. Basko, C. Galiotis, N. Marzari, and et al. Uniaxial strain in graphene by raman spectroscopy:gpeak splitting, grneisen parameters, and sample orientation. *Physical Review B*, 79(20), May 2009.

[110] Ting Yu, Zhenhua Ni, Chaoling Du, Yumeng You, Yingying Wang, and Zexiang Shen. Raman mapping investigation of graphene on transparent flexible substrate: The strain effect. *The Journal of Physical Chemistry C*, 112(33):12602–12605, 2008.

[111] I. Forbeaux, J.-M. Themlin, and J.-M. Debever. High-temperature graphitization of the 6h-sic (0001) face. *Surface Science*, 442(1):9 – 18, 1999.

[112] J. Hass, R. Feng, T. Li, X. Li, Z. Zong, W. A. de Heer, P. N. First, E. H. Conrad, C. A. Jeffrey, and C. Berger. Highly ordered graphene for two dimensional electronics. *Applied Physics Letters*, 89(14):143106, 2006.

[113] Jia-An Yan, W. Y. Ruan, and M. Y. Chou. Phonon dispersions and vibrational properties of monolayer, bilayer, and trilayer graphene: Density-functional perturbation theory. *Phys. Rev. B*, 77:125401, Mar 2008.

[114] L. Lindsay, D. A. Broido, and Natalio Mingo. Flexural phonons and thermal transport in multilayer graphene and graphite. *Phys. Rev. B*, 83:235428, Jun 2011.

[115] Hui Wang, Yufang Wang, Xuewei Cao, Min Feng, and Guoxiang Lan. Vibrational properties of graphene and graphene layers. *Journal of Raman Spectroscopy*, 40(12):1791–1796, 2009.

[116] L. Lindsay and D. A. Broido. Optimized tersoff and brenner empirical potential parameters for lattice dynamics and phonon thermal transport in carbon nanotubes and graphene. *Phys. Rev. B*, 81:205441, May 2010.

[117] AC Ferrari. Interpretation of raman spectra of disordered and amorphous carbon. *Phys. Rev. B*, 61, 05 2000.

[118] J.-C. Charlier, P. C. Eklund, J. Zhu, and A. C. Ferrari. *Electron and Phonon Properties of Graphene: Their Relationship with Carbon Nanotubes*, pages 673–709. Springer Berlin Heidelberg, Berlin, Heidelberg, 2008.

[119] Denis L Nika and Alexander A Balandin. Two-dimensional phonon transport in graphene. *Journal of Physics: Condensed Matter*, 24(23):233203, may 2012.

[120] Deyu Li, Yiying Wu, Philip Kim, Li Shi, Peidong Yang, and Arun Majumdar. Thermal conductivity of individual silicon nanowires. *Applied Physics Letters*, 83(14):2934–2936, 2003.

[121] Alexander Balandin and Kang L. Wang. Effect of phonon confinement on the thermoelectric figure of merit of quantum wells. *Journal of Applied Physics*, 84(11):6149–6153, 1998.

[122] Alexander A. Balandin. Thermal properties of graphene and nanostructured carbon materials. *Nature Materials*, 10(8):569581, Jul 2011.

[123] P. Klemens. Theory of the a-plane thermal conductivity of graphite. *Journal of Wide Bandgap Materials*, 7:332–339, 04 2000.

[124] Stphane Berciaud, Sunmin Ryu, Louis E. Brus, and Tony F. Heinz. Probing the intrinsic properties of exfoliated graphene: Raman spectroscopy of free-standing monolayers. *Nano Letters*, 9(1):346–352, 2009. PMID: 19099462.

[125] D. Graf, F. Molitor, K. Ensslin, C. Stampfer, A. Jungen, C. Hierold, and L. Wirtz. Spatially resolved raman spectroscopy of single- and few-layer graphene. *Nano Letters*, 7(2):238–242, 2007. PMID: 17297984.

[126] J. Maultzsch, S. Reich, and C. Thomsen. Double-resonant raman scattering in graphite: Interference effects, selection rules, and phonon dispersion. *Phys. Rev. B*, 70:155403, Oct 2004.

[127] F. Tuinstra and J. L. Koenig. Raman spectrum of graphite. *The Journal of Chemical Physics*, 53(3):1126–1130, 1970.

[128] Christian Thomsen and Stephanie Reich. Double resonant raman scattering in graphite. *Physical review letters*, 85:5214–7, 01 2001.

[129] A. Baranov, Bekhterev Alexander, Ya Bobovich, and V. Petrov. Interpretation of certain characteristics in raman spectra of graphite and glassy carbon. *Optics and Spectroscopy*, 62:612–616, 04 1987.

[130] Istvan Pcsik, Martin Hundhausen, Margit Kos, and Lothar Ley. Origin of the d peak in the raman spectrum of microcrystalline graphite. *Journal of Non-Crystalline Solids*, 227-230:1083 – 1086, 1998.

[131] AC Ferrari, J. Meyer, Vittorio Scardaci, C Casiraghi, Michele Lazzeri, Francesco Mauri, S Piscanec, Dingde Jiang, K Novoselov, Siegmar Roth, and AK Geim. Ra-

man spectrum of graphene and graphene layers. *Physical review letters*, 97:187401, 12 2006.

[132] D. Basko, S. Piscanec, and A. Ferrari. Electron-electron interactions and doping dependence of the two-phonon raman intensity in graphene. *Physical Review B*, 80, 06 2009.

[133] Edward McCann and Vladimir I. Fal'ko. Landau-level degeneracy and quantum hall effect in a graphite bilayer. *Phys. Rev. Lett.*, 96:086805, Mar 2006.

[134] Andrea C. Ferrari. Raman spectroscopy of graphene and graphite: Disorder, electronphonon coupling, doping and nonadiabatic effects. *Solid State Communications*, 143(1):47 – 57, 2007.

[135] M. J. Matthews, M. A. Pimenta, G. Dresselhaus, M. S. Dresselhaus, and M. Endo. Origin of dispersive effects of the raman d band in carbon materials. *Phys. Rev. B*, 59:R6585–R6588, Mar 1999.

[136] Diane S. Knight and William B. White. Characterization of diamond films by raman spectroscopy. *Journal of Materials Research*, 4(2):385393, 1989.

[137] D. M. Basko. Boundary problems for dirac electrons and edge-assisted raman scattering in graphene. *Phys. Rev. B*, 79:205428, May 2009.

[138] C. Casiraghi, A. Hartschuh, H. Qian, S. Piscanec, C. Georgi, A. Fasoli, K. S. Novoselov, D. M. Basko, and A. C. Ferrari. Raman spectroscopy of graphene edges. *Nano Letters*, 9(4):1433–1441, 2009. PMID: 19290608.

[139] M.M. Lucchese, F. Stavale, E.H. Martins Ferreira, C. Vilani, M.V.O. Moutinho, Rodrigo B. Capaz, C.A. Achete, and A. Jorio. Quantifying ion-induced defects and raman relaxation length in graphene. *Carbon*, 48(5):1592 – 1597, 2010.

[140] Ryan Beams, Luiz Gustavo Canado, and Lukas Novotny. Low temperature raman study of the electron coherence length near graphene edges. *Nano Letters*, 11(3):1177–1181, 2011. PMID: 21341735.

[141] S. Pisana, Michele Lazzeri, Cinzia Casiraghi, Kostya Novoselov, Andre Geim, Andrea Ferrari, and Francesco Mauri. Breakdown of the adiabatic born-oppenheimer approximation in graphene. *Nature materials*, 6:198–201, 04 2007.

[142] D. M. Basko. Theory of resonant multiphonon raman scattering in graphene. *Phys. Rev. B*, 78:125418, Sep 2008.

[143] Martin C. Nuss, K. W. Goossen, J. P. Gordon, P. M. Mankiewich, M. L. OMalley, and M. Bhushan. Terahertz timedomain measurement of the conductivity and superconducting band gap in niobium. *Journal of Applied Physics*, 70(4):2238–2241, 1991.

[144] K. M. Dani, J. Lee, R. Sharma, A. D. Mohite, C. M. Galande, P. M. Ajayan, A. M. Dattelbaum, H. Htoon, A. J. Taylor, and R. P. Prasankumar. Intraband conductivity response in graphene observed using ultrafast infrared-pump visible-probe spectroscopy. *Phys. Rev. B*, 86:125403, Sep 2012.

[145] Momchil T Mihnev, Faris Kadi, Charles J Divin, Torben Winzer, Seunghyun Lee, Che-Hung Liu, Zhaohui Zhong, Claire Berger, Walt A De Heer, Ermin Malic, et al. Microscopic origins of the terahertz carrier relaxation and cooling dynamics in graphene. *Nature communications*, 7:11617, 2016.

[146] P. J. Hale, S. M. Hornett, J. Moger, D. W. Horsell, and E. Hendry. Hot phonon decay in supported and suspended exfoliated graphene. *Phys. Rev. B*, 83:121404, Mar 2011.